A PolyMUMPs Capacitive Micromachined Ultrasonic Transducer

by

Ming Cai

A THESIS SUBMITTED IN PARTIAL FULFILLMENT OF
THE REQUIREMENTS FOR THE DEGREE OF

MASTER OF APPLIED SCIENCE

in

The Faculty of Graduate Studies

(Electrical and Computer Engineering)

THE UNIVERSITY OF BRITISH COLUMBIA

(Vancouver)

April 2011

Abstract

This work presents the design of Capacitive Micromachined Ultrasonic Transducers (CMUTs) with one and multiple bottom electrodes and their fabrication using the PolyMUMPs technique provided by MEMSCAP Inc. It also reports a new behavioral model of the CMUTs written in VHDL-AMS, complemented by a comparison between finite element analysis, behavioral simulations and experimental measurements on the newly fabricated CMUT arrays. As an improvement on a previously developed VHDL-AMS CMUT behavioral model [1], where the CMUT was treated as a movable rigid plate capacitor, a mode decomposition approach was used in the present work to better approximate the dynamics of the CMUT membrane. Besides the frequency responses, time responses and electro-mechanical conversion efficiency, the simulation results also showed the electrostatic spring softening effect, and the optimization of the DC/AC voltage ratio that leads to a maximum transmitted acoustic power. The CMUT membrane capacitance variation predicted by the model compares favorably with results from the finite element analysis, with better matching than the previously developed models. Polytec Micro System Analyzer (Polytec MSA-500) using Laser Doppler Vibrometry was used for the experimental characterization, in which the pull-in voltage, vibration modes and their respective resonant frequencies were determined. Characterization results were compared with the ones from the finite element analysis and the behavioral model simulations, and excellent agreement was shown.

Preface

The results of the experimental characterization in Chapter 5 have been published in IEEE Sensors, 2011 (Wei You, Edmond Cretu, Robert Rohling, and Ming Cai-"Tiltable Ultrasonic Transducers: concept, beamforming methods and simulation").

Figure 2 was drawn by Hadi Najar, and Figure 47 was from a training presentation given by Polytec Inc.

Check relative chapters and pages to see reference and footnotes with similar information.

Table of Contents

List of Tables

List of Figures

Acknowledgements

I would like to offer my sincere gratitude to the help and guidance of my supervisor Dr. Edmond Cretu. His academic advice and words of wisdom have inspired me, encouraged me, and accompanied me all through the two years of my program. I would also like to acknowledge and thank for the advice from Dr. Robert Rohling and Dr. Shahriar Mirabbasi in our group meetings from which I have benefited a lot.

I thank my labmate Wei You for all the discussions we had that helped me solve many problems and clear my thoughts.

Last but not least, I owe my special thanks to my parents who have always been there for me through good times and bad times. I would not have what I have today if it was not for your support.

Dedication

To My Parents

Chapter 1

Introduction

1.1 Principle of Operation and Advantages of CMUTs

An ultrasonic transducer is a device that converts energy between electrical and ultrasound domains, and it has a variety of applications in sonar, medical ultrasonography, non-destructive testing, etc. The typical traditional ultrasonic transducers mainly refer to piezoelectric devices that operate on the fact that piezoelectric crystals and ceramics have the property of changing size (induced strain) when a voltage is applied. Thus they can be caused to vibrate at high frequencies and produce high frequency sound waves when a time-varying current with a high frequency is applied across them.

Traditional piezoelectric transducers have been dominant in ultrasound imaging for decades in spite of their drawbacks, such as impedance mismatch, frequency range limitations, etc [2], [3]. The impedance mismatch is more severe in the case of air-coupled ultrasound than in water-coupled ultrasound because the acoustic impedance of air (400 kg/m^2s) is much smaller than that of the piezoelectric materials that are commonly used in ultrasound imaging (30×10^6 kg/m^2s) [2], leading to an inefficient operation. The frequency range limitations are mainly due to the fact that the frequency range of operation of a piezoelectric transducer is determined by its geometry. Traditional piezoelectric transducers also show bad noise performance and surface displacement limits because of the intrinsic properties of the piezoelectric materials [2]. On top of those

disadvantages, traditional piezoelectric transducers are temperature sensitive and can only be used near room temperature [3].

With the advances in the research in ultrasonics and micro-electro-mechanical systems since the early 1990s, CMUTs emerged as a new ultrasonic transducer technology with many advantages over traditional piezoelectric transducers in terms of wider bandwidth, higher sensitivity and temperature insensitivity [1]-[3], with good prospects in high resolution ultrasound imaging in cancer diagnosis. Moreover, CMUTs are fabricated with the same technology used in integrated circuit fabrication, and this implies the possibility of integrating CMUTs and the control and signal processing circuits together on one die, which significantly lowers the complexity of electrical interconnections. Additionally, microfabrication technology makes it also easier to fabricate large 2D CMUT arrays and arrays with different geometries.

In general, a Capacitive Micromachined Ultrasonic Transducer (CMUT) is a membrane suspended over a substrate with an electrode on which a DC bias and a time-varying voltage can be applied, as shown in Figure 1.

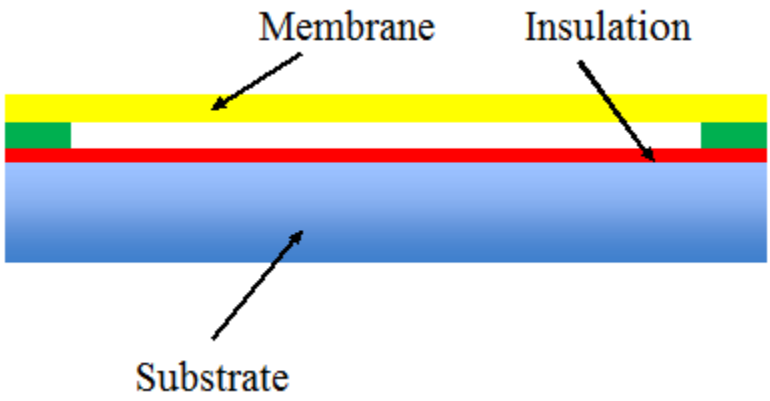

Figure 1. Cross section of a simple CMUT.

With the electrostatic force that is generated by the applied voltages, the CMUT membrane can be perturbed from its resting position and made to deflect and/or to vibrate. By defining the parameters and geometry of the CMUT, the resonant frequency of the CMUT membrane can be set in the ultrasonic frequency range; it will therefore be able to emit a series of ultrasound pressure waves into the surrounding medium when it vibrates at its resonance. Reciprocally, the pressure waves from the medium incident on the CMUT membrane can cause it to vibrate, which generates a time-varying current if the DC bias is fixed and proper back-end circuits are present.

1.2 Previous Works in CMUT Modeling

A large amount of research work has been carried out in the behavioral modeling of CMUTs, to better understand the performance of CMUT devices and to assist in the experimental characterization of the devices. Early works mostly focused on transducers with grooved or sandblasted backplates [4]-[8], in which the transducers were considered as a combination of individual resonators. They were mainly based on Mason's derivations [9] with corrections and modifications, and adopted a transformer equivalent circuit that links the electrical domain with the acoustic domain. However, the transducers in [5] operated at relatively low frequencies and the model prediction showed discrepancies from experimental measurements. More rigorous models of the CMUT were proposed, taking into account different types of losses and parasitic effects: [3] considered various parasitic losses due to packaging, mechanical coupling, and resistive losses (capacitance, inductance, resistance, etc.); [10] took the energy loss and the noise into consideration in the receiver model; [7] considered several mechanical stiffness effects, and [7] and [11] both delved into the effect of the gas kept in the cavity between the plate and the substrate. A PSpice model of the CMUT was presented in [12] based on the analytical distributed model reported in [11], but there was no published work describing the VHDL-AMS

implementation of a behavioral model until [1]. In [1], the CMUT cell was treated as a movable rigid plate capacitor with one degree-of-freedom whose dynamics was given by a mass-spring-damper lumped model, and the displacement of the CMUT membrane was considered to be uniform all over the membrane surface, which deviated from the actual dynamics of the CMUT membrane.

1.3 Preview of This Work

A first CMUT fabrication cycle using the PolyMUMPs technology provided by MEMSCAP Inc. was carried out in late 2009, using a layout design of CMUTs done by a colleague from MiNa (Microsystems and Nanotechnology) Research Group. The cross-sectional and the top view of the structure of a CMUT cell in the design is presented in Figure 2[1].

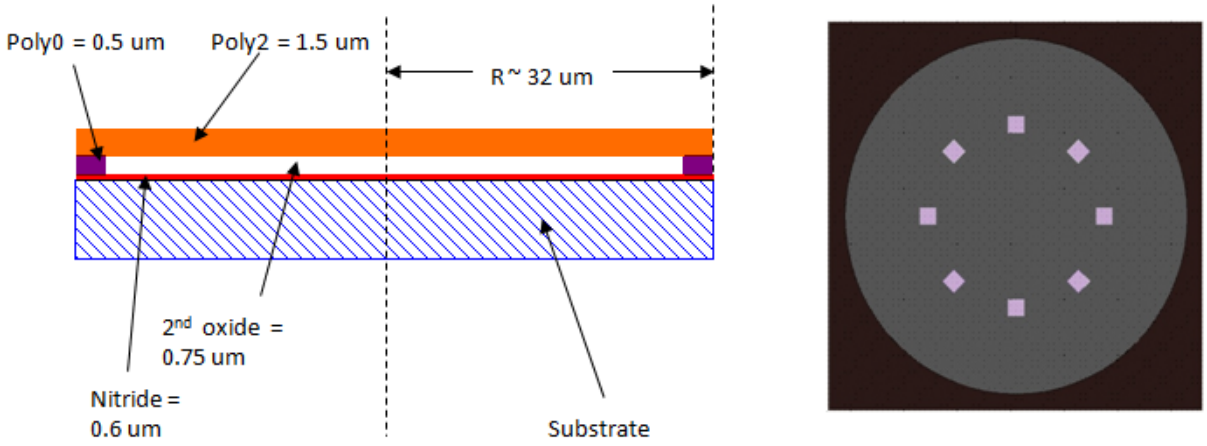

Figure 2. The cross-sectional (left) and the top view (right) of a CMUT cell in the previous design.

The 8 squares in the top view of a CMUT cell are the release holes on the Poly2 layer, which are necessary to etch away the second silicon dioxide layer under Poly2 to form the gap during the

[1] Courtesy: Hadi Najar.

hydrofluoric etch process. In this design, the CMUT cell was of a circular shape with a radius of 32μm. The second polysilicon layer Poly2 was chosen as the structural layer, and the substrate acted as the bottom electrode, insulated by the silicon nitride layer from the structural layer. The simulation results from an FEM model, simulated using COMSOL Multiphysics (COMSOL Inc., Los Angeles, CA, USA), predicted a first resonant frequency around 6MHz and a pull-in voltage over 270V. However, the experimental characterization has shown failures in all fabricated structures - the gap between the CMUT membrane and the insulating layer was non-existent. Possible causes were the missing of the second oxide layer, and several violations of the design rules.

In this work, a new design of CMUTs was carried out still using the same PolyMUMPs technology, but ensuring a more conservative approach with respect to the design rules. COMSOL Multiphysics simulations have been used to design and optimize the structural parameters. Considering the limitations in the testing equipments and the capacity of the control circuits, the structural parameters were determined on the premise that the desired pull-in voltage and the first resonant frequency of the CMUT cells were 91V and over 1MHz respectively.

A more rigorous behavioral model of the CMUT was proposed. In developing this new model, we resorted to the theories of plate and membrane vibrations and adopted a mode decomposition approach involving modal participation factors to better approximate the motion of the CMUT membrane. To the best of the author's knowledge, this was the first time that modal participation factors were introduced in the behavioral modeling of CMUTs. Results of comparisons between the average CMUT membrane capacitance simulated using this new VHDL-AMS model and simulated using the finite element model developed in COMSOL Multiphysics showed excellent agreement, with an error of 2.5%, whereas the comparisons between the same finite element

simulations (taken as reference) and the previously developed VHDL-AMS model [1] led to an error of 24%.

Since this new behavioral model involved a large amount of non-linearities, difficult to implement in SPICE simulators, it was also written in VHDL-AMS language and verified using SMASH (DOLPHIN Integration, Meylan, France) HDL simulator, that allows user-defined VHDL-AMS models to integrate with other electronic components. All the parameters of the model were imported from the CMUT cells that were fabricated using the PolyMUMPs technology. Finite element analyses by COMSOL Multiphysics were performed as comparison with the simulation results of the model, and the two showed good matching: excellent agreement in the resonant frequency and a 12% error in the pull-in voltage (whereas there was a 16% error in the pull-in voltage using the previously developed VHDL-AMS model [1]). The electro-mechanical conversion efficiency was obtained, and the electrostatic spring softening effect, which was not observed in the previous model [1], was observed in the new model simulation. The new model deals with the DC and AC voltage respectively, providing the opportunity for the optimization of the DC/AC voltage ratio in achieving a maximum converted acoustic power. The present work is the first to report on such power transfer optimization.

Polytec Micro System Analyzer (Polytec MSA-500) based on Laser Doppler Vibrometry was used in the experimental characterization of the CMUT cells. The measurement results showed excellent matching with the FEA and model simulation results in both the pull-in voltage and resonant frequencies. The first three vibration modes were observed under both symmetric and asymmetric actuations, and the mode shapes displayed a good correspondence with theoretical prediction. This was the first time that the second vibration mode was excited purposely under asymmetric actuation.

The second chapter includes the new design of CMUTs, the optimization of geometry parameters using COMSOL Multiphysics simulations, and the design of layout masks. The third chapter focuses on analytical modeling of CMUTs based on theories of plate and membrane vibrations. The model simulation results are presented in the fourth chapter, as well as the necessary settings of the simulation software, followed by the equipment software settings and the experimental characterization. The last chapter ends with a set of conclusions and an outline of future work.

Chapter 2

Design of CMUTs

2.1 Fabrication Technology and Structure of CMUTs

2.1.1 Fabrication Technology and Processes

Considering the performance and specific structure of a CMUT, the CMUT cells in this work were fabricated using the PolyMUMPs process, a three-layer polysilicon micromachining process offered by MEMSCAP Inc. (Raleigh, NC, USA). It is one of the three standard processes offered as part of their Multi-User MEMS Process (MUMPs) program, the other two being MetalMUMPs (an electroplated nickel process) and SOIMUMPs (a silicon-on-insulator micromachining process). A cross-sectional view showing all the 7 layers of the PolyMUMPs process is given in Figure 3 [13].

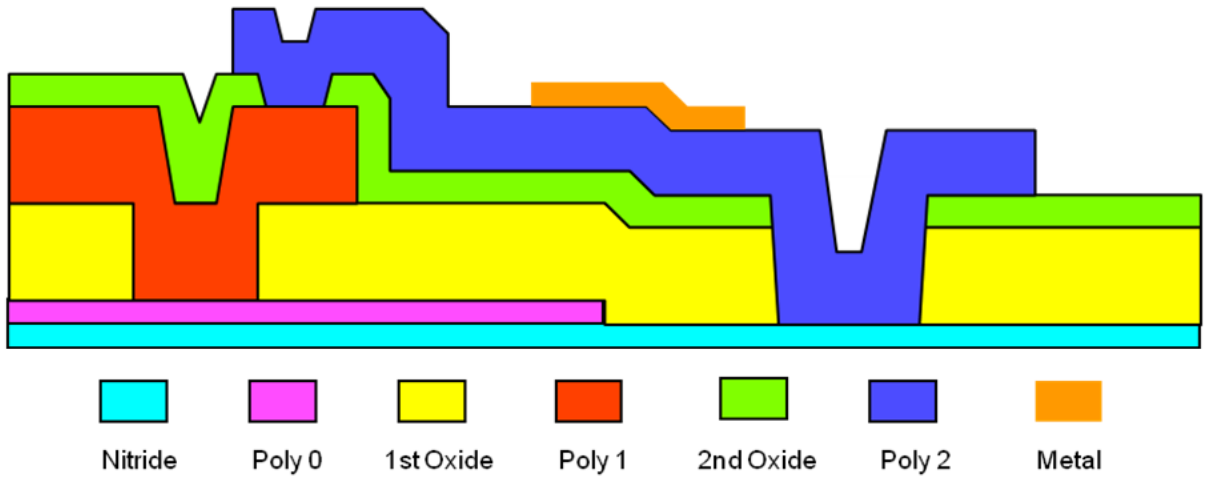

Figure 3. Cross-sectional view of the 7 layers of the PolyMUMPs process.

The 600nm silicon nitride layer is deposited on the wafers using LPCVD (Low Pressure Chemical Vapor Deposition). It acts as the insulation between the substrate and electrical surface layers. It is followed directly by the LPCVD deposition of a 500nm polysilicon layer Poly0, which is the electrical layer for ground plane or electrode formation and is below the first mechanical layer. After the etching of Poly0, a 2.0μm LPCVD PSG (phosphosilicate glass) sacrificial layer is formed. It is the first sacrificial oxide layer, providing the gap between the substrate or silicon nitride and Poly1. The first polysilicon structural layer Poly1 is deposited by LPCVD as well at a thickness of 2.0μm, and the second sacrificial oxide layer is formed on the top of it, with a thickness of 0.75μm, providing the gap between Poly1 and Poly2. The second structural layer Poly2 (1.5μm thick) is deposited after the etching of the second oxide layer, followed by a 0.5μm metal layer (gold with a thin adhesion layer) that provides for probing, bonding, electrical routing and highly reflective mirror surfaces. After the deposition and patterning of all the 7 layers comes the hydrofluoric acid release which etches away the two oxide layers and forms the gaps. Table 1 outlines the names of the material layers, their thicknesses and the lithography level names associated with those layers [13].

Table 1. The material layer names, thicknesses and the related lithography level names.

Material Layer Name	Thickness (μm)	Lithography Level Name
Silicon Nitride	0.6	--
Poly0	0.5	POLY0 (HOLE0)
First Oxide	2.0	DIMPLE ANCHOR1
Poly1	2.0	POLY1 (HOLE1)

Material Layer Name	Thickness (μm)	Lithography Level Name
Second Oxide	0.75	POLY1_POLY2_VIA ANCHOR2
Poly2	1.5	POLY2 (HOLE2)
Metal	0.5	METAL (HOLEM)

Some of the terms in Table 1 and their meanings are: ANCHOR1 - opens points-of-contact between Poly1 and the substrate, silicon nitride or Poly0, DIMPLE - generates "bumps" in under-surface of Poly1to minimize stiction, POLY1_POLY2_VIA - opens points-of-contact between the first and second polysilicon layers, ANCHOR2 - opens points-of-contact between Poly2 and the substrate or silicon nitride and HOLE - provides holes for respective layers [13].

2.1.2 Design of CMUT Structures

In the present design of the CMUT array die, we wanted the first resonant frequency to be at least over 1MHz, in order to have good axial resolution, and the pull-in voltage to be as low as possible, in order to make the interface with the CMOS electronics easier (ideally under 100V due to limitations of testing equipments). Based on the above principles, the new design presented in this work chose the circular shape as the shape of a CMUT cell, the 0.5μm Poly0 layer as the bottom electrode, the 0.75μm second oxide layer as the gap in order to keep the pull-in voltage low, and the 1.5μm Poly2 as the structural layer. The cross section of a single CMUT cell is given in Figure 4.

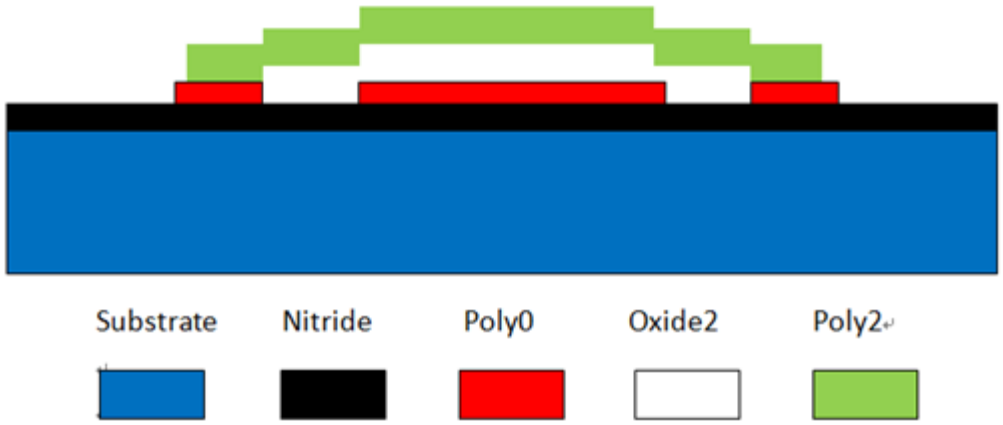

Figure 4. Cross section of a CMUT cell in the new design.

However, potential problems existed in this structure of a CMUT cell. The most important one is that the Poly0 circular bottom electrode will be exposed and subsequently removed during the Poly1 etch due to the absence of the Poly1 layer (the first silicon dioxide layer Oxide1 is not used in this design, so Poly1 will be deposited directly on Poly0 thus Poly0 layer will be etched away). To avoid this, we substituted the Poly1 layer for Poly0 as the bottom electrode. The cross section of an improved CMUT cell is shown in Figure 5.

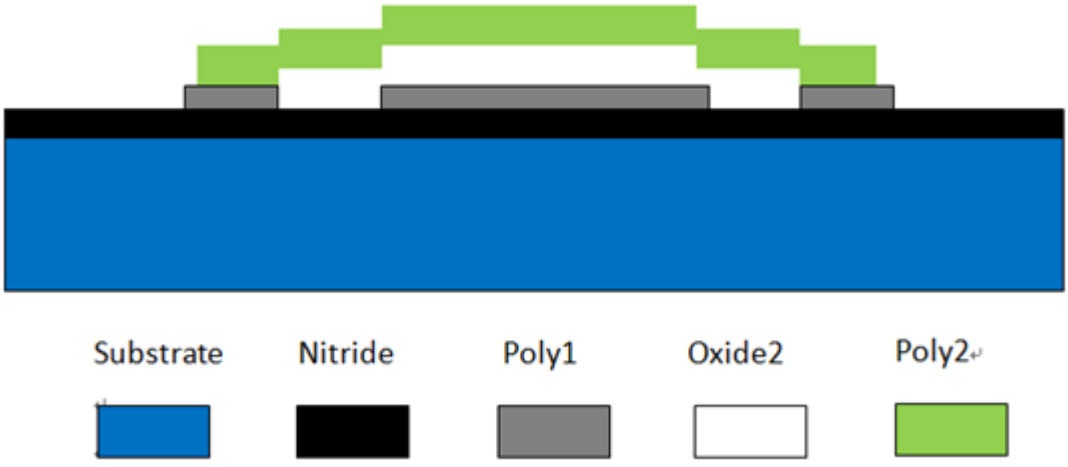

Figure 5. Cross section of an improved CMUT cell in the new design.

2.2 Finite Element Analyses (FEA) Using COMSOL Multiphysics

2.2.1 Geometry of CMUT in COMSOL Multiphysics

Since the fabrication technology was chosen, the material as well as thickness of each layer were predetermined; the only parameter left to be explored was the radius of a CMUT cell. We carried out a series of finite element analyses using COMSOL Multiphysics (COMSOL, Inc., Los Angeles, CA, USA) to determine the radius of the CMUT cell in order to meet our previous specifications of the resonant frequencies and pull-in voltage.

The geometry of the FEM model used in COMSOL Multiphysics is shown in Figure 6.

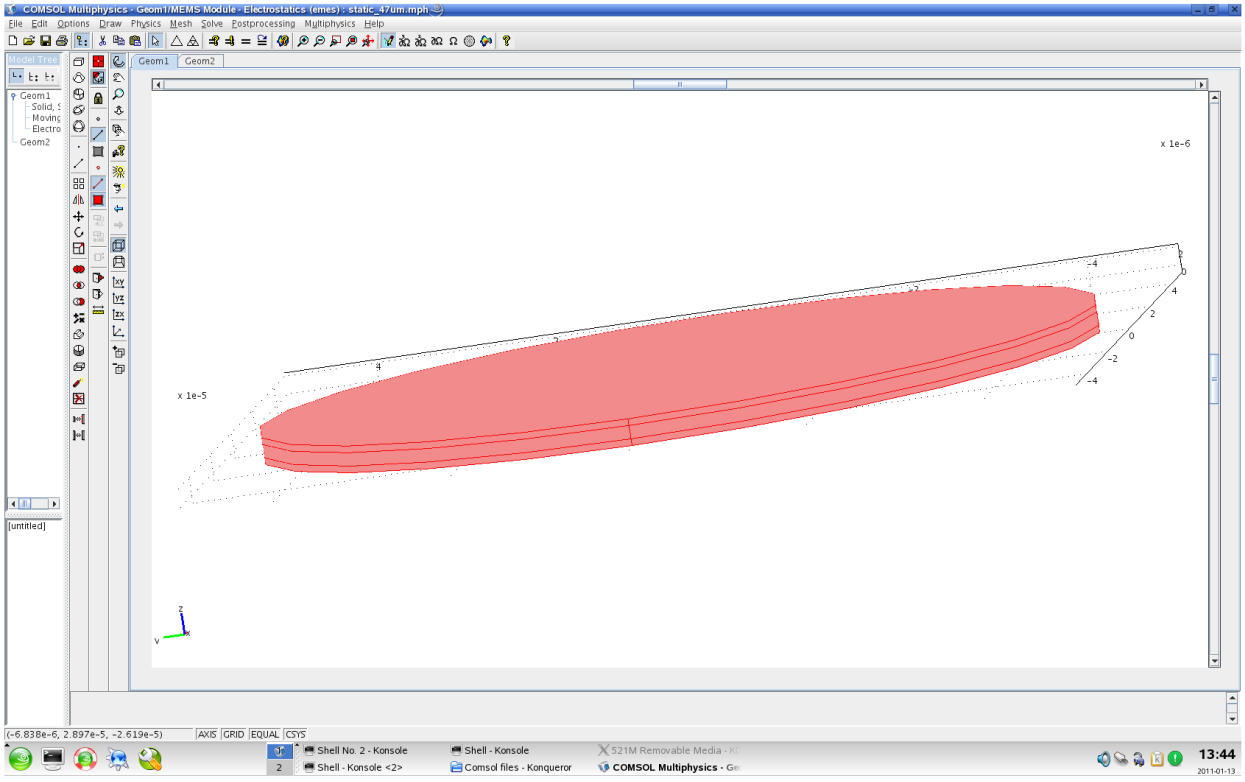

Figure 6. Geometry of the FEM model used in COMSOL Multiphysics.

2.2.2 Results of FEA and Determination of Parameters

In the ‘Free Mesh Parameters’ window, we chose ‘Extra coarse’ for the ‘Predefined mesh sizes’ to reduce the amount of calculations considering the capacity of the computer.

First, we wanted to run a parametric analysis by applying a series of DC biases on the CMUT membrane to determine the pull-in voltage. The settings in the ‘Solver Parameters’ window are given in Figure 7.

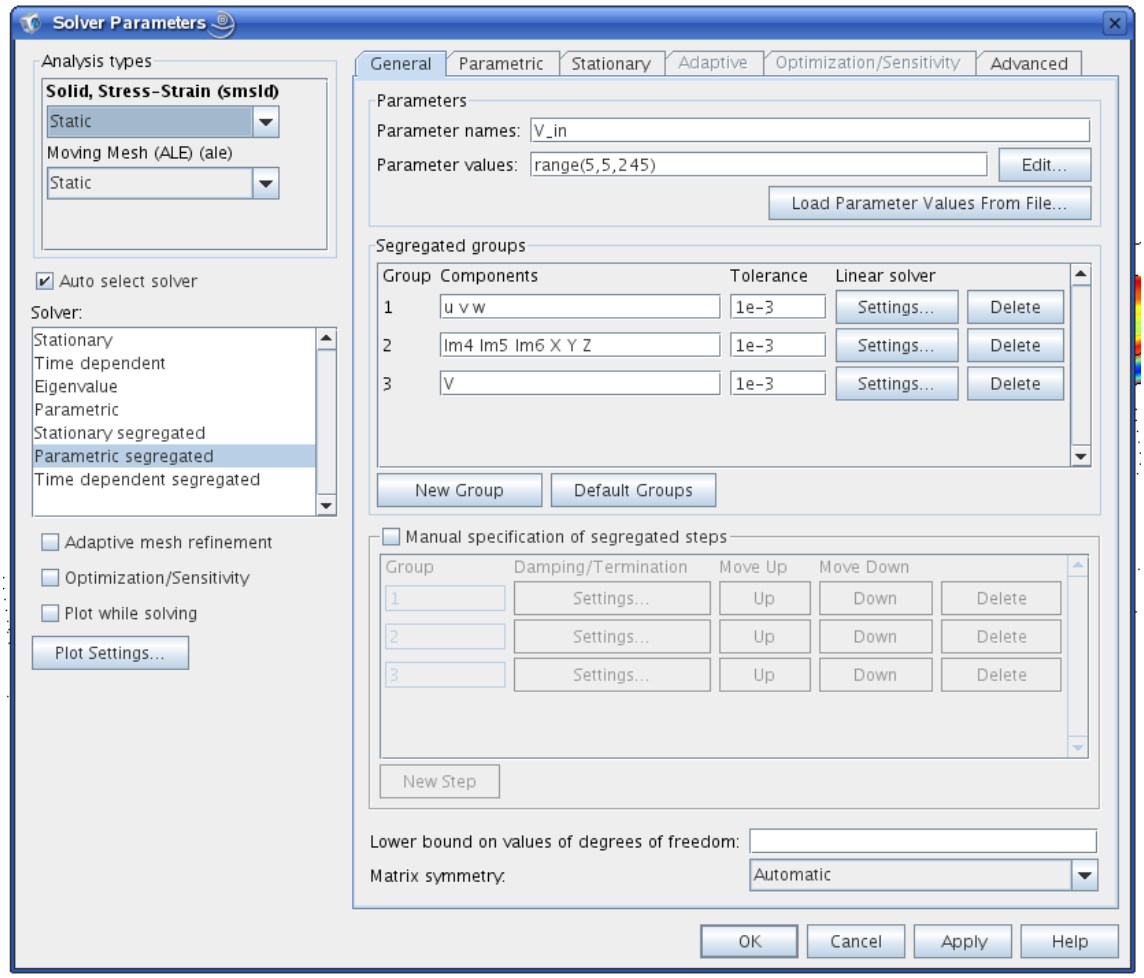

Figure 7. The settings in the ‘Solver Parameters’ window for parametric analysis.

The ‘Parameter names’ blank was given by V_in, which is the applied voltage on the bottom surface of the CMUT membrane. The range of the ‘Parameter values’ was set to (5, 5, 245) which means the starting voltage is 5V, the ending voltage is 245V and the step is 5V. The center displacement of the CMUT membrane with a radius of 32μm is shown in Figure 8.

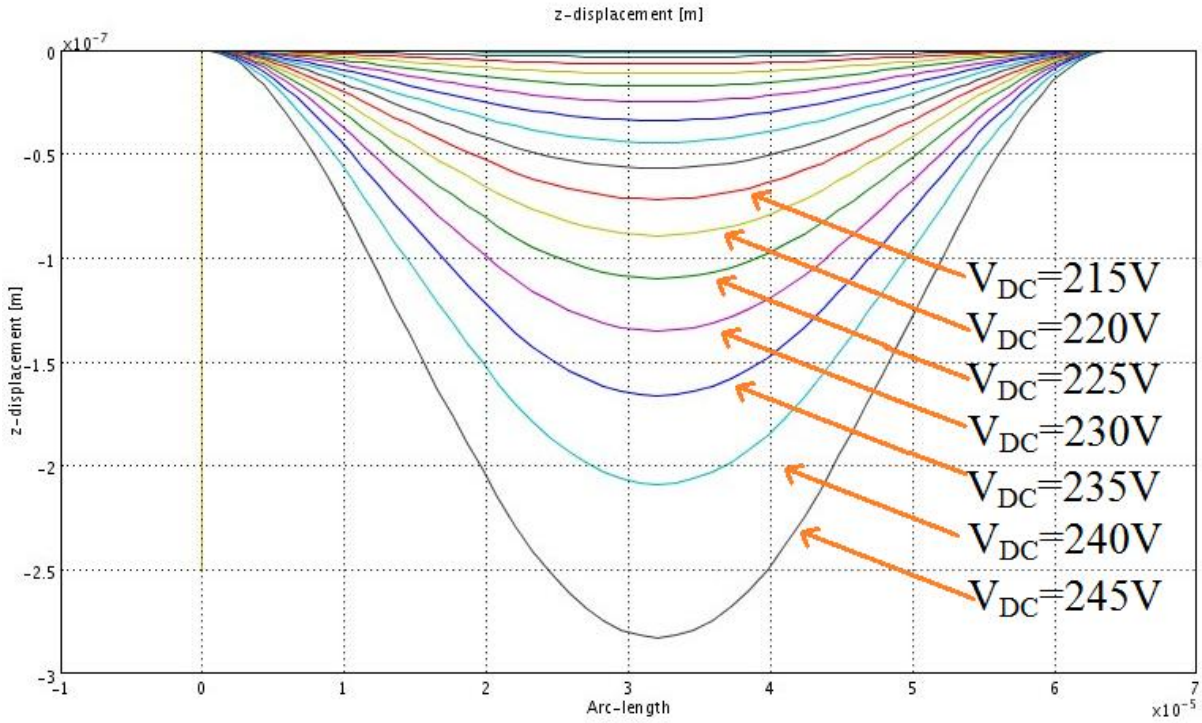

Figure 8. The displacement of the CMUT membrane with a radius of 32μm under the DC biases from 5V to 245V with a step of 5V in COMSOL simulation.

In Figure 8, the unit for the x-axis is *m*, the direction of z-displacement is perpendicular to the CMUT membrane and towards the substrate. As the DC bias increases, the displacement of the CMUT membrane increases. From Figure 8, we can see that even when the applied DC bias is as high as 245V, the center displacement is still about 0.284μm and the membrane has not collapsed yet. Therefore, similar analyses were carried out with different voltage ranges and the

pull-in voltage was determined to be at 248V, where a convergence in the solving process was not reached.

As a pull-in voltage of 248V might bring some challenges to the design and microfabrication of the back-end control circuit of CMUTs, we performed the similar parametric analyses on different radii (35μm, 40μm, 45μm, 50μm), for the pull-in voltage will decrease as the radius increases. The pull-in voltages of the CMUT membranes with different radii are given in Table 2.

Table 2. The pull-in voltages of the CMUT membranes with different radii, obtained from parametric analyses using COMSOL Multiphysics.

Radius (μm)	32	35	40	45	50
Pull-in voltage (V)	248	207	159	126	102

Since when the radius of the membrane is 50μm, the pull-in voltage of 102V is already low enough for the control circuits, and we want as many CMUT cells on one die as possible, larger radii over 50μm were not simulated. In order to see the resonant frequencies and different mode shapes of the CMUT membrane, an eigenfrequency analysis was performed. The settings in the 'Solver Parameters' window are shown in Figure 9.

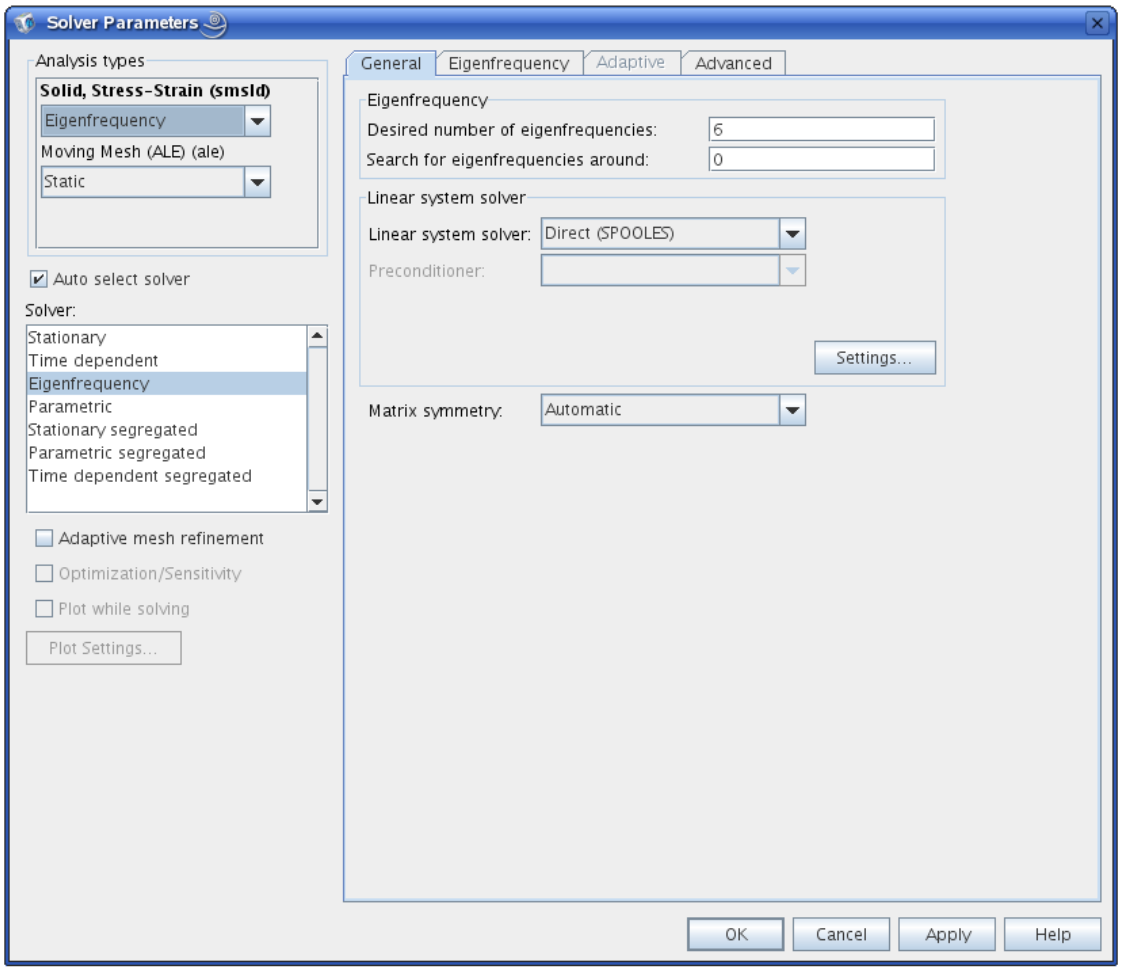

Figure 9. The settings in the 'Solver Parameters' window for eigenfrequency analysis.

The 'Desired number of eigenfrequencies' was set to 6, which means 6 eigenfrequencies and vibration mode shapes could be observed in the result. The first 6 mode shapes of the CMUT membrane are given in Figure 10, and the first 6 eigenfrequencies of the CMUT membrane with a radius of 32μm are given in Table 3.

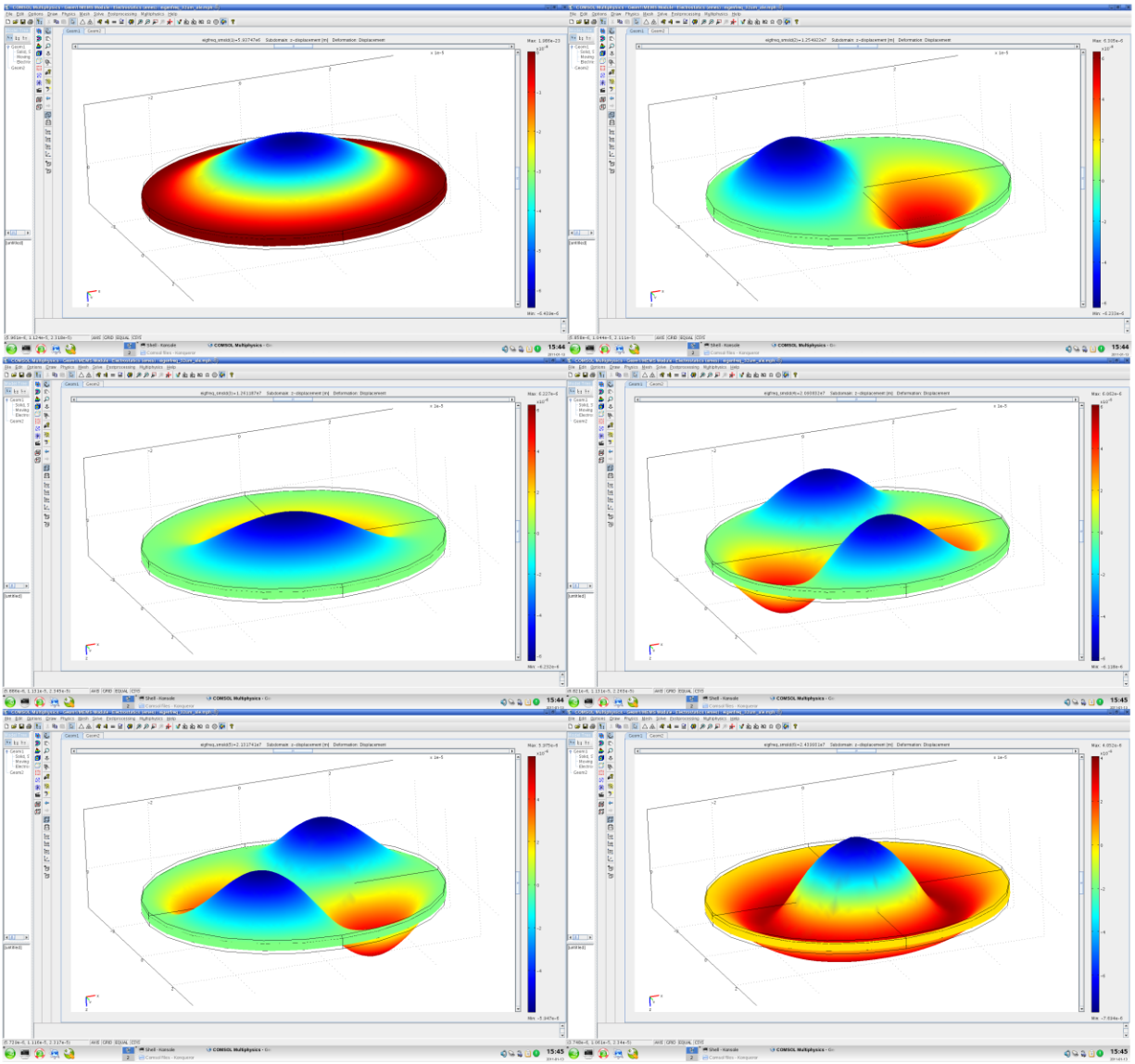

Figure 10. The first 6 mode shapes: top left (the 1st), top right and middle left (the 2nd), middle right and bottom left (the 3rd), bottom right (the 4th).

Table 3. The first 6 eigenfrequencies of the CMUT membrane with a radius of 32μm.

Number of Mode	1	2	3	4	5	6
Eigenfrequency (MHz)	5.937	12.549	12.612	20.938	21.317	24.399

In Figure 10, the top left mode shape shows the 1st vibration mode where there are no concentric circles or diameter lines as symmetry elements (concentric circles and diametral lines are rings and lines of points on a CMUT membrane whose total displacement is zero, same as the boundary of the membrane); the top right (as well as the middle left) and the middle right (as well as the bottom left) mode shapes are the 2nd and 3rd vibration modes there are no concentric circles but one and two diameter lines respectively (one and two lines of points with zero displacement separating the two and four "bumps" respectively); the bottom right mode shape is the 4th mode shape where there is one concentric circle and no diametral lines (one ring of points with zero displacement near the edge of the membrane). Figure 10 shows that the FEA corresponds very well with the vibrating plate theories mentioned in the next chapter.

A frequency response analysis was also run to see the resonant frequencies of the CMUT membrane. The settings in the 'Solver Parameters' window for such analysis are shown in Figure 11.

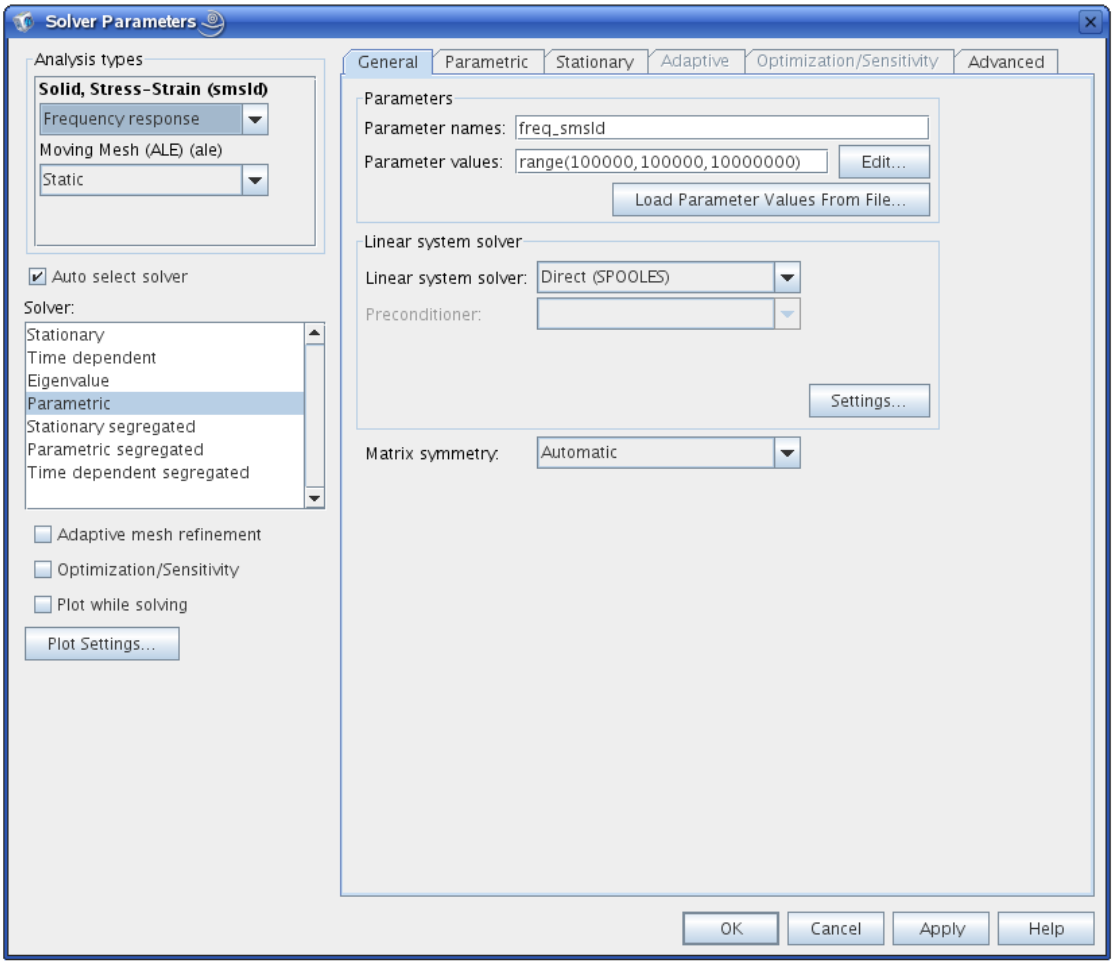

Figure 11. The settings in the 'Solver Parameters' window for frequency response analysis.

The frequency range was set to from 100kHz to 10MHz, with a step of 100KHz. And the simulated frequency response for the CMUT membrane with a radius of 32μm is given in Figure 12.

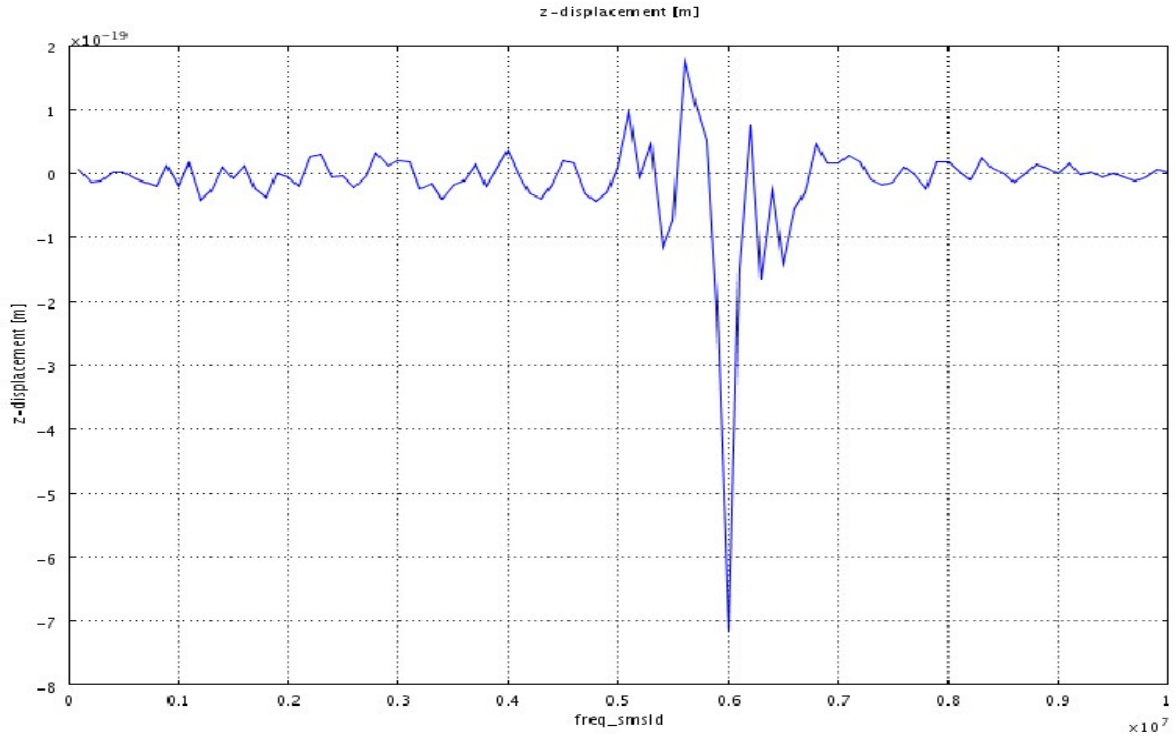

Figure 12. The frequency response for the CMUT membrane with a radius of 32μm.

The unit for the x-axis in Figure 12 is Hz, the z-displacement also means the displacement of the CMUT membrane in the perpendicular direction. As the simulation frequency step increases, the frequency response curve gets smoother, and the reason has not been found out yet. In the post processing, we chose the center point on the CMUT membrane and displayed its displacement in the z-direction. Figure 12 shows that around 6MHz, the displacement reaches its maximum, which is consistent with the results from the eigenfrequency analysis.

We then ran a series of eigenfrequency analyses on the CMUT structure with different radii, and the first eigenfrequencies are given in Table 4. The FEA results from Table 4 will be compared with the simulation results of the behavioral model in Chapter 4.

Table 4. The first eigenfrequencies for CMUT membrane with different radii.

Radius (μm)	32	35	40	45	50
First eigenfrequency (MHz)	5.9375	4.9464	3.7860	2.9905	2.4184

The eigenfrequency analysis is based only on mechanical plate theories, in which the electrostatic spring softening effect is not considered. In order to take the electrostatic spring softening effect into consideration, we needed to run a static analysis under a fixed DC bias first, then by changing the 'Initial value' to 'Current solution' from either 'Initial value expression' or 'Initial value expression evaluated using current solution' in the 'Solver Manager', we ran an eigenfrequency analysis. In this way, the obtained resonant frequencies will include the effects of the DC bias.

From the analyses above, it is obvious that the CMUT membrane with a radius of 50μm meets our specifications in terms of pull-in voltage and resonant frequencies. Therefore, we mainly focused on the simulations of the CMUT membrane with a radius of 50μm. Since the pull-in voltage of the CMUT membrane with a radius of 50μm is 102V, we apply a series of DC biases from 70V to 100V, and the first resonant frequencies are given in Table 5.

Table 5. First resonant frequencies considering the electrostatic spring softening effect of the CMUT membrane with a radius of 50μm.

DC bias (V)	70	75	80	85	90	95	100
Resonant frequency (MHz)	2.20	2.15	2.09	2.01	1.89	1.70	1.17

Table 5 shows that even when the applied DC bias is almost as high as the pull-in voltage, the first resonant frequency still remains above 1MHz, which is ideal for our purposes. Thus, we chose 50μm as the radius in our new design.

In the previous simulations, the CMUT membrane and the bottom electrode were of the same size, as shown in Figure 6. However, this is unachievable in the actual microfabrication process. Considering the design rule restrictions [13], the radii of the CMUT membrane and the bottom electrode were set to 53μm and 47μm in the layout design respectively[2]. Table 6 gives the final finite element analyses of the CMUT membrane with such geometric parameters.

Table 6. Simulations of the CMUT membrane with the new geometric parameters.

Radius of membrane (μm)	Radius of electrode (μm)	Pull-in voltage (V)	First eigenfrequency (MHz)	Applied voltage (V)	Modified first resonant frequency (MHz)
53	47	91	2.1491	80	1.6838

The applied voltage in the simulations shown in Table 6 was 80 V, which was approximately 90% of the pull-in voltage. This is due to the fact that the sensitivity of the CMUT increases as the applied DC bias approaches the pull-in voltage. The important parameters of CMUT cells on one die in the layout and their values are given in Table 7.

[2] We violated the following design rules in the layout design: POLY1 enclose ANCHOR1 by 4.0um, POLY1 enclose POLY1_POLY2_VIA by 4.0um, POLY1 enclose POLY2 by 4.0um, POLY2 enclose POLY1_POLY2_VIA by 4.0um; In this design, we let POLY1 enclose ANCHOR1 by 3.0 um, POLY2 enclose POLY1_POLY2_VIA by 3.0um, and in some areas POLY2 fully covers POLY1. The reason for these violations is to make full use of the available space in order for the devices to achieve the ideal functions.

Table 7. Important parameters of a CMUT cell.

Symbol	Representation	Value
a_m	Radius of the CMUT membrane	53μm
a_e	Radius of the bottom Electrode	47μm
N	Number of CMUT cells	5041
d_g	Gap distance between the membrane and electrode	0.75μm
d_m	Thickness of the CMUT membrane	1.5μm
ε_m	Relative permittivity of the membrane material	11.68
Y_m	Young's modulus of the membrane material	160×10^9 N m^{-2}
ρ_m	Density of the membrane material	2320 kg m^{-3}
σ_m	Poisson's ratio of the membrane material	0.22

The layout of CMUT cells array was drawn using L-Edit from MEMS Pro v6.0 (SoftMEMS, CA, USA). Figure 13 shows the top view of one of the CMUT cells.

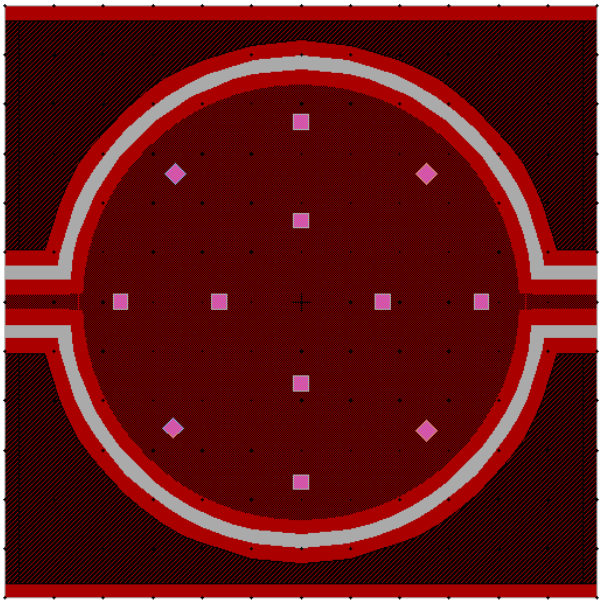

Figure 13. Top view of a CMUT cell in the layout.

CMUT cells with 2 and 4 bottom electrodes were also included in the layout. The top views of both cell types are presented in Figure 14.

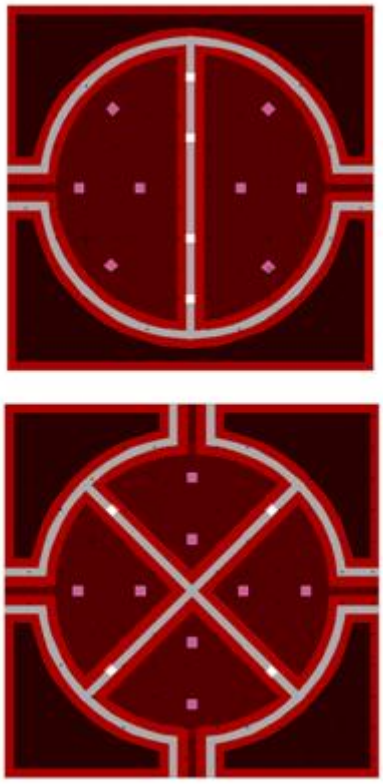

Figure 14. Top views of CMUT cells with 2 (top) and 4 (bottom) bottom electrodes.

We chose 208PGA as our package type, which offers 208 bonding pads on each die. On each die, there are 71 rows of CMUT cells and in each row the number of CMUT cells is also 71. The CMUT cells of each row are electrically connected in parallel; thus the CMUT cells in each row are simultaneously actuated by the same voltage. The top view of the whole layout with a side length of 10mm is given in Figure 15, and Figure 16 provides a zoomed view of the top left corner and bottom right corner.

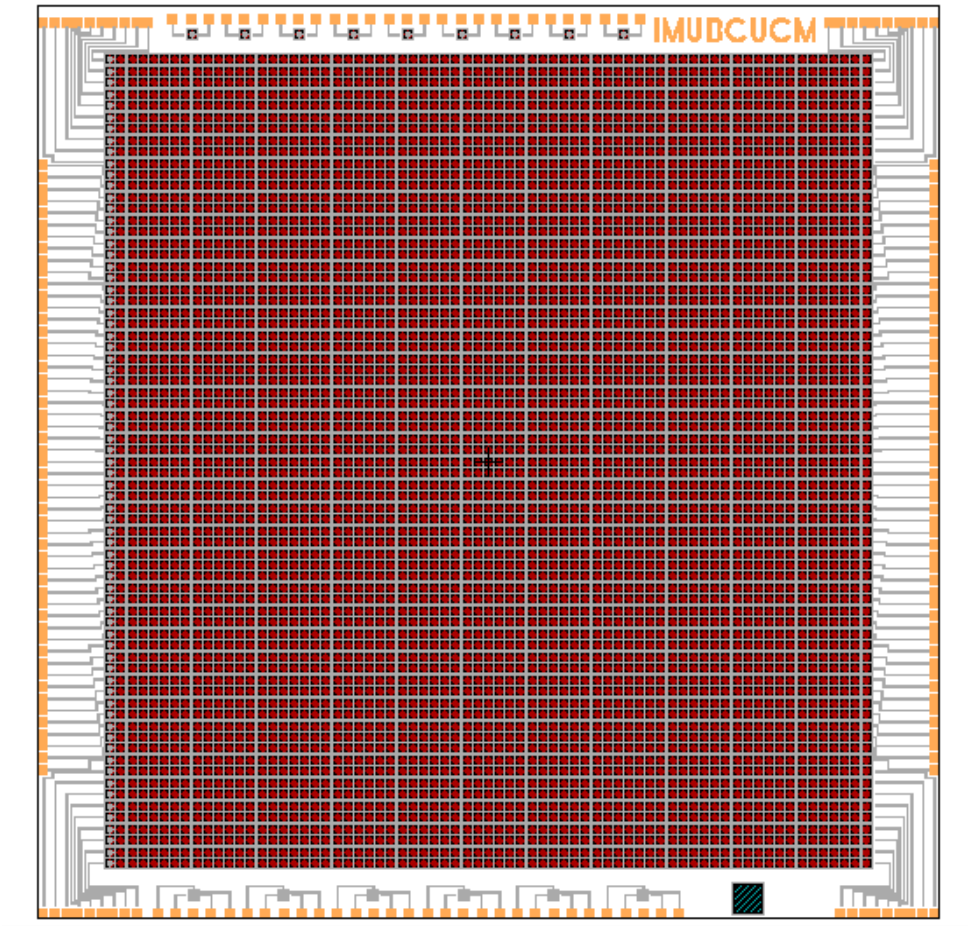

Figure 15. Top view of the whole layout.

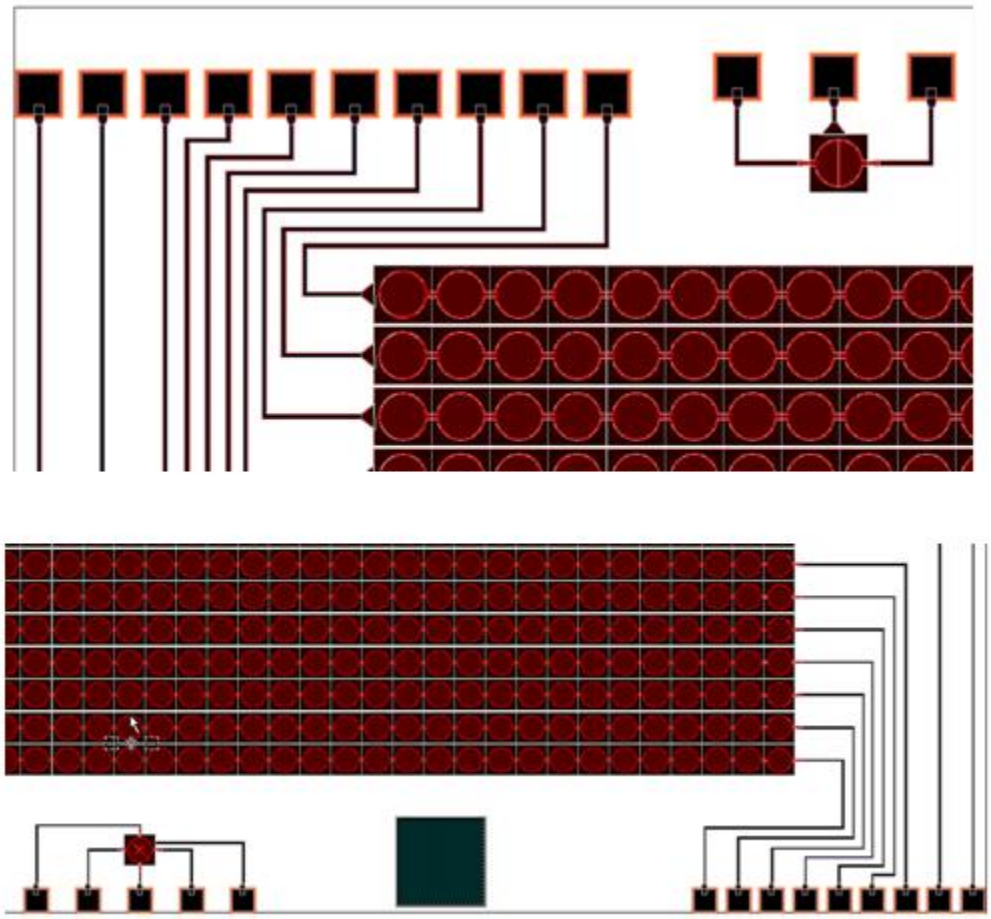

Figure 16. A zoomed view of the top left corner (top) and the bottom right corner (bottom) of the layout.

Chapter 3

Behavioral Modeling of CMUTs

3.1 The Mass-Spring-Damper Model

The mass on a spring is not new to students who have taken courses on fundamental physics. And the mass-spring-damper model is widely used as an important component of the basic model not only in the fields as distinct as elasticity, electric circuits, acoustics, statistical mechanics, etc., but also in microsystems such as the modeling of MEMS and NMES devices. The foundation of modeling electrostatic-elastic systems using the mass-spring-damper model is based upon several approximations, mainly concerning geometry [14]. Here, we assumed the geometric effects (deflections of membranes) and fringing effects are negligible, hence we could derive the behavioral model for a CMUT cell based on the mass-spring-damper system. As in [1], in this work we also treated the CMUT cell as a movable plate capacitor with one degree-of-freedom, and used the mass-spring-damper model to approximate the movable plate capacitor. All the important parameters in the behavioral modeling of CMUTs are listed in Table 8, and the sketch of a mass-spring-damper model is given in Figure 17.

Table 8. Important parameters in the behavioral modeling of CMUTs.

Symbol	Representation and Unit
k	Effective spring constant ($N \cdot m^{-1}$)
m_0	Effective mass (kg)

Symbol	Representation and Unit
B	Damping from the acoustic medium ($1 \cdot \Omega^{-1}$)
f	Force exerted on the acoustic medium (N)
v	CMUT membrane velocity (m s^{-1})
v_{DC}	Membrane DC velocity (m s^{-1})
v_{AC}	Membrane AC velocity (m s^{-1})
x	Center displacement of the CMUT membrane (m)
F_{sp}	Restoring spring force (N)
x_{sp}	Displacement at the end of the spring from its resting position (m)
y	Deflection of a clamped diaphragm (m)
y_0	Maximum deflection of a clamped diaphragm (m)
r	Radial position of a point on the membrane (m)
P	Load pressure on a diaphragm (N m^{-2})
$F_{capacitor}$	Capacitor force (N)
F_{mass}	Mass force (N)
u_{DC}	Applied DC bias (V)
u_{AC}	Applied AC excitation (V)
S	Area of a CMUT cell (m^2)

Symbol	Representation and Unit
k_{soft}	Spring constant considering the electrostatic spring softening effect ($N \cdot m^{-1}$)
N_{rr}^{*}	Initial tension in the pure membrane approximation (N)
ω_k	k^{th} resonant frequency of a pure membrane or a plate (Hz)
U_{mn}	Natural modes of a vibrating plate (m)
U	General membrane displacement (m)
$U_{\max}$	General center membrane displacement (m)
U_{shape}	Shape function of the membrane curve
U_{DC}	DC displacement (m)
C_{DC}	DC capacitance (F)
i_{DC}	DC input current (A)
$U_{DC,RMS}$	The RMS value of the DC displacement (m)
W_c	Electrical energy stored in the capacitor (J)
U_{AC}	AC displacement (m)
C_{AC}	AC capacitance (F)
i_{AC}	AC input current (A)
η_k	The k^{th} modal participation factor
F_{el}	Electrostatic force voltages (N)

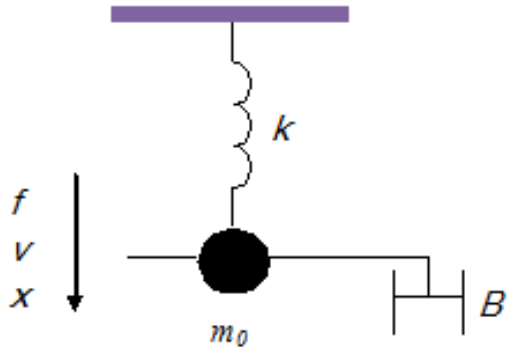

Figure 17. Sketch of a mass-spring-damper model.

In the previous figure, *k* represents the effective spring constant, while m_0 is the effective mass of the CMUT membrane. *B* is the damping due to the acoustic medium, *f* is the force exerted by the CMUT membrane on the acoustic domain and *v* is the membrane velocity. In [1], *x,* the displacement of the CMUT membrane, was considered to be uniform all over the membrane and thus resulted in a piston-like movement of the membrane. In the present work, x was considered only as the displacement at the center of the CMUT membrane, and a mode shape approximation was used instead to obtain a more realistic CMUT behavioral model.

3.1.1 The Effective Spring Constant and the Electrostatic Spring Softening Effect

The effective spring constant could be calculated from Hooke's law of elasticity, which mathematically states that:

$$F_{sp} = -kx_{sp}, \tag{1}$$

where F_{sp} is the restoring forced exerted by the material (N or $kg \cdot m \cdot s^{-2}$) - in this case it should be the restoring spring force that equals the electrostatic force in quantity and drives the CMUT membrane to its resting position; x_{sp} is the displacement at the end of the spring from its equilibrium position (m), which, in this case, is displacement of the center of the CMUT membrane from its resting position.

From the theories of diaphragm, the deflection y of a clamped diaphragm loaded by pressure P at any radial distance r is given by (2) [15]:

$$y = \frac{3\left(1-\sigma_m^2\right)P}{16Y_m d_m^3}\left(a^2 - r^2\right)^2 , \tag{2}$$

where Y_m is the Young's modulus, d_m is the thickness of the membrane, σ_m is the Poisson's ratio, and a is the radius of the membrane. The maximum deflection y_0 occurs at the center where r=0 and is:

$$y_0 = \frac{3\left(1-\sigma_m^2\right)a^4 P}{16Y_m d_m^3} . \tag{3}$$

Since the restoring spring force is equal to the electrostatic force before the membrane collapses, pressure P should be equal to the restoring spring force over area. Therefore,

$$y_0 = \frac{3\left(1-\sigma_m^2\right)a^4}{16Y_m d_m^3} \cdot \frac{-F_{sp}}{\pi a^2} = \frac{3\left(1-\sigma_m^2\right)a^2}{16\pi Y_m d_m^3} \cdot \left(-F_{sp}\right) . \tag{4}$$

Since,

$$F_{sp} = -k \cdot y_0 , \tag{5}$$

thus,

$$k = \frac{-F_{sp}}{y_0} = \frac{16\pi Y_m d_m^3}{3\left(1-\sigma_m^2\right)a^2} . \tag{6}$$

In the deduction process, the pressure *P* is assumed to have a certain constant value. However, as discussed above, when the membranes displaces in the +*x* direction, the equivalent electrostatic pressure (for an applied DC bias) will increase as well, giving a nonlinear dependence of the equivalent pressure on the displacement. This positive feedback effect results in the well-known phenomena of "spring softening," and modeled as an equivalent change in the effective spring constant.

The deduction of the modified effective spring constant can be found in [2], which is simplified as follows: since the CMUT membrane can be treated as a movable plate capacitor with one degree-of-freedom, we have:

$$F_{capacitor} + F_{sp} = F_{mass}, \tag{7}$$

where the force exerted by the capacitor can be calculated as:

$$F_{capacitor} = -\frac{d}{dx}\left(\frac{1}{2}Cu_{DC}^2\right) = -\frac{1}{2}u_{DC}^2\left[\frac{d}{dx}\left(\frac{\varepsilon_0 S}{d_0 - x}\right)\right] = \frac{\varepsilon_0 S u_{DC}^2}{2\left(d_0 - x\right)^2}. \tag{8}$$

Here d_0 is the thickness of the effective gap between the CMUT membrane and the bottom electrode, and is given by (9):

$$d_0 = d_g + \frac{d_m}{\varepsilon_m}, \tag{9}$$

in which d_g is the thickness of the actual gap and ε_m is the relative permittivity of the membrane material. Thus we have:

$$m_0 \frac{d^2 x}{dt^2} - \frac{\varepsilon S u_{DC}^2}{2\left(d_0 - x\right)^2} + kx = 0. \tag{10}$$

Performing a first order Taylor expansion of the second term in equation (10) at the point *x*=0, we have:

$$m_0 \frac{d^2x}{dt^2} - \left[\frac{\varepsilon S u_{DC}^2}{2d_0^2} + \frac{\varepsilon S u_{DC}^2}{d_0^3} x \right] + kx = 0 . \tag{11}$$

Thus,

$$m_0 \frac{d^2x}{dt^2} + \left(k - \frac{\varepsilon S u_{DC}^2}{d_0^3} \right) x = \frac{\varepsilon S u_{DC}^2}{2d_0^2} . \tag{12}$$

Therefore, the modified effective spring constant considering the electrostatic spring softening effect is given by:

$$k_{soft} = k - \frac{\varepsilon_0 S V_{DC}^2}{d_0^3} = \frac{16\pi Y_m d_m^3}{3\left(1-\sigma_m^2\right)a^2} - \frac{\varepsilon_0 S V_{DC}^2}{d_0^3} . \tag{13}$$

So we expect to see a drop in the resonant frequency as the applied DC bias increases.

3.1.2 The Effective Mass

In this behavioral model, the effective mass of the CMUT membrane is a lumped parameter that determines the inertial force acting upon the CMUT membrane. It is part of the 'real' mass of the membrane that has impact on the motion of the system. In previous chapters where the design and characterization of CMUTs are discussed, the chosen CMUT structures have circular shapes. Therefore, we will only discuss the circular shape here. There are two types of approximations for the CMUT membrane deformation dynamics: pure membrane approximation and plate approximation. A pure circular membrane is a skin stretched over a frame under an initial tension N_{rr}^* [16] and its bending stiffness *D* is negligible, where *D* is given by (14):

$$D = \frac{Y_m d_m^3}{12\left(1-\sigma_m^2\right)} . \tag{14}$$

The natural frequencies of a membrane are given by (15) [16]:

$$\omega_k = \omega_{mn} = \frac{(\lambda a)_{mn}}{a}\sqrt{\frac{N_{rr}^*}{\rho_m d_m}}, \tag{15}$$

where ρ_m is the density of the membrane material, and $(\lambda a)_{mn}$ are the roots (identified by m=0, 1, 2, …in ascending order) of the n[th] order Bessel function of the first kind, given by (16):

$$J_n(\lambda a) = 0. \tag{16}$$

However, in reality, the initial tension N_{rr}^* is difficult to calculate and to predict, and it varies with different fabrication conditions and techniques.

For the plate approximation, we consider the CMUT membrane to be a vibrating circular plate, and the natural mode components of the circular plate model are given by (17) [16]:

$$U_{mn}(r,\theta) = \left[J_n\left((\lambda a)_{mn}\frac{r}{a}\right) - \frac{J_n\left((\lambda a)_{mn}\right)}{I_n\left((\lambda a)_{mn}\right)} I_n\left((\lambda a)_{mn}\frac{r}{a}\right)\right]\cos n(\theta - \varphi), \tag{17}$$

where the values of $(\lambda a)_{mn}$ are the roots of the equation (18) [16]:

$$J_n(\lambda a)\frac{dI_n}{dr}(\lambda a) - \frac{dJ_n}{dr}(\lambda a) I_n(\lambda a) = 0, \tag{18}$$

and are given in Table 9. *m* is the number of concentric circles and *n* is the number of diametral lines in the mode shapes. The natural frequencies are given by (19) [16]:

$$\omega_{mn} = \frac{(\lambda a)_{mn}^2}{a^2}\sqrt{\frac{D}{\rho_m d_m}}, \tag{19}$$

where $I_n(\lambda a)$ is the n[th] order modified Bessel function of the first kind. Thus the natural frequencies ω_{mn} can be theoretically calculated because from (19) we can see that they are defined by the material properties and geometric parameters of the CMUT membrane. Some values of the roots $(\lambda a)_{mn}$ are shown in Table 9.

Table 9. Some values for roots $(\lambda a)_{mn}$ [16].

m \ n	0	1	2	3
0	3.196	4.611	5.906	7.143
1	6.306	7.799	9.197	10.537
2	9.440	10.958	12.402	13.795
3	12.577	14.108	15.579	17.005

If we consider the first mode, where m=n=0, from (14) and (19), we have:

$$\omega_{00} = \frac{(\lambda a)_{00}^2}{a^2}\sqrt{\frac{D}{\rho_m d_m}} = \frac{3.196^2}{a^2}\sqrt{\frac{Y_0 d_m^2}{12\rho_m\left(1-\sigma_m^2\right)}}\,. \tag{20}$$

Equating (20) with the lumped parameter resonant frequency expression given by (21):

$$\omega_0 = \sqrt{\frac{k}{m_0}}\,, \tag{22}$$

we have:

$$\sqrt{\frac{k}{m_0}} = \frac{3.196^2}{a^2}\sqrt{\frac{Y_0 d_m^2}{12\rho_m\left(1-\sigma_m^2\right)}}\,. \tag{23}$$

Considering the effective spring constant without the electrostatic spring softening effect and plugging (6) in (23), we have the effective mass m_0 given by (24):

$$m_0 = N0.613\pi a^2 d_m \rho_m\,. \tag{24}$$

Now that we have the effective spring constant and the effective mass, we can continue derivation of the behavioral model of CMUTs.

The membrane displacement of a CMUT cell $U(r)$ can be described by the displacement at the center of the membrane $U_{\max}$ and a shape function of the membrane curve $U_{shape}(r)$ as given by (25) [17]:

$$U(r) = U_{\max} \cdot U_{shape}(r). \tag{25}$$

In practice, we apply a relatively large DC bias superimposed with an AC excitation with a smaller amplitude. Both the DC bias and the AC excitation will cause the displacement of the CMUT membrane. For clarity, we divide the total displacement of the CMUT membrane into two components, the DC bias component and the AC excitation component.

3.2 The DC Bias Component

The CMUT membrane displacement due to the DC bias can be given by (26) [17]:

$$U_{DC}(x, r) = x \cdot \left(1 - \frac{r^2}{a^2}\right)^2, \tag{26}$$

where *x* is the displacement at the center of the membrane which varies with the DC bias applied to the electrodes, and $\left(1 - \frac{r^2}{a^2}\right)^2$ is the shape function. As could be seen later in the discussion of the AC excitation component, the DC displacement can be considered as one special kind of AC displacement with an extremely low frequency. Therefore, it could also be represented by (44). However, the difference between the shape function in (26) and (44) with respect to a fixed radius *a* is very small based on the calculation results using Mathematica (Wolfram Research, Inc., Champaign, IL, USA), so here the shape function of the DC displacement uses this polynomial as an approximation.

Thus, the membrane capacitance caused by the DC bias component is given by (27):

$$
\begin{aligned}
C_{DC}(x) &= 2\int_0^a \frac{n\varepsilon_0 \pi r dr}{d_0 - U_{DC}(x,r)} \\
&= 2\int_0^a \frac{n\pi\varepsilon_0 r dr}{d_0 - x\cdot\left(1-\frac{r^2}{a^2}\right)^2} = N\pi a^2\varepsilon_0 \frac{\arctan h\left(\frac{x}{\sqrt{xd_0}}\right)}{\sqrt{xd_0}} \\
&\approx N\pi a^2\varepsilon_0 \frac{\left(\frac{\sqrt{x}}{\sqrt{d_0}} + \frac{1}{3}\cdot\frac{x^{3/2}}{{d_0}^{3/2}} + \frac{1}{5}\cdot\frac{x^{5/2}}{{d_0}^{5/2}} + \frac{1}{7}\cdot\frac{x^{7/2}}{{d_0}^{7/2}}\right)}{\sqrt{xd_0}} \\
&= N\pi a^2\varepsilon_0\left(\frac{1}{d_0} + \frac{1}{3}\cdot\frac{x}{d_0^2} + \frac{1}{5}\cdot\frac{x^2}{d_0^3} + \frac{1}{7}\cdot\frac{x^3}{{d_0}^4}\right)
\end{aligned}, \tag{27}
$$

where N is the number of CMUT cells on one die, $\arctan h\left(\frac{x}{\sqrt{xd_0}}\right)$ is one type of inverse hyperbolic functions and is given by (28):

$$
\arctan hx = \frac{1}{2}\ln\frac{1+x}{1-x}, |x| < 1. \tag{28}
$$

In equation (28), x is the independent variable of function arctanh$x$, not the center displacement of the CMUT membrane. Since $\left|\frac{x}{\sqrt{xd_0}}\right| < 1$, we can perform the Taylor expansion of the inverse hyperbolic function $\arctan h\left(\frac{x}{\sqrt{xd_0}}\right)$ at x=0 using $\arctan h(x) = \sum_{n=0}^{\infty}\frac{x^{2n+1}}{2n+1}$. So we have equation (27). From (27) we can see the capacitance is a function of x, which is the displacement at the center of the membrane. This is similar to the capacitance in the piston-like model obtained in [1].

Therefore, the input current caused by the DC bias is given by (29):

$$
\begin{aligned}
i_{DC} &= C_{DC}(x)\frac{du_{DC}}{dt} + u_{DC}\frac{dC_{DC}(x)}{dt} = u_{DC}\frac{dC_{DC}(x)}{dt} \\
&= N\pi a^2 \varepsilon_0 u_{DC}\frac{d}{dt}\left(\frac{1}{d_0} + \frac{1}{3}\cdot\frac{x}{d_0^2} + \frac{1}{5}\cdot\frac{x^2}{d_0^3} + \frac{1}{7}\cdot\frac{x^3}{d_0^4}\right) \\
&= N\pi a^2 \varepsilon_0 u_{DC}\left(\frac{1}{3d_0^2}v_{DC} + \frac{2x}{5d_0^3}v_{DC} + \frac{3x^2}{7d_0^4}v_{DC}\right)
\end{aligned}
\quad . \tag{29}
$$

where u_{DC} is the applied DC bias. If we only apply a DC bias on the CMUT membrane, there will be no current, so in reality the DC input current is always 0. The reason I included it in the behavioral model is by the requirements of VHDL-AMS (two voltage sources u_{DC} and u_{AC}, two current expressions i_{DC} and i_{AC}).

With u (voltage) and i (current) characterizing the energy exchange in the electrical domain, we use v (membrane velocity) and f (force exerted on the medium) to measure its interaction with the mechanical domain. Hence, the behavioral model the CMUTs can be represented by a two-port model as shown in Figure 18.

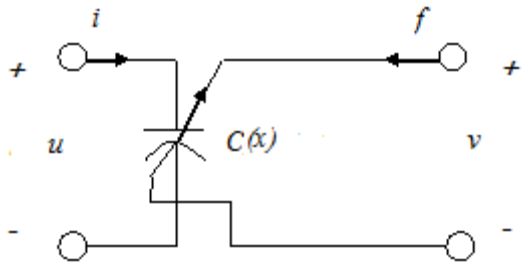

Figure 18. Sketch of the two-port behavioral model of CMUTs.

In Figure 18, the arrows indicate the positive directions of the input current and force, i_{AC} and $C_{AC}(t,r)$ are the capacitance and input current caused by the AC excitation which will be discussed later. The power conservation law [18] gives us:

$$
u \cdot i + v \cdot f = \frac{dW_c}{dt}, \tag{30}
$$

where u is the total applied voltage and is given by (31):

$$u = u_{DC} + u_{AC}, \tag{31}$$

and W_c represents the electrical energy stored in the capacitor, and is equal to:

$$W_c = \frac{Q^2}{2C(q)} = \frac{1}{2}Qu. \tag{32}$$

Thus,

$$u.dQ + f.d\left[U_{DC}(x,r) + U_{AC}(r,\theta)\right] = d\left[\frac{C_{total}(x)u^2}{2}\right], \tag{33}$$

where $C_{total}(x)$ is the total capacitance considering the effects of the DC capacitance and AC capacitance together. When considering each component, we assume the other is 0, thus the relationship between DC capacitance $C_{DC}(x,r)$ and AC capacitance $C_{AC}(r,\theta)$ cannot be simply interpreted as addition or multiplication. But the DC capacitance is much larger than the AC capacitance as could been seen later, so here the effect of the AC capacitance is neglected for simplicity. Also, since the DC displacement is much larger than the AC displacement as could be seen later, we neglect the AC displacement as well and we only use the center displacement of the CMUT membrane x to represent the DC displacement. Therefore, equation (33) could be simplified as:

$$u.dQ + f.dx = d\left[\frac{C(x)u^2}{2}\right]. \tag{34}$$

Therefore,

$$f = \frac{d}{dx}\left[\frac{C_{DC}(x)\left(u_{DC}+u_{AC}\right)^2}{2}\right] - \left(u_{DC}+u_{AC}\right)\frac{d}{dx}\left[C_{DC}(x)\left(u_{DC}+u_{AC}\right)\right]$$
$$= \frac{-\left(u_{DC}+u_{AC}\right)^2}{2}\frac{dC_{DC}(x)}{dx} \quad . \tag{35}$$
$$= \frac{-(u_{DC}+u_{AC})^2}{2} N\pi a^2 \varepsilon_0 \left(\frac{1}{3d_0^2}+\frac{2x}{5d_0^3}+\frac{3x^2}{7d_0{}^4}\right)$$

Considering the effective mass and the effective spring constant, we have:

$$f = m_0\frac{dv}{dt} + k_{soft}\int v dt - \frac{\left(u_{DC}+u_{AC}\right)^2}{2} N\pi a^2 \varepsilon_0 \left(\frac{1}{3d_0^2}+\frac{2x}{5d_0^3}+\frac{3x^2}{7d_0{}^4}\right) \quad . \tag{36}$$

In statistics, the RMS (root mean square) value of a set of data is the square root of the arithmetic mean of the squares of the original data. It is a statistical measure of the magnitude of a varying quantity and is used in various fields, including electrical engineering, where varying signals (in time or space) are replaced with their RMS value, in order to account for an energy-based equivalence. According to the definition, the RMS value of a set of n values $\{x_1, x_2, ..., x_n\}$ is given by (37):

$$x_{rms} = \sqrt{\frac{x_1^2 + x_2^2 + \cdots + x_n^2}{n}} \, . \tag{37}$$

Therefore, the RMS value of the DC bias displacement component is given by (38):

$$U_{DC,RMS} = \sqrt{\frac{1}{\pi a^2}\cdot\frac{1}{a}\int_0^a \left(x\left(1-\frac{r^2}{a^2}\right)^2\right)^2 \cdot 2\pi r dr} \, . \tag{38}$$

The computation leads to:

$$U_{DC,RMS} = \frac{8\sqrt{770}}{1155} \approx 0.1922x \, . \tag{39}$$

Let

$$y = U_{DC,RMS}\,. \tag{40}$$

Plugging (39) and (40) in (27), we have:

$$C_{DC}(y) = N\pi a^2 \varepsilon_0 \left(\frac{1}{d_0} + \frac{5.2029y}{3d_0^2} + \frac{5.2029^2 y^2}{5d_0^3} \right), \tag{41}$$

$$\begin{aligned} i_{DC} &= C_{DC}(x)\frac{du_{DC}}{dt} + u_{DC}\frac{dC_{DC}(x)}{dt} = u_{DC}\frac{dC_{DC}(x)}{dt} \\ &= N\pi a^2 \varepsilon_0 u_{DC} \frac{d}{dt}\left(\frac{1}{d_0} + \frac{5.2029y}{3d_0^2} + \frac{5.2029^2 y^2}{5d_0^3} \right) \\ &= N\pi a^2 \varepsilon_0 u_{DC} \left(\frac{5.2029}{3d_0^2} v_{DC} + \frac{2\cdot 5.2029^2 y}{5d_0^3} v_{DC} \right) \end{aligned} \quad . \tag{42}$$

So here we use the RMS value of the displacement to represent the actual DC displacement, which is a more accurate approximation than (29). Thus, (36) could be re-written as:

$$\begin{aligned} f &= m_0 a + k_{soft}\int v dt - \frac{u^2}{2} N\pi a^2 \varepsilon_0 \left(\frac{5.2029}{3d_0^2} + \frac{2\cdot 5.2029^2 y}{5d_0^3} \right) \\ &= m_0 \frac{dv}{dt} + k_{soft}\int v dt - \frac{(u_{DC}+u_{AC})^2}{2} N\pi a^2 \varepsilon_0 \left(\frac{5.2029}{3d_0^2} + \frac{2\cdot 5.2029^2 y}{5d_0^3} \right) \end{aligned}. \tag{43}$$

3.3 The AC Excitation Component

As aforementioned, the actual displacement of the CMUT membrane can be considered as the combination of two components, the DC bias component and the AC excitation component. For the AC excitation component, we need to consider as well the dynamic effects. In reality, a single excitation can excite a series of natural mode components in various amounts, and we use a modal participation factor to define the amount each natural mode component contributes to the total displacement of a vibrating plate. Thus the total displacement of a vibrating plate is given by (44) [16]:

$$U_{AC}(t,r,\theta)=\sum_{k=1}^{\infty}\eta_k(t)U_k(r,\theta), \tag{44}$$

where $U_k(r,\theta)$ is the k[th] natural mode and can be given by (18), $\eta_k(t)$ is the modal participation factor for the k[th] natural mode. In this work, we will only derive the modal participation factor for the first mode $\eta_1(t)$, which is when m=0, n=0, and $(\lambda a)_{00}=3.196$ because it is much larger than the rest considering the frequency of the AC excitation we will apply in the characterization of the devices.

The electrical energy stored in the plate can be calculated from (45):

$$W_c=\frac{1}{2}(u_{DC}+u_{AC})^2 C, \tag{45}$$

where $C=\dfrac{\varepsilon_0\pi a^2}{d_0-U_{DC,RMS}-U_{AC,RMS}}$, $U_{DC,RMS}$ and $U_{AC,RMS}$ are the RMS values of the DC bias and AC excitation components respectively.This is based on the fact that we use the RMS values of the DC and AC displacements to represent the actual displacements for simplicity. Since the DC bias can be considered as one special kind of AC excitation with the frequency 0, the DC bias component, under this circumstance, can also be represented by an expression similar to (44). For the capacitance of the CMUT vibrating plate, we need to consider the plate as a whole – to reduce the number of degrees of freedoms, the DC bias and AC excitation components are averaged in terms of their RMS value. The RMS DC bias and AC excitation components are given below:

$$\begin{aligned}U_{DC,RMS}&=\sqrt{\frac{1}{\pi a^2}\int_0^a\left(\eta_{1,DC}(t)J_0\left(3.196\frac{r}{a}\right)-\frac{J_0(3.196)}{I_0(3.196)}I_0\left(3.196\frac{r}{a}\right)\right)^2 2\pi r dr}\\&=\eta_{1,DC}(t)\sqrt{\frac{1}{\pi a^2}\cdot 0.2038\pi a^2}\\&=0.4514\eta_{1,DC}(t)\end{aligned}, \tag{46}$$

$$U_{AC,RMS} = \sqrt{\frac{1}{\pi a^2}\int_0^a \left(\eta_{1,AC}(t) J_0\left(3.196\frac{r}{a}\right) - \frac{J_0(3.196)}{I_0(3.196)} I_0\left(3.196\frac{r}{a}\right)\right)^2 2\pi r dr}$$
$$= \eta_{1,AC}(t)\sqrt{\frac{1}{\pi a^2}\cdot 0.2038\pi a^2} \quad . \tag{47}$$
$$= 0.4514\eta_{1,AC}(t)$$

The total electrical energy can also be written as,

$$W_c = F_{el}\left(d_0 - U_{DC,RMS} - U_{AC,RMS}\right), \tag{48}$$

where F_{el} is the electrostatic force. So, we have:

$$F_{el} = \frac{W_c}{d_0 - U_{DC,RMS} - U_{AC,RMS}} = \frac{\varepsilon_0 \pi a^2 \left(u_{DC} + u_{AC}\right)^2}{2\left(d_0 - U_{DC,RMS} - U_{AC,RMS}\right)^2} . \tag{49}$$

Thus, the load on the CMUT vibrating plate (N/m^2) is given by (50):

$$q(r,\theta,t) = \frac{\varepsilon_0 \left(u_{DC} + u_{AC}\right)^2}{2\left(d_0 - U_{DC,RMS} - U_{AC,RMS}\right)^2}, \tag{50}$$

and,

$$q(r,\theta,t) = q^*(r,\theta)e^{j\omega t}, \tag{51}$$

Hence, $\eta_1(t)$ can be calculated from the differential equation (52) [16]:

$$\ddot{\eta}_1 + 2\zeta_1\omega_1\dot{\eta}_1 + \omega_1^2\eta_1 = F_1^* e^{j\omega t}, \tag{52}$$

where ζ_1 is called the modal damping coefficient for the first mode, which is set to 0 in this work;

F_1^* is given by (53):

$$F_1^* = \frac{1}{\rho_m d_m N_1}\int_\theta \int_r q^* U_1 r dr d\theta, \tag{53}$$

where N_1 is given by (54):

$$N_1 = \int_\theta \int_r U_1^2 r dr d\theta . \tag{54}$$

For the DC modal participation factor, if $m = 0, n = 0$, we use N_{DC} to represent N_1 in this case.

And we have:

$$\begin{aligned}
N_{DC} &= \int_\theta \int_r \left(J_0\left(3.196\frac{r}{a}\right) - \frac{J_0(3.196)}{I_0(3.196)} I_0\left(3.196\frac{r}{a}\right) \right)^2 r dr d\theta \\
&= \int_0^{2\pi} d\theta \cdot \left[\int_0^a r \left(J_0\left(3.196\frac{r}{a}\right) - \frac{J_0(3.196)}{I_0(3.196)} I_0\left(3.196\frac{r}{a}\right) \right)^2 dr \right] \\
&= 2\pi a^2 \int_0^1 r' \left(J_0\left(3.196 r'\right) - \frac{J_0(3.196)}{I_0(3.196)} I_0\left(3.196 r'\right) \right)^2 dr' \\
&\approx 2\pi a^2 \times 0.101901 \\
&= 2 \times 3.14 \times \left(32 \times 10^{-6}\right)^2 \times 0.101901 \\
&\approx 6.55297 \times 10^{-10}
\end{aligned} \tag{55}$$

Since,

$$q(r,\theta,t) = q^*(r,\theta) e^{j\omega t}, \tag{56}$$

one has:

$$q_{DC}(r,\theta,t) = q_{DC}^*(r,\theta) = \frac{\varepsilon_0 u_{DC}^2}{\left(d_0 - U_{DC}\right)^2} . \tag{57}$$

We have therefore:

$$
\begin{aligned}
F_{DC}^{*} &= \frac{1}{\rho_m d_m N_{DC}} \int_r \int_\theta \left(q_{DC}^{*} U_1 \right) r dr d\theta \\
&= \frac{2\pi\varepsilon_0 u_{DC}^2}{\rho_m d_m N_{DC}} \int_0^a \frac{\left(J_0\left(3.196\frac{r}{a}\right) - \frac{J_0(3.196)}{I_0(3.196)} I_0\left(3.196\frac{r}{a}\right) \right) r dr}{\left(d_0 - U_{DC}\right)^2} \\
&= \frac{2\pi a^2 \varepsilon_0 u_{DC}^2}{\rho_m d_m N_{DC}} \int_0^1 \frac{\left(J_0\left(3.196r'\right) - \frac{J_0(3.196)}{I_0(3.196)} I_0\left(3.196r'\right) \right) r' dr'}{\left(d_0 - 0.4514\eta_{DC}\right)^2} \\
&= \frac{2\pi a^2 \varepsilon_0 u_{DC}^2}{\rho_m d_m N_{DC}} \cdot \frac{0.1645}{\left(d_0 - 0.4514\eta_{DC}\right)^2}
\end{aligned}
\tag{58}
$$

The magnitude of the modal participation factor $\hat{\eta}_k$ is given by (59) [16]:

$$
\hat{\eta}_k = \frac{F_k^{*}}{\omega_k^2 \sqrt{\left[1 - \left(\frac{\omega}{\omega_k}\right)^2\right]^2 + 4\zeta_k^2 \left(\frac{\omega}{\omega_k}\right)^2}} . \tag{59}
$$

Then the magnitude of the DC modal participation factor can be written as (60):

$$
\begin{aligned}
\hat{\eta}_{DC} &= \frac{F_{DC}^{*}}{\omega_{00}^2} \\
&= \frac{\frac{2\pi a^2 \varepsilon_0 u_{DC}^2}{\rho_m d_m N_{DC}} \cdot \frac{0.1645}{\left(d_0 - 0.4514\hat{\eta}_{DC}\right)^2}}{\omega_{00}^2}
\end{aligned}
\tag{60}
$$

For the AC modal participation factor, we have

$$
\begin{aligned}
N_{AC} &= \int_\theta \int_r \left(J_0\left(3.196\frac{r}{a}\right) - \frac{J_0(3.196)}{I_0(3.196)} I_0\left(3.196\frac{r}{a}\right) \right)^2 r dr d\theta \\
&= \int_0^{2\pi} d\theta \cdot \left[\int_0^a r \left(J_0\left(3.196\frac{r}{a}\right) - \frac{J_0(3.196)}{I_0(3.196)} I_0\left(3.196\frac{r}{a}\right) \right)^2 dr \right] \\
&= 2\pi a^2 \int_0^1 r' \left(J_0\left(3.196 r'\right) - \frac{J_0(3.196)}{I_0(3.196)} I_0\left(3.196 r'\right) \right)^2 dr' \\
&\approx 2\pi a^2 \times 0.101901 \\
&= 2 \times 3.14 \times \left(32 \times 10^{-6}\right)^2 \times 0.101901 \\
&\approx 6.55297 \times 10^{-10}
\end{aligned}
\quad . \qquad (61)
$$

Then we have:

$$
\begin{aligned}
F_{AC}^* &= \frac{1}{\rho_m d_m N_{AC}} \int_r \int_\theta \left(q_{AC}^* U_1 \right) r dr d\theta \\
&= \frac{2\pi \varepsilon_0 \hat{u}_{AC}^2}{\rho_m d_m N_{AC}} \int_0^a \frac{\left(J_0\left(3.196\frac{r}{a}\right) - \frac{J_0(3.196)}{I_0(3.196)} I_0\left(3.196\frac{r}{a}\right) \right) r dr}{\left(d_0 - U_{DC} - U_{AC}\right)^2} \\
&= \frac{2\pi \varepsilon_0 a^2 \hat{u}_{AC}^2}{\rho_m d_m N_{AC}} \int_0^1 \frac{\left(J_0\left(3.196 r'\right) - \frac{J_0(3.196)}{I_0(3.196)} I_0\left(3.196 r'\right) \right) r' dr'}{\left(d_0 - \eta_{DC} \left(J_0\left(3.196 r'\right) - \frac{J_0(3.196)}{I_0(3.196)} I_0\left(3.196 r'\right) \right) - \eta_{AC} \left(J_0\left(3.196 r'\right) - \frac{J_0(3.196)}{I_0(3.196)} I_0\left(3.196 r'\right) \right) \right)^2} \\
&= \frac{2\pi a^2 \varepsilon_0 \hat{u}_{AC}^2}{\rho_m d_m N_{AC}} \cdot \frac{0.1645}{\left(d_0 - 0.4514\left(\eta_{DC} + \eta_{AC}\right)\right)^2}
\end{aligned}
\quad . \qquad (62)
$$

So,

$$
\begin{aligned}
\hat{\eta}_{AC} &= \frac{F_{AC}^*}{\omega_{00}^2 \left[1 - \left(\frac{\omega}{\omega_{00}} \right)^2 \right]} \\
&= \frac{\frac{2\pi a^2 \varepsilon_0 \hat{u}_{AC}^2}{\rho_m d_m N_{AC}} \cdot \frac{0.1645}{\left(d_0 - 0.4514\left(\eta_{DC} + \eta_{AC}\right)\right)^2}}{\omega_{00}^2 \left[1 - \left(\frac{\omega}{\omega_{00}} \right)^2 \right]}
\end{aligned}
\quad . \qquad (63)
$$

Plugging (60) in (63), we have the magnitude of the AC modal participation factor:

$$\hat{\eta}_{AC} = \frac{F_{AC}^{*}}{\omega_{00}^{2}\left[1-\left(\frac{\omega}{\omega_{00}}\right)^{2}\right]} \approx \frac{0.329\pi a^{2}\varepsilon_{0}\hat{u}_{AC}^{2}}{\rho_{m}d_{m}N_{AC}\omega_{00}^{2}d_{0}^{2}\left[1-\left(\frac{\omega}{\omega_{00}}\right)^{2}\right]} \quad (64)$$

Now that we derived the AC modal participation factor, we can write the AC excitation component as in (65):

$$U_{AC}(t,r) = \frac{0.329\pi a^{2}\varepsilon_{0}u_{AC}^{2}(t)}{\rho_{m}d_{m}N_{AC}\omega_{00}^{2}d_{0}^{2}\left[1-\left(\frac{\omega}{\omega_{00}}\right)^{2}\right]}\cdot\left(J_{0}\left(3.196\frac{r}{a}\right)-\frac{J_{0}(3.196)}{I_{0}(3.196)}I_{0}\left(3.196\frac{r}{a}\right)\right) = p\cdot u_{AC}^{2}(t)\cdot\left(1.0557-2.6959\left(\frac{r}{a}\right)^{2}+1.7210\left(\frac{r}{a}\right)^{4}\right), \quad (65)$$

where $p = \frac{0.329\pi a^{2}\varepsilon_{0}}{\rho_{m}d_{m}N_{AC}\omega_{00}^{2}d_{0}^{2}\left[1-\left(\frac{\omega}{\omega_{00}}\right)^{2}\right]}$ .Thus, the capacitance caused by the AC excitation is written as (66):

$$\begin{aligned}
C_{AC}(t) &= 2N\int_{0}^{a}\frac{\varepsilon_{0}\pi r dr}{d_{0}-U_{AC}(t,r)} \\
&= 2N\int_{0}^{a}\frac{\pi\varepsilon_{0}r dr}{d_{0}-p\cdot u_{AC}^{2}(t)\left(1.0557-2.6959\left(\frac{r}{a}\right)^{2}+1.7210\left(\frac{r}{a}\right)^{4}\right)} \\
&= 2N\int_{0}^{a}\frac{\pi\varepsilon_{0}r dr}{d_{0}-p\cdot u_{AC}^{2}(t)\left(1.0557-2.6959\left(\frac{r}{a}\right)^{2}+1.7210\left(\frac{r}{a}\right)^{4}\right)} \\
&= 2N\pi a^{2}\varepsilon_{0}\left(\frac{10000}{\sqrt{pu_{AC}^{2}(t)\left(43801pu_{AC}^{2}(t)+6.8840\times10^{8}d_{0}\right)}}\left(\begin{array}{l}\arctan h\left(\frac{26959\,pu_{AC}^{2}(t)}{\sqrt{pu_{AC}^{2}(t)\left(43801pu_{AC}^{2}(t)+1.7210\times10^{18}d_{0}\right)}}\right)\\ +\arctan h\left(\frac{7461pu_{AC}^{2}(t)}{\sqrt{pu_{AC}^{2}(t)\left(43801pu_{AC}^{2}(t)+1.7210\times10^{18}d_{0}\right)}}\right)\end{array}\right)\right) \\
&\approx 2N\pi a^{2}\varepsilon_{0}\left(\frac{0.5000}{d_{0}}+\frac{0.1407\,pu_{AC}^{2}(t)}{d_{0}^{2}}+\frac{0.0874\left(pu_{AC}^{2}(t)\right)^{2}}{d_{0}^{3}}+\frac{0.0658\left(pu_{AC}^{2}(t)\right)^{3}}{d_{0}^{4}}\right)
\end{aligned} \quad (66)$$

The input current component caused by the AC excitation is therefore given by

$$
\begin{aligned}
i_{AC} &= C_{AC}(t)\frac{du_{AC}}{dt} + u_{AC}\frac{dC_{AC}(t)}{dt} \\
&= C_{AC}(t)\frac{du_{AC}}{dt} + u_{AC}\frac{dC_{AC}(t)}{du_{AC}}\cdot\frac{du_{AC}}{dt} \\
&\approx 2N\pi a^2\varepsilon_0\left(\frac{0.5000}{d_0} + \frac{0.1407\,pu_{AC}^2(t)}{d_0^2} + \frac{0.0874\left(pu_{AC}^2(t)\right)^2}{d_0^3} + \frac{0.0658\left(pu_{AC}^2(t)\right)^3}{d_0^4}\right)\frac{du_{AC}}{dt} \\
&+ u_{AC}\frac{du_{AC}}{dt}2N\pi a^2\varepsilon_0\left(\frac{0.2814\,pu_{AC}(t)}{d_0^2} + \frac{0.3497\left(p\right)^2 u_{AC}^3(t)}{d_0^3} + \frac{0.3950\left(p\right)^3 u_{AC}^5(t)}{d_0^4}\right) \\
&= 2\pi a^2\varepsilon_0\frac{du_{AC}}{dt}\left(\begin{array}{l}\dfrac{0.5000}{d_0} + \dfrac{0.1407\,pu_{AC}^2(t)}{d_0^2} + \dfrac{0.0874\left(pu_{AC}^2(t)\right)^2}{d_0^3} + \dfrac{0.0658\left(pu_{AC}^2(t)\right)^3}{d_0^4} \\ +u_{AC}\left(\dfrac{0.2814\,pu_{AC}(t)}{d_0^2} + \dfrac{0.3497\left(p\right)^2 u_{AC}^3(t)}{d_0^3} + \dfrac{0.3950\left(p\right)^3 u_{AC}^5(t)}{d_0^4}\right)\end{array}\right) .
\end{aligned}
\tag{67}
$$

Now that we have all the parameters in the behavioral model shown in Figure 18 worked out including the DC and AC capacitances, the DC and AC currents, and the expressions for the force exerted on the membrane *f*, and their relations with the membrane velocity *v*, we could verify this model in certain simulation software., which will be discussed in the next chapter.

Chapter 4

Simulation of the CMUT Behavioral Model

4.1 Settings in SLED (Schematic Link EDitor) and SMASH (AMS Simulation)

Equations (41), (42), (43), (66) and (67) are the main components of the behavioral model of the CMUT cell. However, these equations exhibit a large amount of non-linearities, which makes them difficult to implement in standard SPICE simulators. We have therefore used the standard modeling language VHDL-AMS (IEEE standard 1076.1-1999) for the implementation and simulation of the improved CMUT behavioral model. Saber (Synopsys, Inc., CA, USA), Simplorer (ANSYS, Inc., PA, USA) and SMASH 5.14.2 (DOLPHIN Integration, Meylan, France) are all multi-domain system modeling and simulation environments that allow user-defined VHDL-AMS models to be integrated with their own libraries and electronic components. In this work, SMASH 5.14.2 was chosen as the simulation software because of its mixed Spice/VHDL-AMS simulation capabilities.. Before being netlisted into SMASH 5.14.2, the schematics of the behavioral model of the CMUT cell as well as the other circuit components were first defined in SLED 1.5.2, which is a hierarchical schematic entry solution that allows designers to configure and graphically define a circuit schematic for their design.

Since we divided the total displacement of the CMUT membrane into two components, the DC bias component and the AC excitation component, we needed two voltage sources in the setup of the simulation environment, the DC bias and AC excitation, both of which are connected to the

electrical port of the CMUT. A resistor, representing the equivalent acoustic load impedance (to account for the acoustic radiation), was also needed, and it is connected to the mechanical port of the CMUT.

For the 'CMUT' symbol, in its external view written in VHDL-AMS, we wrote:

```
LIBRARY IEEE;
USE IEEE.MATH_REAL.all;
USE IEEE.FUNDAMENTAL_CONSTANTS.all;
USE IEEE.ELECTRICAL_SYSTEMS.all;
```

where "USE IEEE.MATH_REAL.all;" enables to define mathematical functions and constants such as "math_pi"; "USE IEEE.FUNDAMENTAL_CONSTANTS.all;" enables to define constants such as "phys_sp0"; and "IEEE.ELECTRICAL_SYSTEMS.all;" enables to define the electrical domain. All the geometric and structural parameters are fixed except for the frequency of the applied AC voltage. The properties of this symbol under the 'Properties' tab in the 'Object Explorer' are shown in Figure 19.

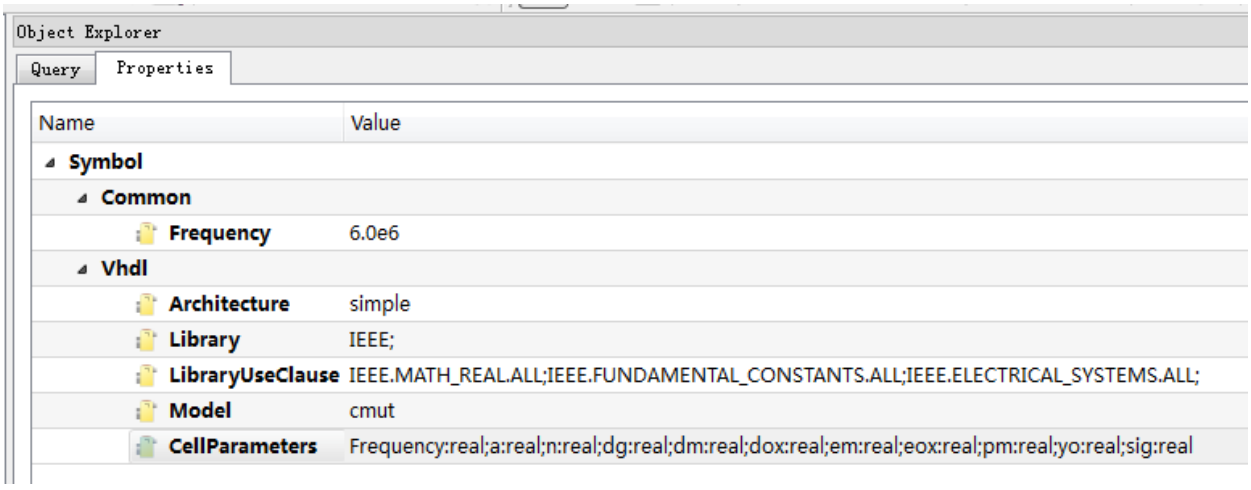

Figure 19. The properties of the 'Cmutwithac' symbol.

For the ‘Vac’ symbol, in its VHDL-AMS file, we defined the entity and architecture as below:

```
ENTITY Vac IS
  GENERIC (Amplitude: voltage:= 0.0;
           Frequency: REAL:= 3.0e6;
           Phase: REAL:= 0.0;
           AcMagnitude   : voltage := 15.0; -- AC magnitude (V)
           AcPhase : real    := 0.0  -- AC phase (degree)
           );

  PORT (TERMINAL e1,
                 e2: ELECTRICAL);
END ENTITY Vac;

ARCHITECTURE simple OF Vac IS
  QUANTITY v ACROSS i THROUGH e1 TO e2;
  -- for AC analysis
  quantity ac_spec    : real spectrum AcMagnitude, math_2_pi*AcPhase/360.0;

BEGIN

  v == Amplitude * sin(MATH_2_PI * Frequency * NOW + Phase) + ac_spec;

END ARCHITECTURE simple;
```

where the quantity ‘ac_spec’ is used for the small signal analysis when ‘Amplitude’ is set to 0. And the properties of the ‘Vac’ symbol under the ‘Properties’ tab in the ‘Object Explorer’ is shown in Figure 20.

bject Explorer

Query | Properties

Name	Value
Symbol	
Common	
Amplitude	0.0
Frequency	6.0e6
Phase	0.0
AcMagnitude	1.0
AcPhase	0.0
Vhdl	
Architecture	simple
Library	IEEE;
LibraryUseClause	IEEE.ELECTRICAL_SYSTEMS.all; IEEE.MATH_REAL.all;
Model	vac
CellParameters	Amplitude:voltage;Frequency:real;Phase:real;AcMagnitude:voltage;AcPhase:real;

Figure 20. The properties of Vac symbol.

For the ‘Vdc’ symbol, in its VHDL-AMS file, we defined the entity and architecture as below:

```
ENTITY Vdc IS
  GENERIC (Amplitude: voltage:= 15.0);

  PORT (TERMINAL e3,
                 e4  : ELECTRICAL);
END ENTITY Vdc;

ARCHITECTURE simple OF Vdc IS
  QUANTITY v ACROSS i THROUGH e3 TO e4;

BEGIN
  v == Amplitude;

END ARCHITECTURE simple;
```

and the properties of this symbol under the ‘Properties’ tab in the ‘Object Explorer’ is given in Figure 21.

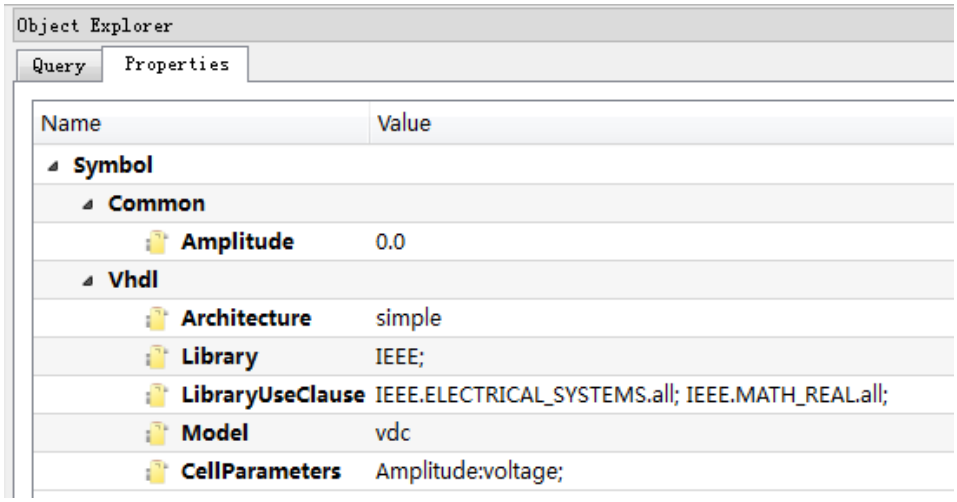

Figure 21. The properties of ‘Vdc’ symbol.

For the ‘Resistor’ symbol, in its VHDL-AMS file, we defined the entity and architecture as below:

```
ENTITY resistor IS
  GENERIC (value : RESISTANCE);

  PORT (TERMINAL m1,
                m2 : ELECTRICAL);
END ENTITY resistor;

ARCHITECTURE simple OF resistor IS
  QUANTITY v ACROSS i THROUGH m1 TO m2;

BEGIN

  v == i * value;

END ARCHITECTURE simple;
```

The damping coefficient B in the mass-spring-damper model is defined by (68) [1]:

$$B = N_a \pi a^2 Z_0 , \tag{68}$$

where Z_0 is the acoustic impedance $\left[kg \cdot m^{-2} \cdot s^{-1} \right]$ of the medium. The acoustic impedance is defined as the ratio of sound pressure p to particle velocity v at a single frequency, as given by (69):

$$Z_0 = \frac{p}{v} = \frac{J}{v^2} = \frac{p^2}{J} = \rho \cdot c . \tag{69}$$

The resistor here is inversely related to the characteristic acoustic impedance, and is given by (70):

$$Z_L = \frac{1}{N_a \pi a^2 Z_0} = \frac{1}{B} . \tag{70}$$

Since the acoustic impedance for air ($20°C$), water ($37°C$) and fatty tissue are 412 $kg \cdot m^{-2} \cdot s^{-1}$, $1.52 \times 10^6 kg \cdot m^{-2} \cdot s^{-1}$ and $1.33 \times 10^6 kg \cdot m^{-2} \cdot s^{-1}$ respectively, N_a is given by 71 (which is the number of CMUT cells in one row) and a is the effective radius (47μm), the load for air ($20°C$), water ($37°C$) and fat are thus $4.928\, k\Omega$, 1.336Ω and $1.527\,\Omega$. The properties of the resistor symbol in the 'Object Explorer' are given in Figure 22.

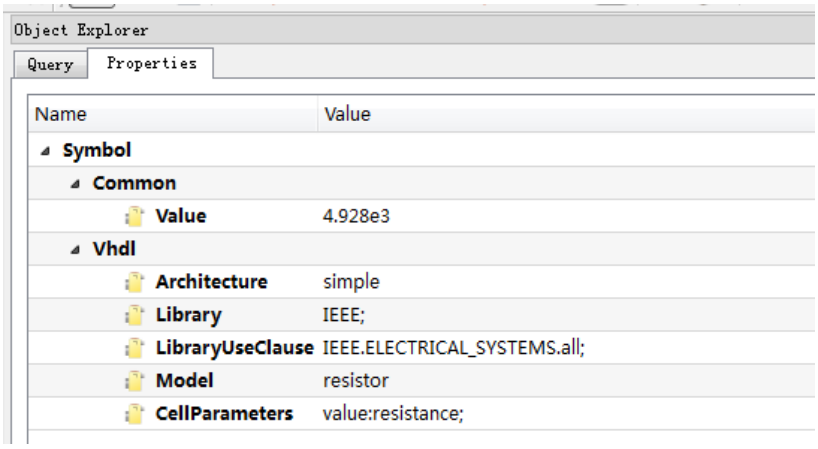

Figure 22. The properties of resistor symbol.

The schematic of the ‘testbench’ is shown in Figure 23.

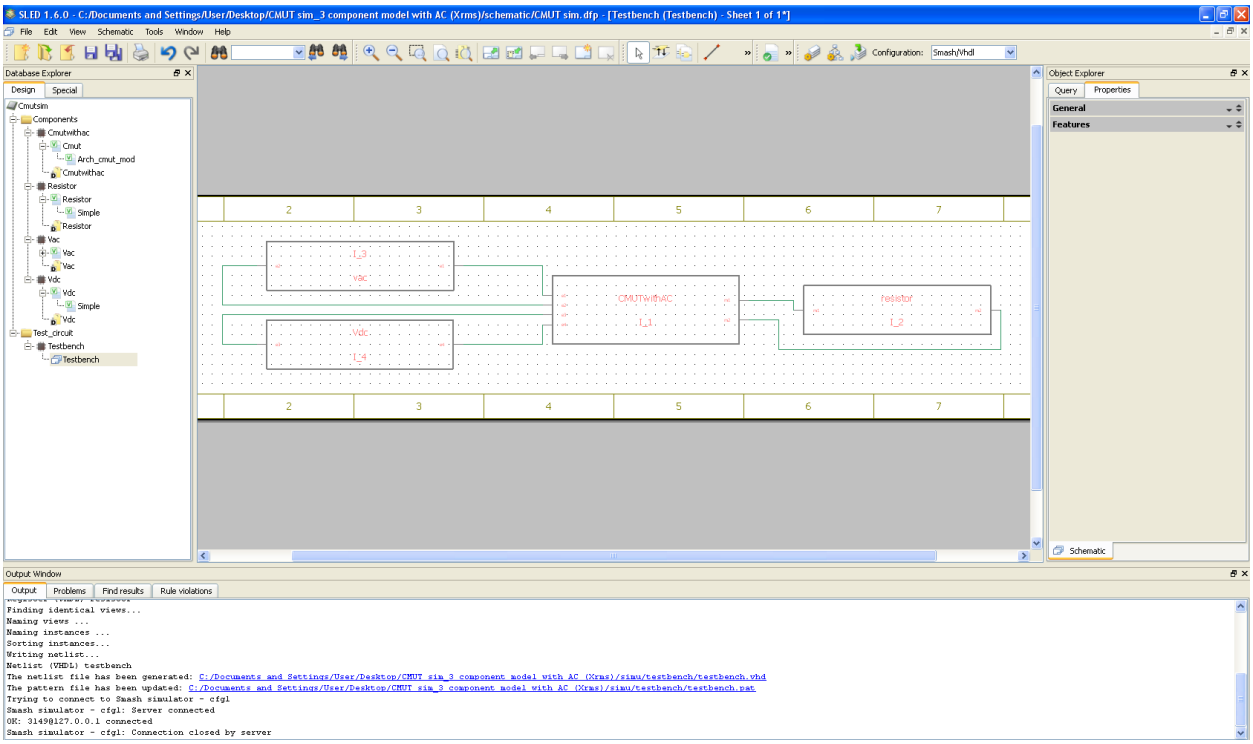

Figure 23. The schematic of ‘testbench’.

The value of the property ‘Amplitude’ in the instance I_3 which is ‘Vac’ was set to ‘amplitude_ac’, and that in the instance I_4 which is ‘Vdc’ was set to ‘amplitude_dc’. The

reason why these properties were parameterized in the instances of the two voltage sources was that it would be easier to change these two voltages in the SMASH simulation.

Clicking ‘Run’ under the ‘Tools’ tab started the netlisting, which automatically opened SMASH 5.14.2. The screenshot of the SMASH window is shown in Figure 24.

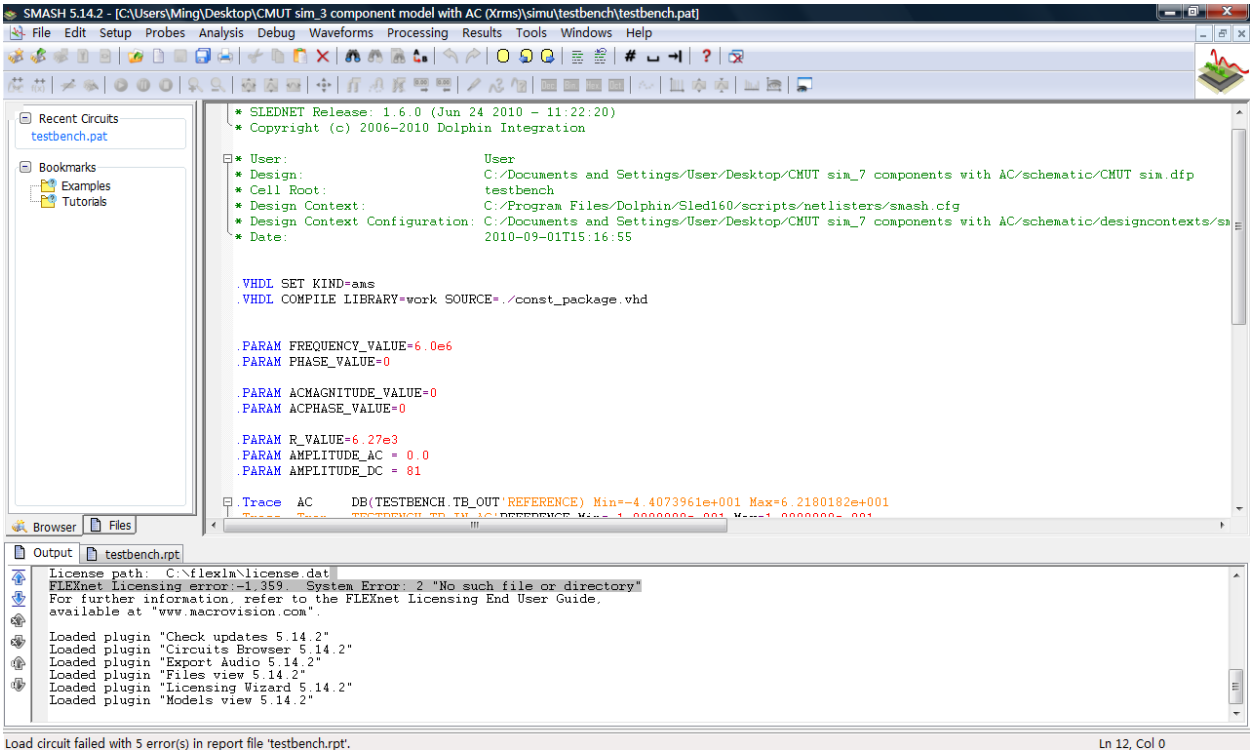

Figure 24. The screenshot of SMASH window.

The detailed simulator control file in testbench.pat is given in Appendices. At the beginning of this control file, the following directives were written:

.VHDL SET KIND=AMS

because it was required to correctly compile VHDL-AMS description when a SPICE netlisting configuration was selected.

4.2 Simulation Results from SMASH

4.2.1 Frequency Response

In order to run a small signal analysis, the following directives needed to be included in the simulator control file:

```
.Trace  AC     DB(TESTBENCH.TB_OUT'REFERENCE)
.AC dec 100000 1MEG 10MEG op=no
.PARAM ACMAGNITUDE_VALUE=1.0
.PARAM ACPHASE_VALUE=0
.PARAM AMPLITUDE_DC = 60
.PARAM R_VALUE=4.928e3
```

TB_OUT is a terminal of nature electrical at the side of the mechanical port, and TB_OUT'REFERENCE is defined in the implementation manual of Dolphine Integration as the voltage between TB_OUT and the electrical reference; .TRACE defines a horizontal window area (this is called an analog "graph") where the evolution of specified analog signals is displayed during the simulation, which is the evolution of TB_OUT in this case; .AC specifies the parameters of a small signal analysis, in this case, the analysis is performed from 1MHz to 10MHz with logarithmic spacings of the analyzed frequencies and 100000 frequency points per decade calculated; and .PARAM is used to define parameters or user-defined functions, in this case the parameters are the amplitude and phase value of the AC small signal, the applied DC bias as well as the load impedance. The parameters can also be set from 'Small signal analysis parameters' in 'Small Signal' under the 'Analysis' tab.

Setting the parameters as above, a small signal analysis was performed to see the frequency response of the CMUT in air transmission as shown in Figure 25, in which we applied a DC bias of 60V that was superimposed on the AC excitation with an amplitude of 10V.

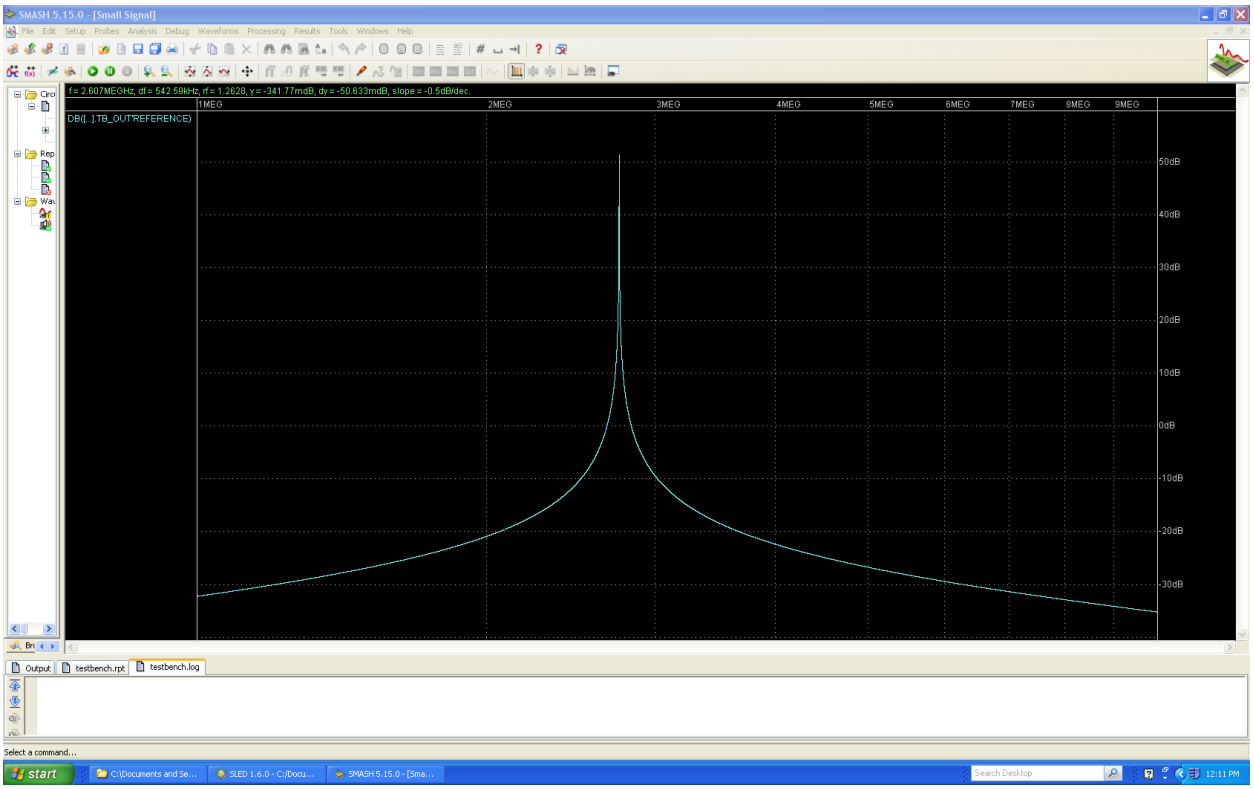

Figure 25. The screenshot of a small signal analysis showing the frequency response in air transimission.

Clicking ‘Dump waveforms in text format’ in ‘Export’ under the ‘Results’ tab, we exported the data of the waveform, re-plotted it in MATLAB 7.0 (The MathWorks, Inc., MA, USA) for clarity as shown in Figure 26. A resonant frequency of 2.7488MHz was obtained, as well as a relatively high Q factor about 23.71.

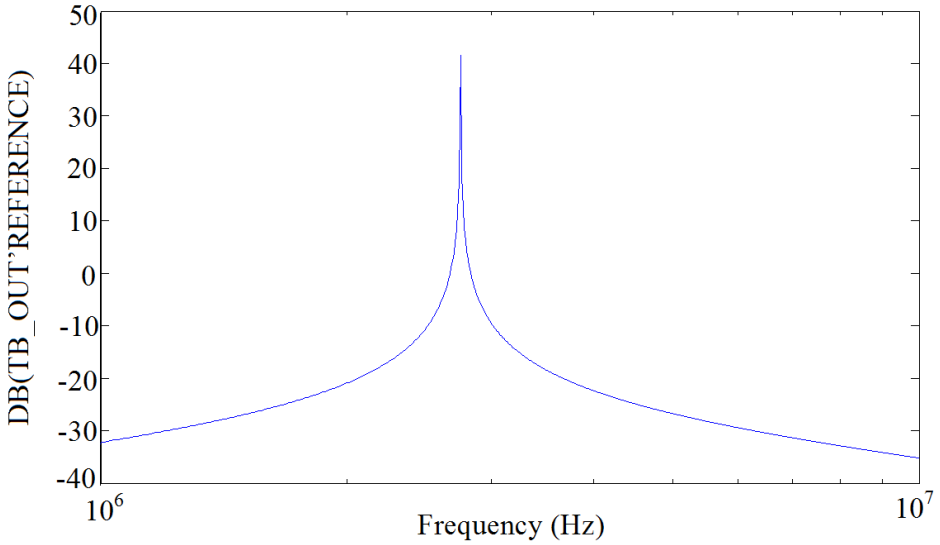

Figure 26. Frequency response in air transmission.

In Figure 26, the y-axis is the ratio of the output voltage, which represents membrane velocity. A frequency response analysis was carried out using COMSOL Multiphysics for comparison. The structure of a CMUT cell used in this simulation and its frequency response in air are given in Figure 27.The resonant frequency is 2.45MHz, which is close to what we obtained from the model simulation.

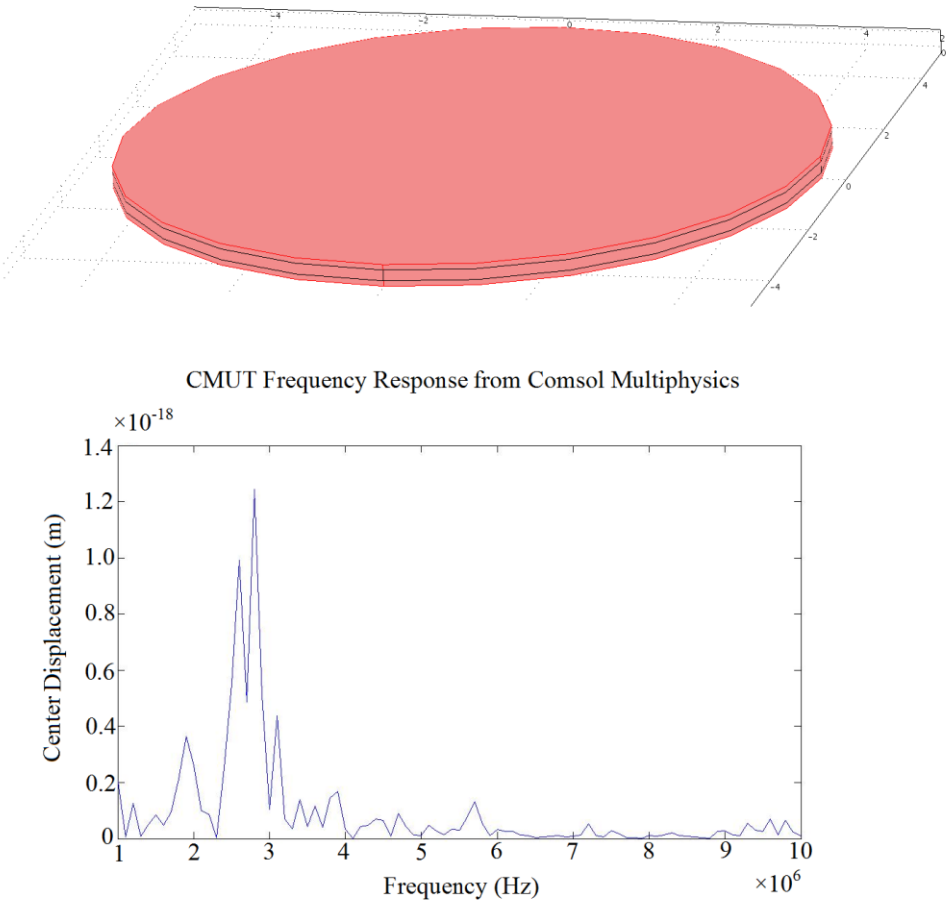

Figure 27. The CMUT structure used in COMSOL Multiphysics (top) and its frequency response in air transmission (bottom).

Another small signal analysis was done in which the frequency range was set from 1MHz to 100MHz to see the frequency response in fatty tissues. Since the load impedance for fatty tissue is $1.527\,\Omega$, we changed the parameter for R_VALUE as below:

.PARAM R_VALUE=1.527

The result is given in Figure 28. A flatter resonant peak compared to that in air transmission could be observed, and the Q factor in fat is about 0.27.

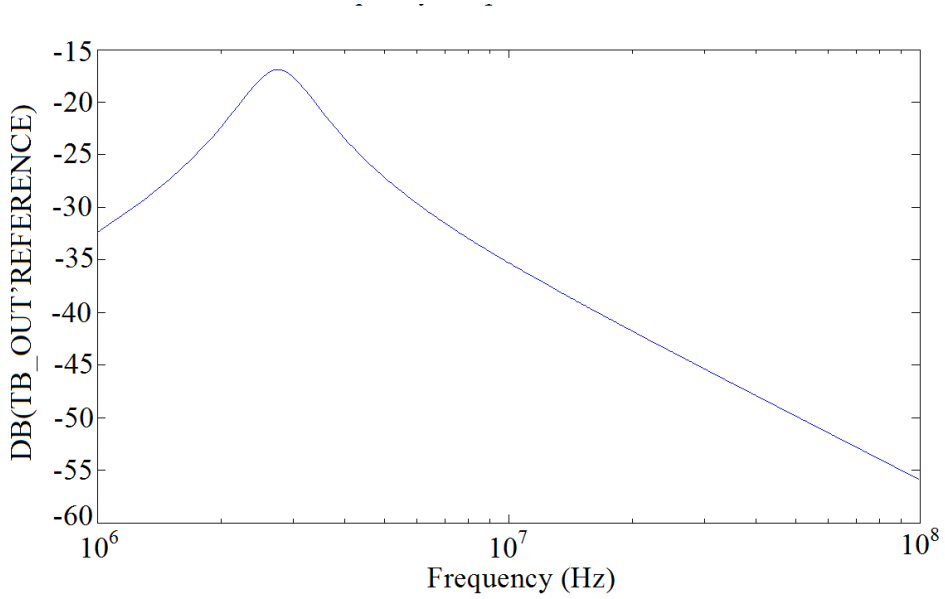

Figure 28. Frequency response in fat transmission.

In ordering to see the electrostatic spring softening effect more clearly, we ran a series of small signal analyses in air transmission. The following directive was added in the simulator control file:

.Step AMPLITUDE_DC 60 80 LIN 2.5

The directive .Step is not a specific analysis specification by itself. It is used to run a series of simulations while varying a parameter, and it works for operating point, DC transfer, transient and small signal analysis. In this case, the parameter AMPLITUDE_DC is linearly swept from 60V to 80V using step 2.5V. A series of small signal analyses were carried out in terms of increasing DC biases, and the 9 resonant frequencies in terms of different DC biases were re-plotted in Figure 29.

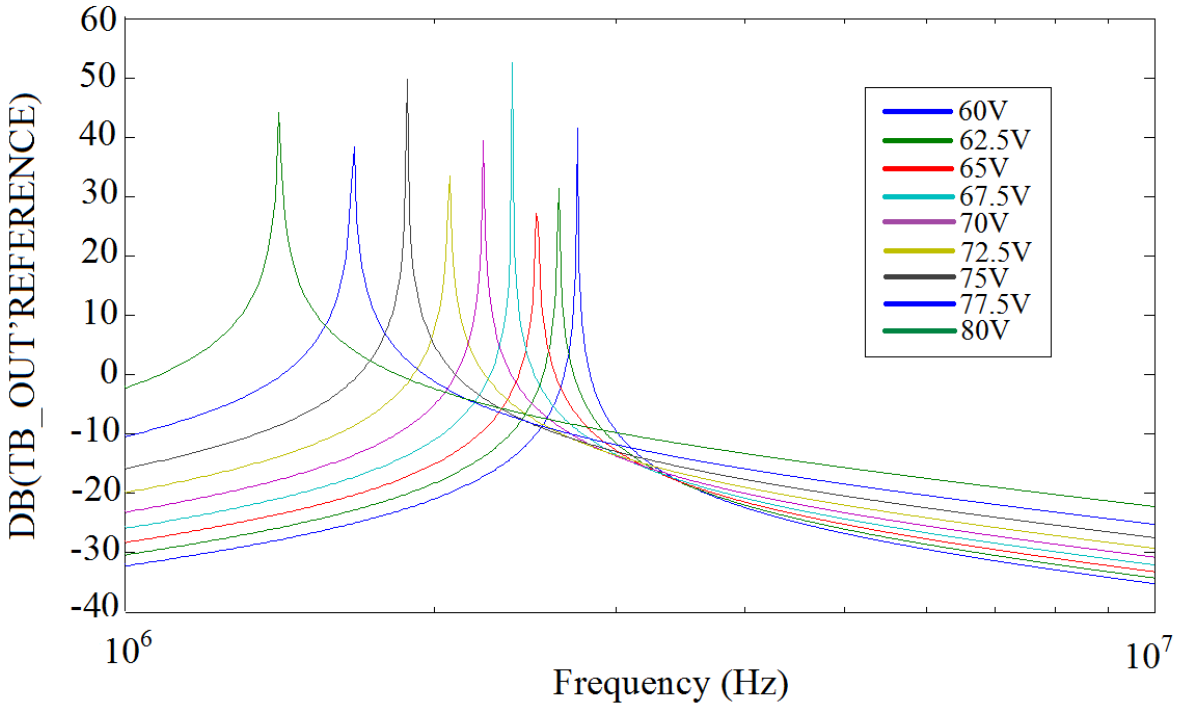

Figure 29. Electrostatic spring softening effect as the applied DC bias increases.

The electrostatic spring softening effect is clearly shown in Figure 38, which is that the resonant frequency dropped closer to 0 as the applied DC bias increased.

4.2.2 Pull-in Voltage

A series of transient analyses were performed to determine the pull-in voltage of the CMUT. We added the following lines in the simulator control file:

.Trace Tran TESTBENCH.TB_IN_DC'REFERENCE

.Trace Tran TESTBENCH.I_1.VOUT__INTEG

.Tran 1ns 1000ns 0s noise=no noisestep=1ns traceBreak=yes compress=no compressCoeff=1 compressTolX=0 compressTolY=1u powerup=no timeup=0s

The directive .Tran specifies the transient analysis main parameters. TESTBENCH.TB_IN_DC'REFERENCE is the DC bias from the DC voltage source, and TESTBENCH.I_1.VOUT__INTEG is the parameter VOUT'INTEG which represents the displacement of the CMUT membrane in the VHDL-AMS file for the CMUT model. In order to add TESTBENCH.I_1.VOUT__INTEG in the simulator control file, we needed to click the 'Circuit' tab and then all the electrical components in the 'Testbench' circuit were listed. We then clicked 'I.1-CMUT' and the parameter TESTBENCH.I_1.VOUT__INTEG showed up. Right-clicking TESTBENCH.I_1.VOUT__INTEG, we could add this parameter in the .Trace directive by choosing 'Trace in transient'. This process is shown in Figure 30.

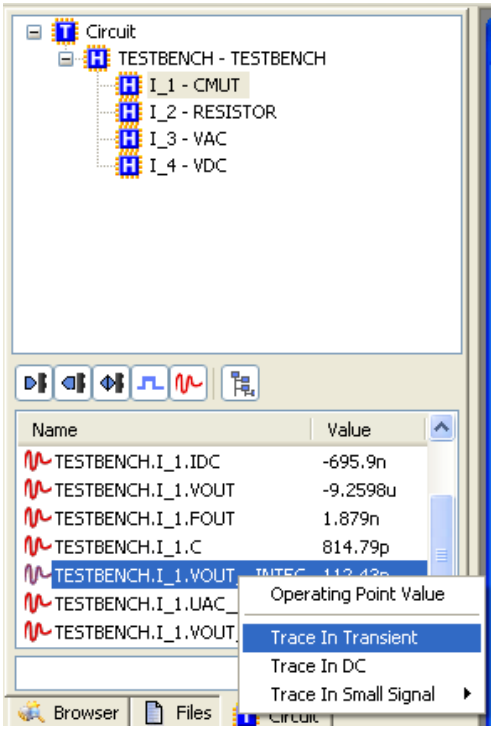

Figure 30. Adding VOUT'INTEG into the .Trace directive in the simulator control file.

From the 'Sweep analysis parameters', we chose 'AMPLITUDE_DC' as the parameter and set the range for AMPLITUDE_DC from 0V to 100V with a step of 10V. From a series of transient

analyses, we could observe that when the value of AMPLITUDE_DC became 90V, the simulation stopped without reaching converge, which means the pull-in voltage lies between 80V and 90V. We then set the range for AMPLITUDE_DC from 80V to 90V with a step of 1V and ran another series of transient analyses and observed that when the value of AMPLITUDE_DC turned 82V, the simulation stopped, meaning the CMUT membrane collapsed and a convergence could not be reached. Therefore, we came to a conclusion that the pull-in voltage of the CMUT membrane is 81V. The results of these analyses are shown in Figure 31.

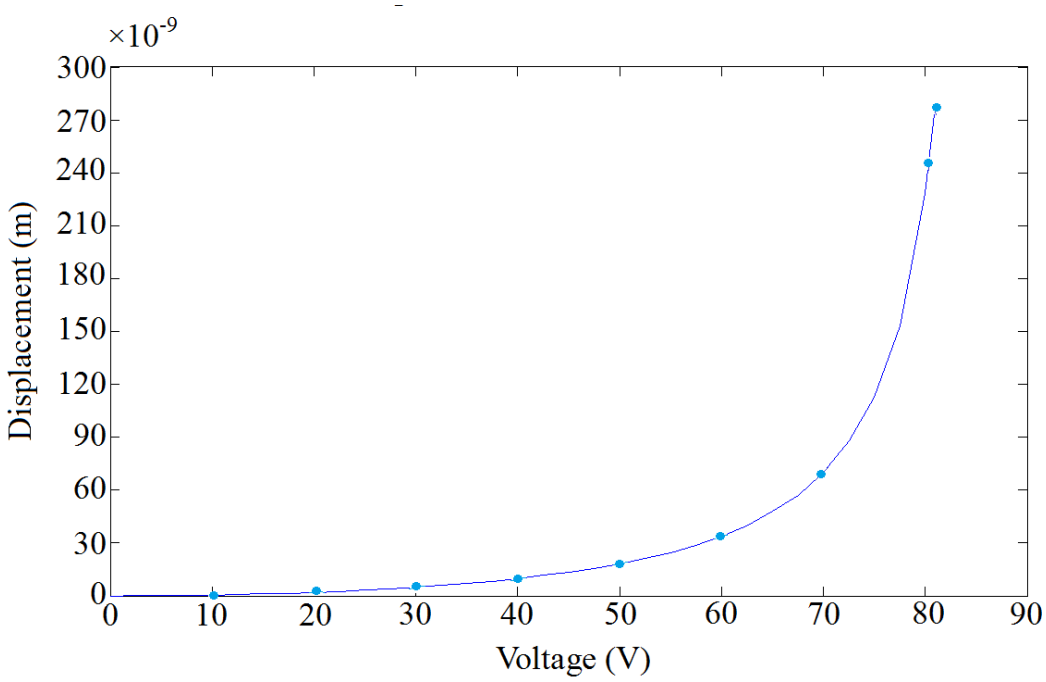

Figure 31. CMUT membrane displacement at the center as the applied DC bias voltage increases using the behavioral model.

The pull-in voltage of the CMUT membrane is 81V and the displacement is 296nm, which has a 12% error compared to the result from the static and parametric analyses using COMSOL Multiphysics rendering a pull-in voltage at 91V and a displacement of 248nm. The error of the

pull-in voltage between the results from the piston-like CMUT behavioral model developed in [1] with the same parameters and COMSOL Multiphysics is 16%.

4.2.3 Electro-mechanical Conversion Efficiency

The effect of the DC bias on the electro-mechanical conversion efficiency (output mechanical power over input electrical power) of the CMUT was also simulated. A 10V, 2.75MHz sinusoid was superimposed on a DC bias which is swept from 0 to the point where the operating point is no longer reached, and the medium was considered to be fat. The electro-mechanical conversion efficiency is shown in Figure 32. This figure shows that as the applied DC bias increases, the electro-mechanical conversion efficiency also increases. It is usually very low, but when the sum of the applied DC bias and the amplitude of the sinusoid is close to the pull-in voltage, a relatively large conversion efficiency is observed.

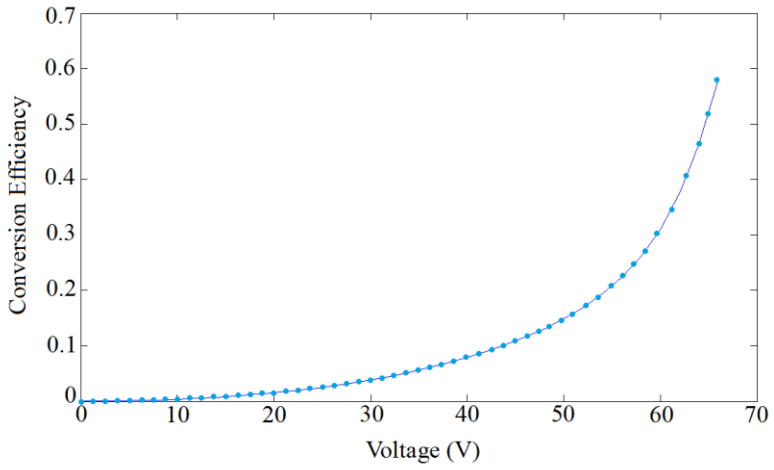

Figure 32. Electro-mechanical conversion efficiency versus Applied DC bias voltage.

4.2.4 Optimization of the DC/AC Voltage Ratio

Since the CMUT model has 2 electrical ports, one is connected to the DC bias the other connected to the AC excitation, we needed to know how much DC bias and AC excitation we should apply in order to achieve the maximum transmitted acoustic power. In this simulation, the sum of the DC bias and the amplitude of the AC excitation was set to 95% of the pull-in voltage (in order not to enter the pull-in instability region), as given by (71):

$$V_{DC} + \hat{V}_{AC} = 0.95V_{pi} = 0.95 \times 81V \approx 77V . \tag{71}$$

The resonant frequency we obtained earlier in this chapter is 2.7488MHz, so we need a pulse with a spectrum where the main lobe bandwidth is larger than the resonant frequency, in order to avoid attenuation. A square pulse in the time domain was chosen, as given by (72):

$$x(t) = \begin{cases} m, |t| < T_1 \\ 0, |t| > T_1 \end{cases} . \tag{72}$$

Its Fourier transform is given by (73):

$$X(j\omega) = m\int_{-T_1}^{T_1} e^{-j\omega t} dt = 2m\frac{\sin \omega T_1}{\omega}, \tag{73}$$

and its main lobe is $\frac{\pi}{T_1}$. In this case, we wanted the main lobe to be larger than 6MHz, namely

$$\frac{\pi}{T_1} \geq 6MHz \cdot 2\pi . \tag{74}$$

Therefore, $T_1 \leq 83.3ns$. Here we chose $T_1 = 5ns$, that is to say, the DC bias and the AC excitation are both square pulses with $T_1 = 5ns$, and the sum of their heights is 77V, which equals to 95%

of the pull-in voltage. A series of transient analyses were run with the DC bias increasing from 0V to 77V with a step of 1V and the amplitude of the AC excitation decreasing from 77V to 0V with a step of 1V to see if we could observe a maximum acoustic power traced by multiplying TESTBENCH.I_1.VOUT (the output voltage at the side of the mechanical port) by TESTBENCH.I_1.FOUT (the output current at the side of the mechanical port). We can see from Figure 33 that when the amplitude of the AC excitation is about 10V and the one of the DC bias is about 67V, the acoustic power reaches its maximum, which is around 0.037W (which is the acoustic power of all the 5041 cells on one die).

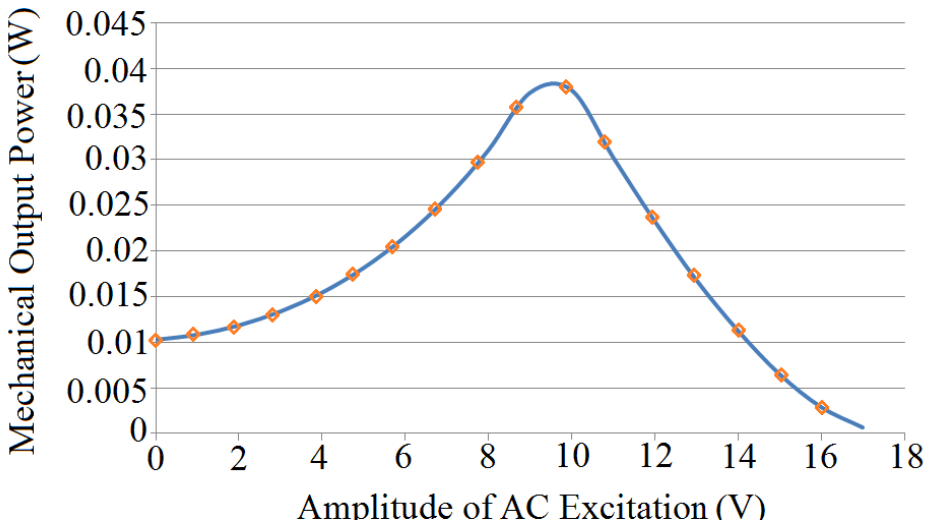

Figure 33. Mechanical output power versus the amplitude of AC excitation.

4.2.5 Analysis of the Accuracy of Plate Approximation

In the VHDL-AMS model of the CMUT, we used the vibrating plate theories given by equations (26) and (65) to approximate the actual displacement of the CMUT membrane. In order to validate the approximation, a series of static and parametric analyses were performed in

COMSOL Multiphysics in which the DC bias was increased from 0V to the pull-in voltage, with the step of 10V, and the data of the displacement of the CMUT membrane at each step were obtained. Since the data were discrete, we calculated the CMUT membrane capacitance using the displacement data for each voltage step in MATLAB and then obtained the average value of the capacitance. Then we compared the results with the ones calculated from the equations (26) and (65) used in the CMUT behavioral model - the comparison is shown in Figure 34.

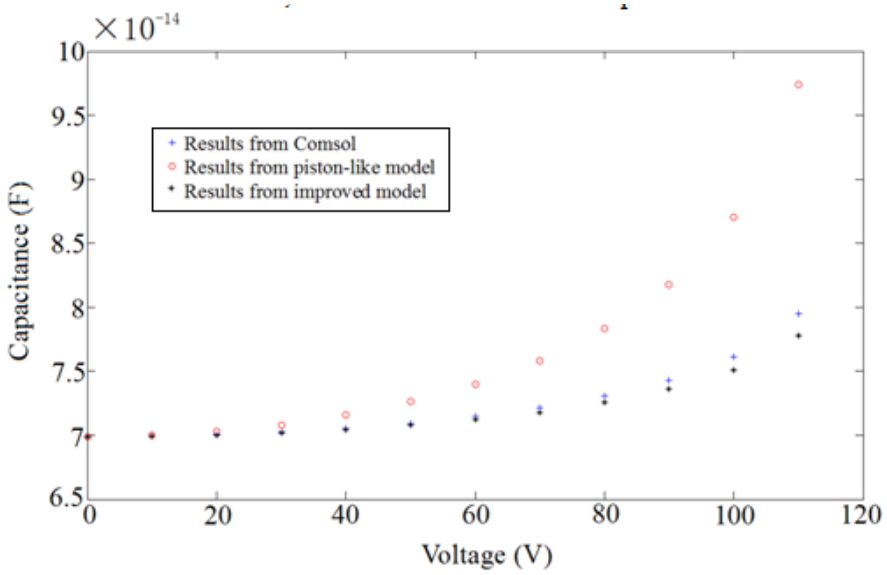

Figure 34. Comparison of the CMUT membrane capacitance among results from COMSOL Multiphysics, the piston-like model and the improved model in this work.

In the simulation using COMSOL Multiphysics, the radius of the CMUT membrane and that of the bottom electrode were both set to 47μm, same as the membrane radius in the behavioral model of CMUT. And the pull-in voltage of this structure is 113V. From Figure 43, we can see that the equations (17) and (24) used in the model approximate the actual average capacitance of the CMUT plate very well when the DC bias is low; as the DC bias increases, the calculated

average capacitance using the equations diverges more and more from the one obtained from COMSOL Multiphysics; when the DC bias reaches the pull-in voltage, there is a 2.5% difference between the average capacitance obtained from COMSOL Multiphysics and that using the equations (17) and (24), whereas the error between the results from COMSOL Multiphysics and the piston-like model developed in [1] is 24%. In the behavioral model developed in this work the AC displacement is a more accurate approximation than the DC displacement, as explained earlier, and the AC displacement is much smaller than the DC displacement under high DC biases than under lower DC biases. Hence, under lower DC biases the more accurate AC displacement approximation weighs more than the DC displacement approximation whereas under higher DC biases it weighs less than DC displacement approximation, thus the results from the behavioral model in this work agree with those from COMSOL simulation very well under lower DC biases, while under higher DC biases the results from the behavioral model in this work deviate from those from COMSOL simulation more. This could serve as an explanation of the 2.5% difference we observed when the DC bias is high.

Chapter 5

Experimental Characterization of CMUTs

5.1 Packaged Die and Testing Equipment

9 packaged die of CMUTs were received. One die and its package as well as the microscopic view of the die showing the top left corner are shown in Figure 35.

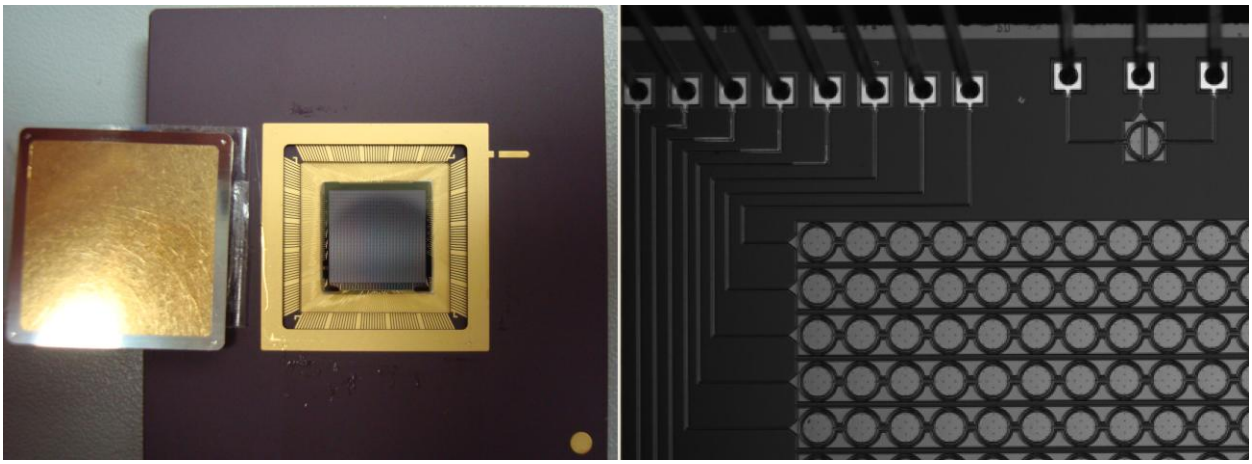

Figure 35. One die and its package 208PGA (left) as well as the microscopic view of the die (right).

Polytec Micro System Analyzer (MSA-500) (Polytec Inc., CA, USA) was used in the experimental characterization of the CMUTs. In general, electrical testing can prove if a device is working or not. However, MEMS devices usually involve active moving elements for sensing and actuation, thus, electrical testing alone cannot determine their exact behavior. Using laser

Doppler vibrometry, Polytec MSA-500 provides fast, real-time 3D analysis of structural vibration and surface topography. The system of Polytec MSA-500 is shown in Figure 36.

Figure 36. The system of Polytec MSA-500, left (from the top down): Data Management System, Junction Box, Vibrometer Controller; right: Fiber-Optic Interferometer, Measurement Head.

There are two sets of software, PMA and PSV, which are for in-plane and out-of-plane motion respectively. In our case, PSV 8.6 was used in that the CMUT membrane exhibits out-of-plane deflection and vibration when actuated.

5.2 Results from Experimental Characterization

5.2.1 Pull-in Characterization

According to the simulation results from COMSOL Multiphysics, the pull-in voltage of CMUT cells in our design is 91V. However, the maximum amplitude of the output voltage Polytec

MSA-500 can provide is 10V, so we needed to connect the output channel of Polytec MSA-500 to a high-voltage amplifier in order to determine the pull-in voltage. The sinusoidal signal was offset from 10V up with a step of 10V. And the amplitude and frequency of the sinusoidal signal were set to 2.5V and 300kHz. Since MSA-500 does not allow applying only a DC bias, we settled for a sinusoid signal with a large offset and a small amplitude to approximate a DC bias. Then a scanning measurement was performed for each step and the AC displacement could be observed respectively. Generally, as the offset increases the AC displacement should increase accordingly, and when the offset reaches the pull-in voltage of the CMUT cells, the AC displacement will stop increasing or show an unexpected value. Tests on multiple arrays of CMUTs on different die all rendered a pull-in voltage between 90V and 100V, which is an excellent agreement with the simulation results from COMSOL Multiphysics. The AC displacement versus the increasing offset of the sinusoidal signal is given in Figure 37.

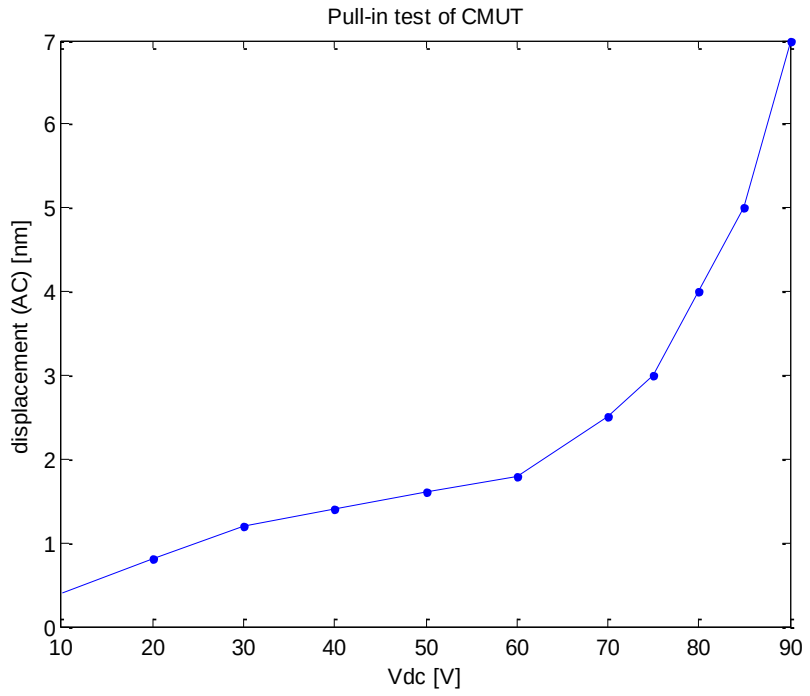

Figure 37. The AC displacement versus the increasing offset of sinusoidal signals.

During the tests on different arrays of CMUTs on different die, the AC displacement dropped down below 1nm after the offset increased to 100V, and it remained so even when the offset was reduced afterward. A possible explanation of such phenomenon is that the CMUT membrane adheres to the bottom electrode as soon as it collapses and cannot rebound due to the viscous residue that might exist in the gap between the bottom electrode and the CMUT membrane after hydrofluoric release.

If we offset the sinusoidal signal to 0V but increased the amplitude from 10V up with a step of 10V, we could observe that some of the CMUT cells were burnt when the amplitude was much lower (around 50V and 60V) than the pull-in voltage. This could be due to a much larger AC current that was caused by a large membrane velocity. In a first approximation, we can consider the CMUT capacitance as given by an equivalent parallel capacitor:

$$C = \frac{\varepsilon A}{d_0 - x}. \tag{75}$$

Then, the total electric quantity can be given by (76):

$$Q = C \cdot u_{AC}. \tag{76}$$

Thus, the temporary AC current is given by (77):

$$
\begin{aligned}
i &= \frac{dQ}{dt} = \frac{d}{dt}\left(C \cdot u_{AC}\right) \\
&= u_{AC}\frac{dC}{dt} + C\frac{du_{AC}}{dt} \\
&= u_{AC}\frac{d}{dt}\left(\frac{\varepsilon A}{d_0 - x}\right) + \frac{\varepsilon A}{d_0 - x}\frac{du_{AC}}{dt} \\
&= u_{AC}\frac{\varepsilon A}{\left(d_0 - x\right)^2}v + \frac{\varepsilon A}{d_0 - x}\frac{du_{AC}}{dt}
\end{aligned}, \tag{77}
$$

When the transient velocity of the CMUT membrane *v* is large, a large AC temporary current can be generated, that burns the CMUT structure. Figure 38 shows a burnt CMUT cell.

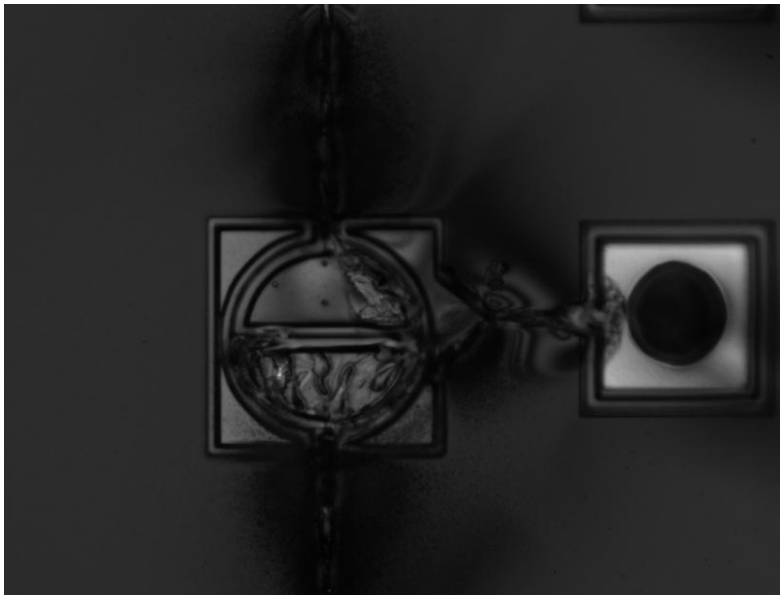

Figure 38. A burnt CMUT cell.

In some cases where the offset was as high as 100V and the amplitude of the sinusoidal signal was low, we could still observe that the CMUT structure was burnt. This might be due to a large DC current caused by the short circuit after the membrane collapsed.

5.2.2 Simple Harmonic Excitation Characterization

In order to see the vibration shapes of individual CMUT cells, few simple harmonic analyses were carried out using a sinusoidal signal with a frequency of 300 kHz and an amplitude of 10V. Figure 39 shows the surface velocity profile of two neighboring CMUT cells under a symmetric sine wave actuation.

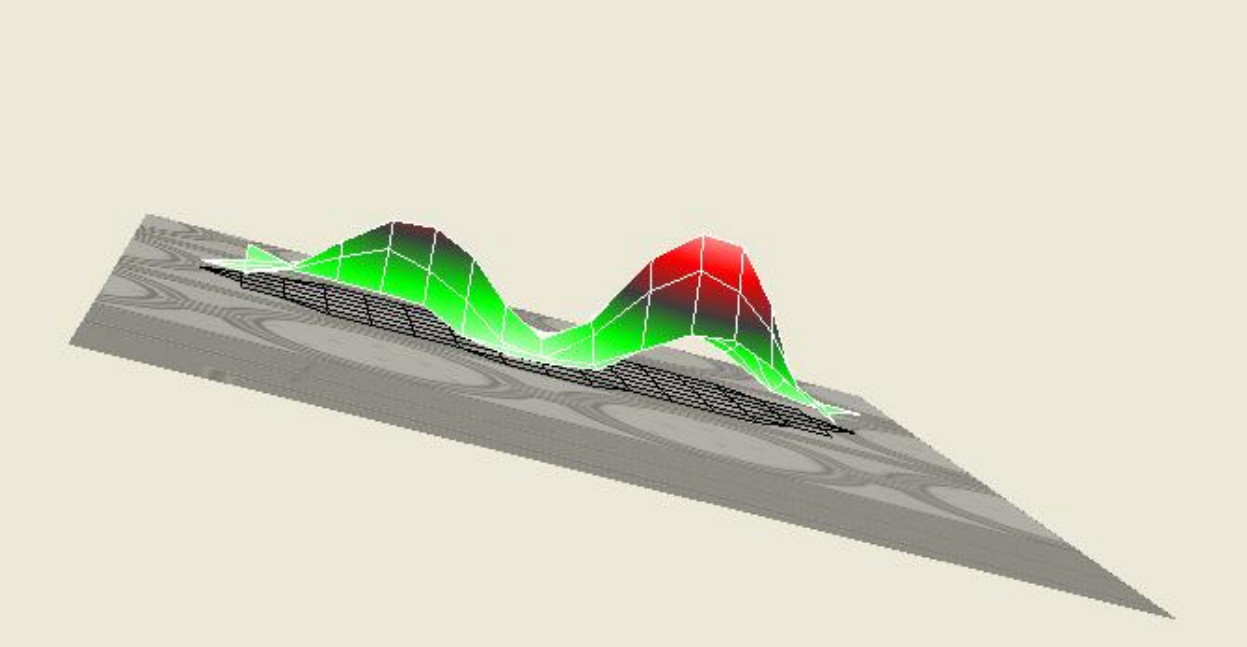

Figure 39. The surface velocity profile of two neighboring CMUT cells under a symmetric sine wave actuation.

The surface velocity profile in Figure 39 shows the vibration shapes of the two neighboring CMUT cells. The difference between the maximum velocities of the two neighboring cells could be due to the different amounts of residue trapped in the gap between the membrane and the electrode after hydrofluoric release or the non-uniform distribution of initial tension in the membrane. It was observed at 600 kHz because the electrostatic force f_e is proportional to

$\left(u_{DC}+u_{AC}\right)^2$:

$$f_e \sim \left(u_{DC}+u_{AC}\right)^2, \tag{78}$$

In this case, u_{DC}=0, so

$$f_e \sim \left(u_{DC}+u_{AC}\right)^2 = u_{AC}^2 = \hat{u}_{AC}^2 \cos^2\left(\omega t+\phi\right) = \hat{u}_{AC}^2 \frac{\left(\cos\left(2\omega t+\phi\right)+1\right)}{2} \sim \cos\left(2\omega t+\phi\right). \tag{79}$$

Hence, the CMUT cells were actuated by an electrostatic force with a frequency of 600 kHz.

Applying the same sine wave on only one of the electrodes (for the multiple electrodes CMUT structures) will actuate the CMUT cell asymmetrically. Figure 40 shows the surface velocity profile of an asymmetrically actuated CMUT cell. Results can also be found in [20].

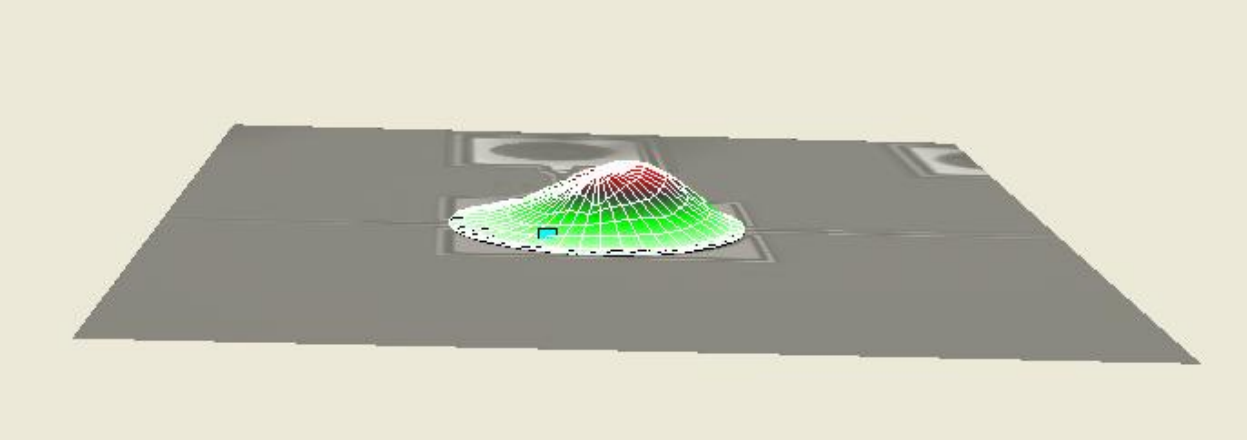

Figure 40. The velocity profile of a CMUT cell under an asymmetric sine wave actuation.

5.2.3 Frequency Response Characterization

By choosing the 'Periodic Chirp' in the Generator settings, the resonant frequencies and different vibration mode shapes of a CMUT cell could be observed. In our case, we set the amplitude of

the periodic chirp to 10V, and the frequency range from 1000Hz to 10MHz. The scanning measurement was performed on a CMUT cell with 2 bottom electrodes in order to observe its frequency response under both symmetric (equal voltage is applied on both electrodes) and asymmetric actuation (voltage is only applied on one electrode). In symmetric actuation, we connected both electrodes to the output of the auxiliary decoder and the CMUT membrane to ground. The frequency response of one CMUT cell under symmetric actuation is shown in Figure 41.

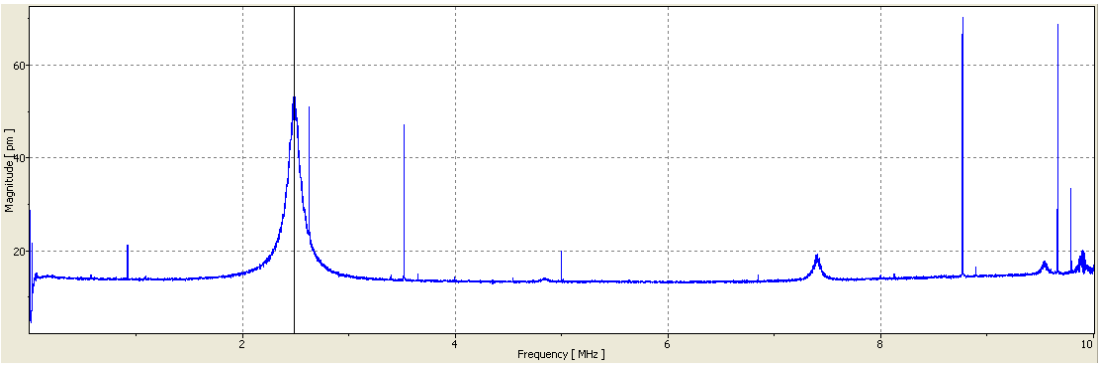

Figure 41. Frequency response of one CMUT cell from 1000kHz to 10MHz under symmetric actuation.

A few spurious peaks could be seen in the frequency response and this might be due to the relatively high noise voltage caused by the broad bandwidth of the DD-300 Displacement Decoder. The first measured resonant frequency is 2.4828MHz, compared to the one from COMSOL Multiphysics which is 2.15MHz. Dragging the cursor from 1000kHz to the first resonant frequency, we could see the vibration shape of the tested CMUT cell changed from irregular and rugged to uniform and bump-like. This is when $m=n=0$ in the theories of vibrations of shells and plates [16].

The second mode shape (m=0, n=1) cannot be seen under the symmetric actuation because when m=0, n=1, the second natural mode is given by (80):

$$U_{01}(r,\theta)=\left[J_1\left((\lambda a)_{01}\frac{r}{a}\right)-\frac{J_1\left((\lambda a)_{01}\right)}{I_1\left((\lambda a)_{01}\right)}I_1\left((\lambda a)_{01}\frac{r}{a}\right)\right]\cos(\theta-\varphi). \tag{80}$$

Thus,

$$\begin{aligned}F_{AC}^{*}&=\frac{1}{\rho_m d_m N_{AC}}\int_r\int_\theta\left(q_{AC}^{*}U_1\right)rdrd\theta\\&=\frac{1}{\rho_m d_m N_{AC}}\int_0^a\int_0^{2\pi}\left(q_{AC}^{*}\left[J_1\left((\lambda a)_{01}\frac{r}{a}\right)-\frac{J_1\left((\lambda a)_{01}\right)}{I_1\left((\lambda a)_{01}\right)}I_1\left((\lambda a)_{01}\frac{r}{a}\right)\right]\cos(\theta-\varphi)\right)rdrd\theta.\\&=0\end{aligned} \tag{81}$$

From the above derivations, we can see that under symmetric actuation when the number of diametral lines n is an odd number, the modal participation factor is 0. Therefore, the second vibration mode shape under symmetric actuation cannot be observed.

However, the resonant frequency for the third vibration mode (m=0, n=2) is very clear and can be seen at 7.3984MHz, compared to the one from COMSOL Multiphysics which is 7.415MHz. The third mode shape under symmetric actuation with comparison to the third eigen mode from eigenfrequency analysis using COMSOL Multiphysic shown in Figure 42, which clearly shows two diametral lines in the vibrational shape of the CMUT cell.

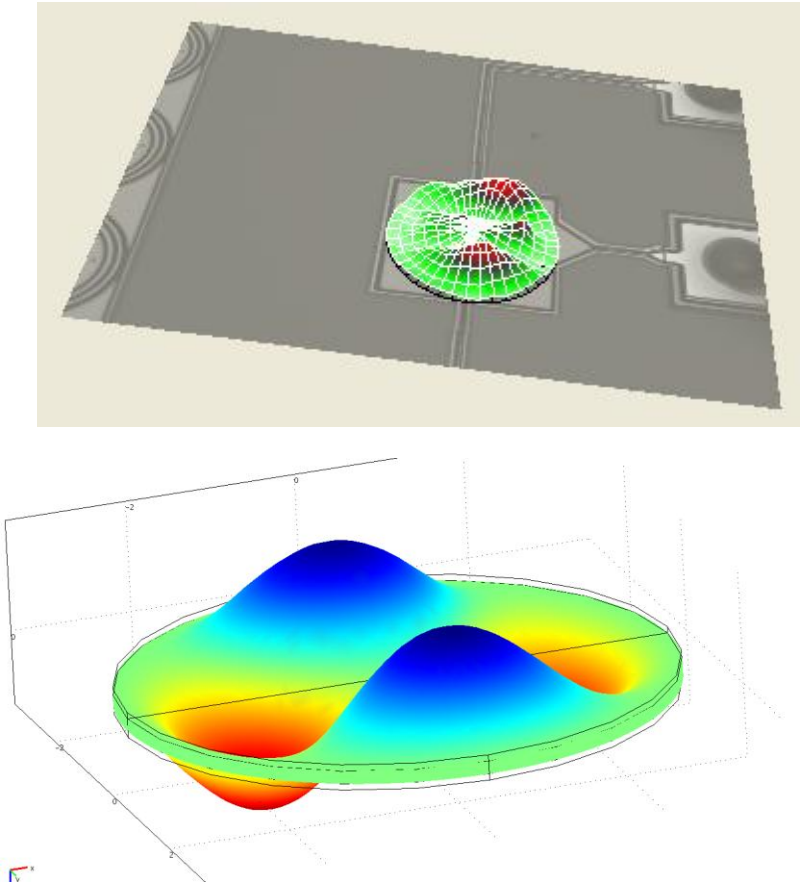

Figure 42. The third mode shape (top) under symmetric actuation compared to the third eigen mode from eigenfrequency analysis using COMSOL Multiphysics (bottom).

The measured resonant modes show the amplitude of the surface velocity profile and phase is not considered, thus all the variations are shown in the positive direction. From the frequency response in Figure 41, other 2 resonant frequencies between 9MHz and 10MHz could be seen, but the 2 resonant modes could not be clearly observed due to the high noise levels.

Under asymmetric actuation, we connected one electrode to the output of the auxiliary decoder, and the other one as well as the CMUT membrane to ground. The first resonant frequency is

basically the same as in symmetric actuation, while the second resonant frequency is clearly seen, as in Figure 43.

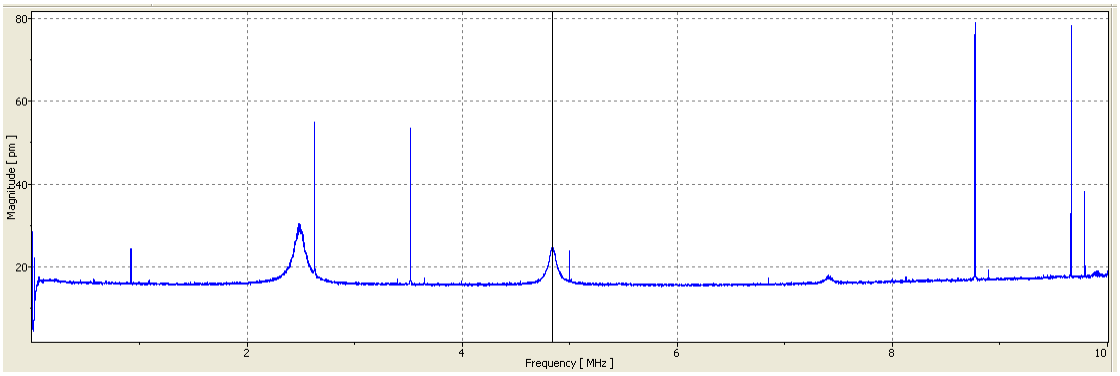

Figure 43. Frequency response under asymmetric actuation.

The second mode shape compared to the second eigen mode from eigenfrequency analysis using COMSOL Multiphysics is shown in Figure 44.

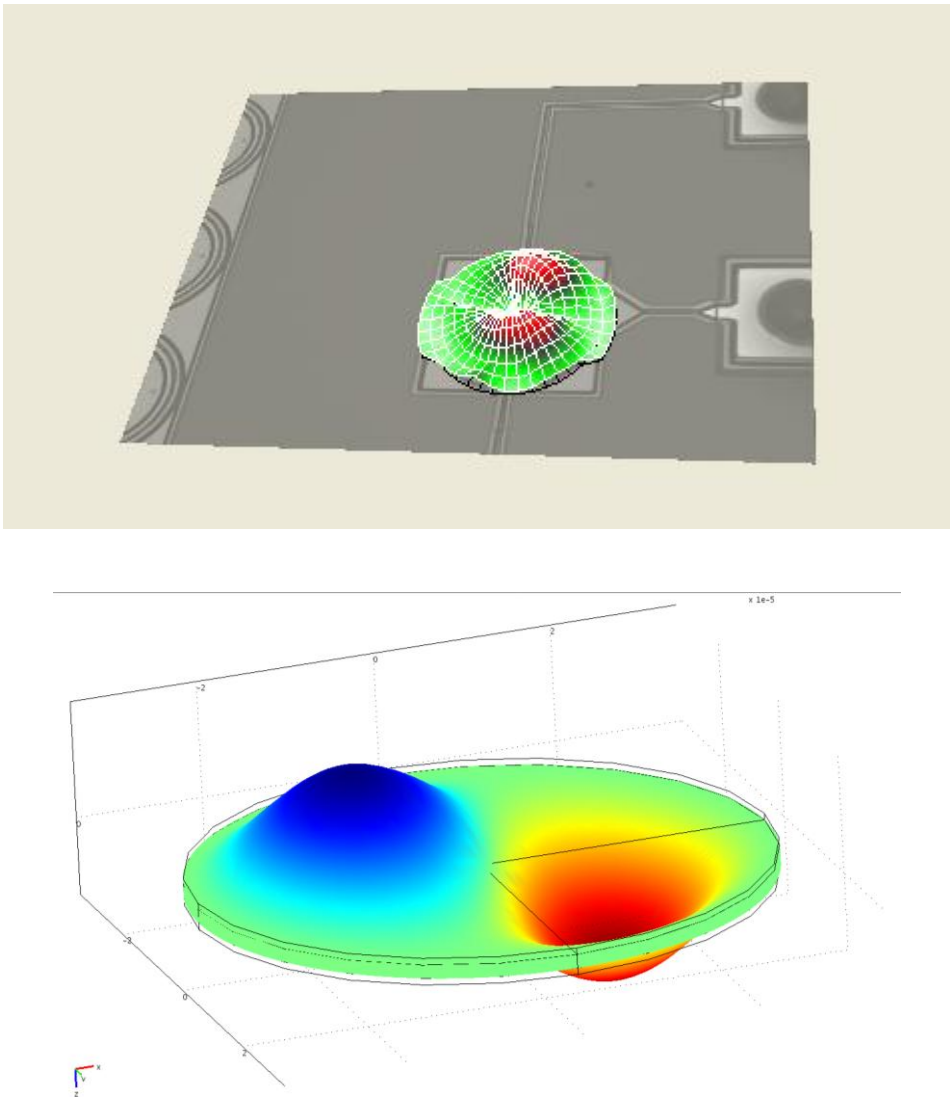

Figure 44. The third mode shape (top) compared to the third eigen mode from eigenfrequency analysis using COMSOL Multiphysics (bottom).

From Figure 44, we could observe one diametral line in the third mode shape. Under asymmetric actuation, there is also one cosine component in q_{AC}^{*}, which makes the results of the integral (79) non-zero:

$$F_{AC}^{*}=\frac{1}{\rho_m d_m N_{AC}}\int_r\int_\theta\left(q_{AC}^{*}U_{01}\right)rdrd\theta\,. \tag{79}$$

The resonant frequency for the third mode is also the same as in the symmetric actuation, the mode shape is nonetheless more clear, as shown in Figure 45, where we could observe 2 diametral lines.

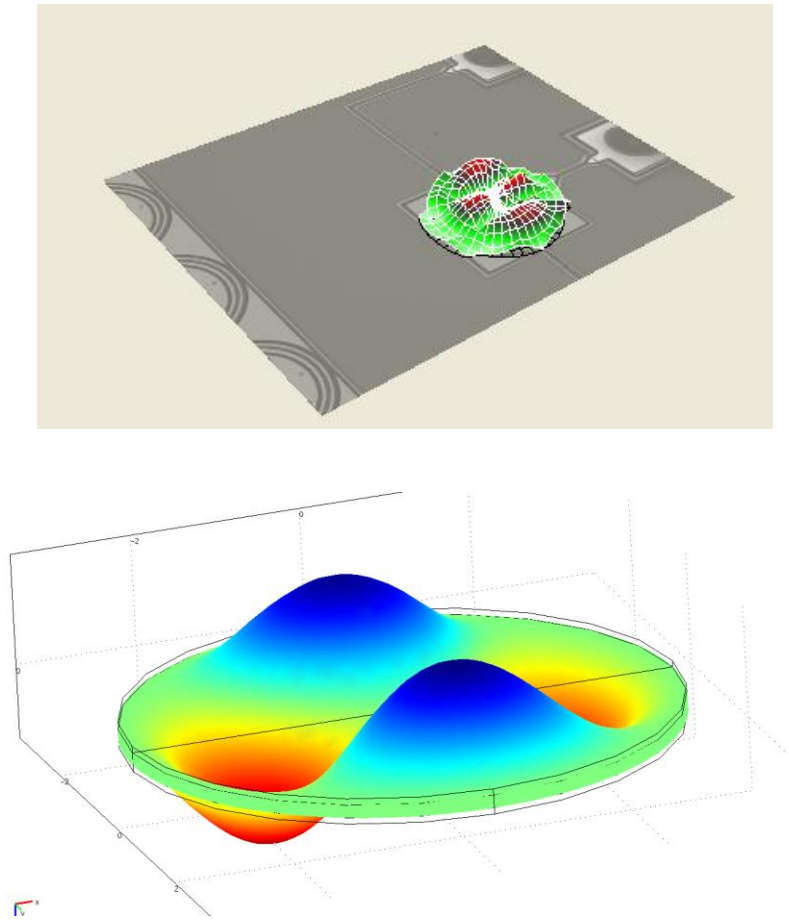

Figure 45. The third mode shape (top) under asymmetric actuation compared to the third eigen mode from eigenfrequency analysis using COMSOL Multiphysics (bottom).

The magnitude of the frequency response under asymmetric actuation is generally smaller than under symmetric actuation - the electrostatic force is much smaller in asymmetric actuation due to the fact that the driving voltage is only applied on only one of the electrodes.

The electrostatic spring softening effect with the chosen driving signal was also observed. We fixed the amplitude of the periodic chirp at 2.5V, and changed the offset from 10V to 60V. The first resonant frequency of one CMUT cell versus the offset is given in Table 10. Table 10 shows that the first resonant frequency drops as the offset increases.

Table 10. The first resonant frequency of one CMUT cell versus the offset.

Offset (V)	The first resonant frequency (MHz)
10	2.565625
20	2.565625
30	2.564063
40	2.551563
50	2.528125
60	2.503125

Chapter 6

Conclusion and Future Work

The Capacitive Micromachined Ultrasonic Transducer (CMUT) has drawn major attention from various research groups around the world and has become a research hot spot in ultrasonic transducer technology since the 1990s. Many of its advantages over the traditional piezoelectric transducers were demonstrated by numerous experimental results. Meanwhile, the behavioral modeling of CMUT has evolved from simplified analytical conisderations to more detailed Spice equivalent models.

This work reported a design of CMUTs which includes CMUT cells with one, two and four bottom electrodes, where the cells with two bottom electrodes are used to analyze the effect of asymmetric electrical actuation. The parameters in this design were determined from the results of COMSOL Multiphysics simulations in order to achieve a relatively high resonant frequency and a low pull-in voltage.

A more accurate behavioral model of CMUT written in VHDL-AMS was also developed. Unlike the earlier developed VHDL-AMS CMUT behavioral model where the vibration of the CMUT membrane was treated as a moving piston, in this new model we divided the CMUT membrane displacement into DC and AC displacement components and treated them independently. We considered the first natural mode of the plate vibration as the AC excitation component, derived the modal participation factor for the first natural mode and obtained a two-port behavioral model of CMUT. We wrote the model in VHDL-AMS language, implemented and simulated it

in SLED and SMASH from DOLPHIN Integration. Various simulations were performed including the frequency responses, pull-in voltage, electrostatic spring softening effect, the electro-mechanical conversion efficiency, the optimization of DC/AC voltage ratio to achieve the maximum acoustic power, etc. The results were in good agreement with those obtained from the FEM model simulated in COMSOL Multiphysics.

Polytec Micro System Analyzer (Polytec MSA-500) using Laser Doppler Vibrometry was used in the experimental characterization of CMUTs fabricated with the PolyMUMPs technique. The pull-in voltage was in an excellent agreement with the results from COMSOL Multiphysics. Multiple vibration modes were observed, and their respective resonant frequencies were also obtained and showed good matching with the ones obtained by the behavioral model and by COMSOL Multiphysics simulations. A journal publication is now being prepared including all the work on the behavioral modeling, analytical model simulation and experimental characterization.

One direction of the future work is to incorporate even more accurate approximation of the motion of the CMUT membrane by considering more natural vibration modes using the mode decomposition method and add the effect of the membrane interaction with the gas kept in the gap between the CMUT membrane and the bottom electrode. Applications of CMUTs under asymmetric actuation are still being studied.

Since there are release holes on the CMUT membrane in this design in order to form the gap between the membrane and the electrode, the CMUT cells can only be used in air. Most applications require that the CMUT cells can be used in liquids, thus the immersion-type CMUTs are another important direction of the future work. The CMUT cells fabricated in this

work can be used as the immersion-type if the release holes are totally covered whereas the gap still exists.

Several methods of covering the release holes will be studied. One is to use inkjet printing techniques used for the deposition of various polymer from the liquid form. The drawback of this method is that the diameter of one droplet is small, so multiple droplets are needed in order to cover all the release holes on one cell. Also, due to the large number of CMUT cells on each die (over 5000), covering the holes on all the cells one by one would be extremely time-consuming. Another method is to chemical vapor deposit a parylene-C layer on the die [19]. Parylene-C is an excellent moisture barrier and the most bio-accepted coating for devices permanently implanted into human bodies. A potential drawback of this method is that the conformal coating of parylene-C might not only cover the release holes on the membrane, but also fill up the gap between the membrane and the electrode to a certain extent, and might thus lead to inefficiency or even failure in the function of the devices. Relevant experiments will be carried out so as to see the feasibility of this method.

References

[1] S. Frew, H. Najar, and E. Cretu, "VHDL-AMS Behavioural Modelling of a CMUT Element," in *Behavioral Modeling and Simulation Workshop, 2009. BMAS 2009. IEEE*, pp. 19-24 .

[2] I. Ladabaum, X. Jin, H. T. Soh, and B. T. Khuri-Yakub, "Surface Micromachined Capacitive Ultrasonic Transducers," *IEEE Trans. Ultrason., Ferroelect., Freq. Contr*, vol. 45 , no. 3, pp. 678-690, May 1998.

[3] M. I. Haller and B. T. Khuri-Yakub, "A Surface Micromachined Electrostatic Ultrasonic Air Transducer," *IEEE Trans. Ultrason., Ferroelect., Freq. Contr.*, vol. 43, pp. 1-6, Jan. 1996.

[4] M. Rafiq and C. Wykes, "The performance of capacitive ultrasonic transducers using v-grooved backplates," *Meas.Sci.Technol.*, vol.2, no. 2, pp. 168-174, Feb. 1991.

[5] J. Hietanen, J. Stor-Pellinen, and M. Luukkala, "A model for an electrostatic transducer with a grooved backplate," *IEEE Meas. Sci. Technol*., vol. 3, pp. 1095-1097, 1992.

[6] P. Mattila, F. Tsuzuki, H. Vaataja, and K. Sasaki, "Electroacoustic Model for Electrostatic Ultrasonic Transducers with V-Grooved Backplates," *IEEE Trans. Ultrason., Ferroelect., Freq. Contr*, vol. 42, no. 1, pp. 1-7, Jan. 1995.

[7] M. J. Anderson, J. A. Hill, C. M. Fortunko, N. S. Dogan, and R. D. Moore, "Broadband electrostatic transducers: Modeling and experiments," J. Acoust. Soc. Am., vol. 97, pp. 262-272, Jan. 1995.

[8] I. Ladabaum, X. C. Jin, H. T. Soh, F. Pierre, A. Atalar, and B. T. Khuri-Yakub, "Microfabricated Ultrasonic Transducers: Towards Robust Models and Immersion Devices, "in *Ultrasonics Symposium*, San Antonio, TX, 1996, pp. 335-338.

[9] W. P. Mason, *Electromechanical Transducers and Wave Filters*. New York: Van Nostrand, 1942.

[10] K. Suzuki, K. Higuchi, and H. Tanigawa, "A Silicon Electrostatic Ultrasonic Transducer," *IEEE Trans. Ultrason., Ferroelect., Freq. Contr.*, vol. 36, pp. 620-627, Nov. 1989.

[11] A. Caronti, G. Caliano, A. Iula and M. Pappalardo, "An Accurate Model for Capacitive Micromachined Ultrasonic Transducers, " *IEEE Trans. Ultrason., Ferroelect., Freq. Contr.*, vol. 49, pp. 159-168, Feb. 2002.

[12] G. Caliano, A. Caronti, M. Baruzzi, A. Rubini, A. Iula, R. Carotenuto, M. Pappalardo, "PSpice modeling of capacitive microfabricated ultrasonic transducers,"in *Ultrasonics*, vol. 40, pp. 449-455, May 2002.

[13] J. Carter et al, *PolyMUMPs Design Handbook*. MEMSCAP Inc., Revision 11.0, 2005.

[14] J. A. Pelesko, D. H. Bernstein, *Modeling MEMS and NEMS*. Boca Raton: Chapman & Hall, 2003, ch. 5.

[15] M. D. Giovanni, *Flat and Corrugated Diaphragm Design Handbook*. New York: Marcel Dekker, Inc., 1982, pp. 133-135.

[16] W. Soedel, *Vibrations of Shells and Plates*. New York: Marcel Dekker, Inc., 1981, ch. 5, 8, 11.

[17] A. Lohfink and P. Eccardt, "Linear and Nonlinear Equivalent Circuit Modeling of CMUTs," *IEEE Trans. Ultrason., Ferroelect., Freq. Contr.*, vol. 52, pp. 2163-2172, Dec. 2005.

[18] E. Cretu, *Inertial MEMS Devices. Modelling Design and Applications*, Delft University of Technology, The Netherlands, 2003.

[19] P. Tang, P. Wang, M. Li, and M. Lu, "Design and characterization of the immersion-type capacitive ultrasonic sensors fabricated in a CMOS process," *Eurosensor XXIV Conference*, vol. 5, pp. 669-672, 2010.

[20] Wei You, Edmond Cretu, Robert Rohling, Ming Cai, "Tiltable Ultrasonic Transducers: concept, beamforming methods and simulation", *IEEE Sensors Journal*, 2011.

Appendices

Appendix A – VHDL-AMS file for the Behavioral Model of CMUTs

```
--3-component model with AC part (RMS)


LIBRARY ieee;
USE IEEE.MATH_REAL.all;
USE IEEE.FUNDAMENTAL_CONSTANTS.all;
USE IEEE.ELECTRICAL_SYSTEMS.all;


ENTITY cmut IS


   generic (
      Frequency : real :=3.0e6; -- AC frequency
      a   : real:=47.0e-6;    --membrane radius
      n   : real:=5041.0;    --number of cells
      dg  : real:=0.75e-6;    --gap distance (m)
      dm  : real:=1.5e-6;    --membrane thickness (m)
      dox : real:=0.0;    --insulating layer thickness (m)
      em  : real:=11.68;    --relative permittivity of membrane
      eox : real:=7.5;    --relative permittivity of insulating layer
      pm  : real:=2320.0;    --membrane density (kg/m^3)
      yo  : real:=160.0e9;    --membrane Young's modulus (N/m^2)
      sig : real:=0.22);   --membrane Poisson's ratio
```

```
    port (
        terminal e1, e2, e3, e4 : electrical;    --electrical port
        terminal m1, m2 : electrical);   --mechanical port

END ENTITY cmut;

ARCHITECTURE arch_cmut_mod OF cmut IS

    quantity uac across iac through e1 to e2;
    quantity udc across idc through e3 to e4;
    quantity vout across fout through m1 to m2;
    quantity C : real;

    constant do : real :=dg+dm/em+dox/eox;
    constant S  : real :=math_pi*a**2.0*n;
    constant mo : real :=0.613*dm*pm*S;
    constant k  : real :=16.0*math_pi*yo*dm**3.0*n/(3.0*a**2.0*(1.0-sig**2.0));
    constant p  : real :=0.329*a**2.0*phys_eps0*math_pi/(pm*dm*do**2.0*6.55297E-
10*(2.0*math_pi*2.7256E6)**2.0*(1.0-(Frequency/2.7256E6)**2.0));

BEGIN
    C==phys_eps0*S*(1.0/do+5.2029*(vout'integ-
0.4514*p*uac**2.0)/(3.0*do**2.0)+(5.2029*(vout'integ-
0.4514*p*uac**2.0))**2.0/(5.0*do**3.0))+2.0*S*phys_eps0*(0.5/do+0.1407*p*uac**2.0/do**
2.0+0.0874*(p*uac**2.0)**2.0/do**3.0+0.0658*(p*uac**2.0)**3.0/do**4.0);
    idc==phys_eps0*S*udc*vout*(5.2029/(3.0*do**2.0)+2.0*5.2029**2.0*(vout'integ-
0.4514*p*uac**2.0)/(5.0*do**3.0));

  iac==2.0*S*phys_eps0*uac'dot*(0.5/do+0.1407*p*uac**2.0/do**2.0+0.0874*(p*uac**2.0)**
  2.0/do**3.0+0.0658*(p*uac**2.0)**3.0/do**4.0+uac*(0.2814*p*uac/do**2.0+0.3497*p**2.0
  *uac**3.0/do**3.0+0.3950*p**3.0*uac**5.0/do**4.0));
```

```
  fout==mo*vout'dot+(k-phys_eps0*S*udc**2.0/do**3.0)*(vout'integ)-
(udc+uac)**2.0*phys_eps0*S/2.0*vout*(5.2029/(3.0*do**2.0)+2.0*5.2029**2.0*(vout'integ-
0.4514*p*uac**2.0)/(5.0*do**3.0));


END ARCHITECTURE arch_cmut_mod;
```

Appendix B – VHDL-AMS File for the AC Voltage Source

```
LIBRARY IEEE;
USE IEEE.ELECTRICAL_SYSTEMS.all;
USE IEEE.MATH_REAL.all;

ENTITY Vac IS
  GENERIC (Amplitude: voltage:= 15.0;
          Frequency: REAL:= 3.0e6;
          Phase: REAL:= 0.0;
          AcMagnitude   : voltage := 1.0; -- AC magnitude (V)
          AcPhase : real    := 0.0  -- AC phase (degree)
          );

  PORT (TERMINAL electrical_p,
                electrical_n: ELECTRICAL);
END ENTITY Vac;

ARCHITECTURE simple OF Vac IS
  QUANTITY v ACROSS i THROUGH electrical_p TO electrical_n;
  QUANTITY Vacv: voltage SPECTRUM 1.0, 0.0;

  -- for AC analysis
  quantity ac_spec    : real spectrum AcMagnitude, math_2_pi*AcPhase/360.0;

BEGIN

  if domain = frequency_domain use
```

```
    v == ac_spec;
  else
    v == Amplitude * sin(MATH_2_PI * Frequency * NOW + Phase) + Vacv;
  end use;

END ARCHITECTURE simple;
```

Appendix C – VHDL-AMS File for the DC Voltage Source

```
LIBRARY IEEE;
USE IEEE.ELECTRICAL_SYSTEMS.all;
USE IEEE.MATH_REAL.all;

ENTITY Vdc IS
  GENERIC (Amplitude: voltage:= 15.0
          );

  PORT (TERMINAL e3,
                e4: ELECTRICAL);
END ENTITY Vdc;

ARCHITECTURE simple OF Vdc IS
  QUANTITY v ACROSS i THROUGH e3 TO e4;

BEGIN

    v == Amplitude;

END ARCHITECTURE simple;
```

Appendix D – VHDL-AMS File for the Resistor

```
LIBRARY IEEE;
USE IEEE.ELECTRICAL_SYSTEMS.all;

ENTITY resistor IS
  GENERIC (value : RESISTANCE);

  PORT (TERMINAL electrical_p,
              electrical_n : ELECTRICAL);
END ENTITY resistor;

ARCHITECTURE simple OF resistor IS
  QUANTITY v ACROSS i THROUGH electrical_p TO electrical_n;

BEGIN

  v == i * value;

END ARCHITECTURE simple;
```

Appendix E – Script in the SMASH Simulator Control File

```
.VHDL SET KIND=ams

.VHDL COMPILE LIBRARY=work SOURCE=./const_package.vhd


.PARAM FREQUENCY_VALUE=6.0e6

.PARAM PHASE_VALUE=0


.PARAM ACMAGNITUDE_VALUE=10

.PARAM ACPHASE_VALUE=0


.PARAM R_VALUE=6.27e3

.PARAM AMPLITUDE_AC = 0.0

.PARAM AMPLITUDE_DC = 60.0


.Trace  AC     DB(TESTBENCH.TB_OUT'REFERENCE) Min=-4.4073961e+001
Max=6.2180182e+001

.Trace  Tran   TESTBENCH.TB_IN_AC'REFERENCE Min=-5.8996090e+002
Max=6.4895699e+003

.Trace  Tran   TESTBENCH.TB_IN_DC'REFERENCE Min=-5.8700984e+002
Max=6.4811082e+003

.Trace  Tran   TESTBENCH.TB_OUT'REFERENCE Min=-5.8900925e+002
Max=6.4791018e+003

.Trace  Tran   TESTBENCH.I_1.VOUT__INTEG Min=-6.8691424e-011 Max=1.5260729e-009




.Tolerance DEFAULT_DOT 1
```

.Tolerance DEFAULT_FLUX 1u

.Tolerance DEFAULT_CURRENT 100n

.Tolerance DEFAULT_VOLTAGE 1u

.Tolerance DEFAULT_TOLERANCE 1u

.H 1fs 1fs 1ns 125m 2

.Tran 1ns 1000ns 0s noise=no noisestep=1ns traceBreak=yes compress=no compressCoeff=1 compressTolX=0 compressTolY=1u powerup=no timeup=0s

.Option Tuning=Swift Swift=1m

.Method TRAP current=no voltage=no factor=10 scale=no global=no

.Step AMPLITUDE_DC 10 80 LIN 10

.AC dec 100000 1MEG 10MEG op=no

.VHDL elaborate TESTBENCH(SCHEMATIC_TESTBENCH)

.include "testbench_models_vhdl.inc"

.LIB "testbench.vhd"

Appendix F – Drawing of the CMUT Geometry in COMSOL Multiphysics

The geometry of the FEM model can be obtained from the following process: by clicking the icon of COMSOL Multiphysics on the desktop, the ‘Model Navigator’ pops out. After selecting ‘3D’ from the available ‘Space dimensions’, we choose ‘Solid, Stress-Strain’ from ‘Structural Mechanics’ under ‘MEMS Module’ of the ‘Application Modes’. The ‘Solid, Stress-Strain’ module studies the displacement, stresses, and strains that result in a 3D body given applied loads and constraints. Eigenfrequecy, frequency response, parametric, quasi static, time-dependent, and linear buckling analyses can be performed on this module. After clicking this model, a 3D frame of axes shows up and we will continue incorporating more modules such as ‘Electrostatics’ from ‘Electrostatics’ under ‘MEMS Module’ and ‘Moving Mesh (ALE)’ from ‘Deformed Mesh’ under ‘COMSOL Multiphysics’ before we draw the geometry. The screenshot of the ‘Model Navigator’ is shown in Figure 46.

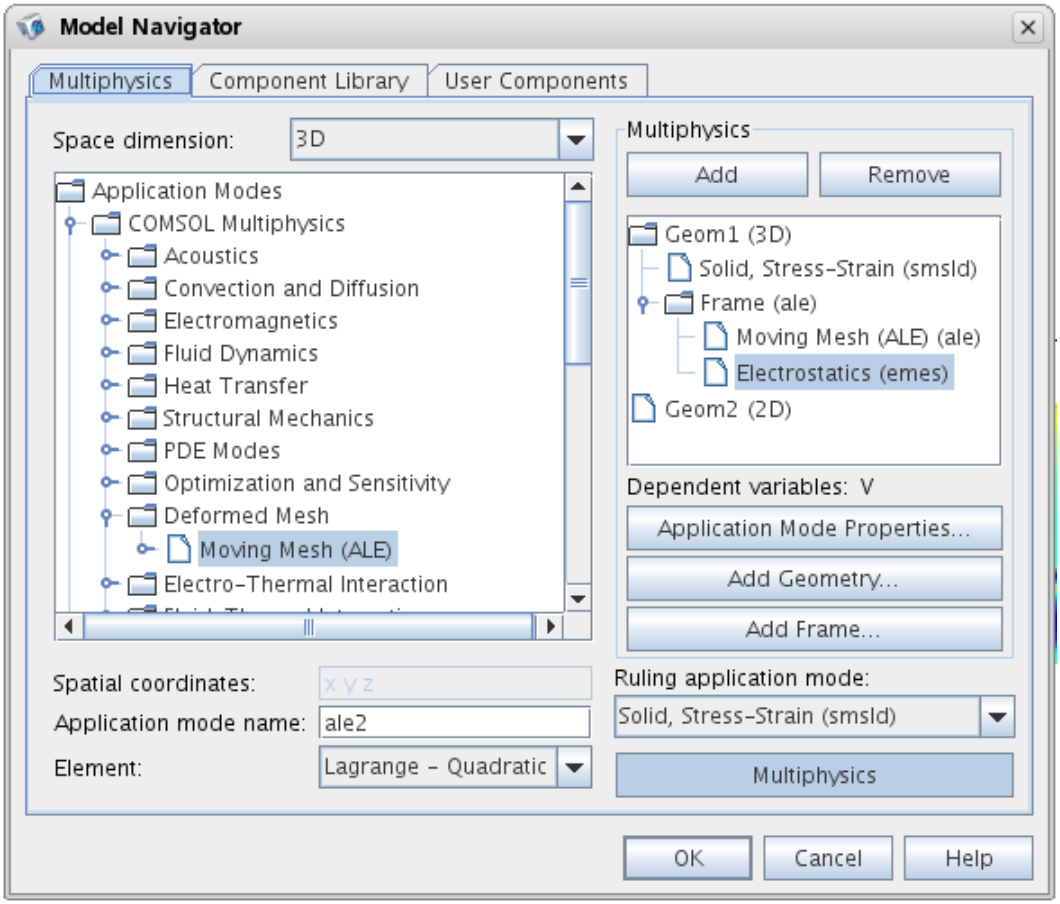

Figure 46. The screenshot of the 'Model Navigator' where all the three models 'Solid, Stress-Strain (smsld)', 'Moving Mesh (ALE) (ale)' and 'Electrostatics (emes)' are chosen.

First, we draw a cylinder with a radius of 32μm (as in the previous design) and a thickness of 1.5μm as the CMUT membrane. Then we draw a cylinder with the same radius but a thickness of 3μm to totally include the CMUT membrane as the surrounding air, and the distance between the lower surface of the CMUT membrane and the lower surface of the air is 0.75μm, which is equal to the thickness of the gap between the CMUT membrane and the bottom electrode. By clicking the 'Physics' Button, the 'Subdomain' and 'Boundary' Settings can be chosen for the three models respectively.

For the ‘Solid, Stress-Strain (smsld)’ model, the ‘Library material’ in the ‘Subdomain Settings’ is set to Poly-Si for the CMUT membrane, and the two air layers (below and above the CMUT membrane) are de-activated. In the ‘Boundary Settings’, under the ‘Constraint’ tab, the circumference of the CMUT membrane is set to ‘Fixed’ whereas the others are set to ‘Free’; the values for quantities F_x, F_y and F_z are set to Fes_nTX_emes, Fes_nTY_emes and Fes_nTZ_emes respectively. The screenshots of the ‘Subdomain Settings’ and ‘Boundary Settings’ for the ‘Solid, Stress-Strain (smsld)’ model are shown in Figure 47.

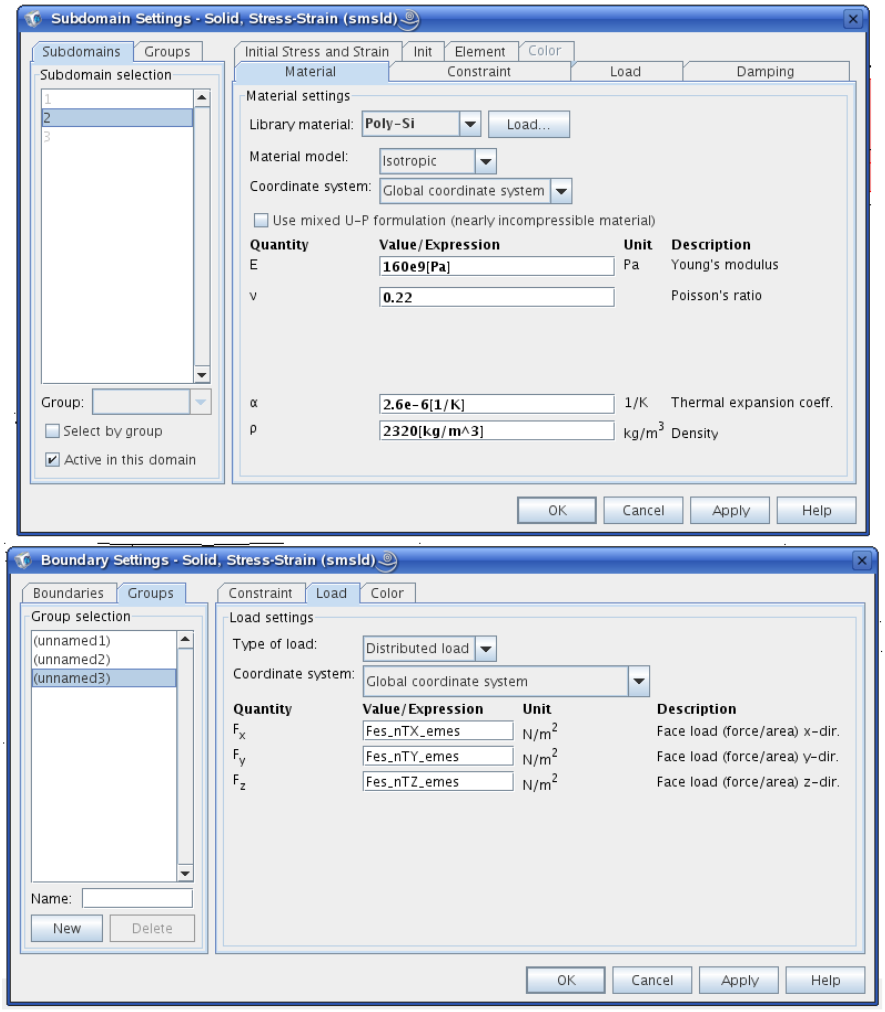

Figure 47. The screenshots of the ‘Subdomain Settings’ and ‘Boundary Settings’ for the ‘Solid, Stress-Strain (smsld)’ model.

For the ‘Moving Mesh (ALE) (ale)’ model, in the ‘Subdomain Settings’, the ‘Quantity’ of the two air layers is set to ‘Free displacement’, and the one of the CMUT membrane is set to ‘Physics induced displacement’ whose values are u, v and w. In the ‘Boundary Settings’, the circumference of the CMUT membrane is de-activated, the values for the two air layers are 0 for all quantities dX, dY and dZ, and values for the top and bottom surface of the CMUT membrane are set to u, v and w for dX, dY and dZ respectively. The screenshots of the ‘Subdomain Settings’ and ‘Boundary Settings’ for the ‘Moving Mesh (ALE) (ale)’ model is shown in Figure 48.

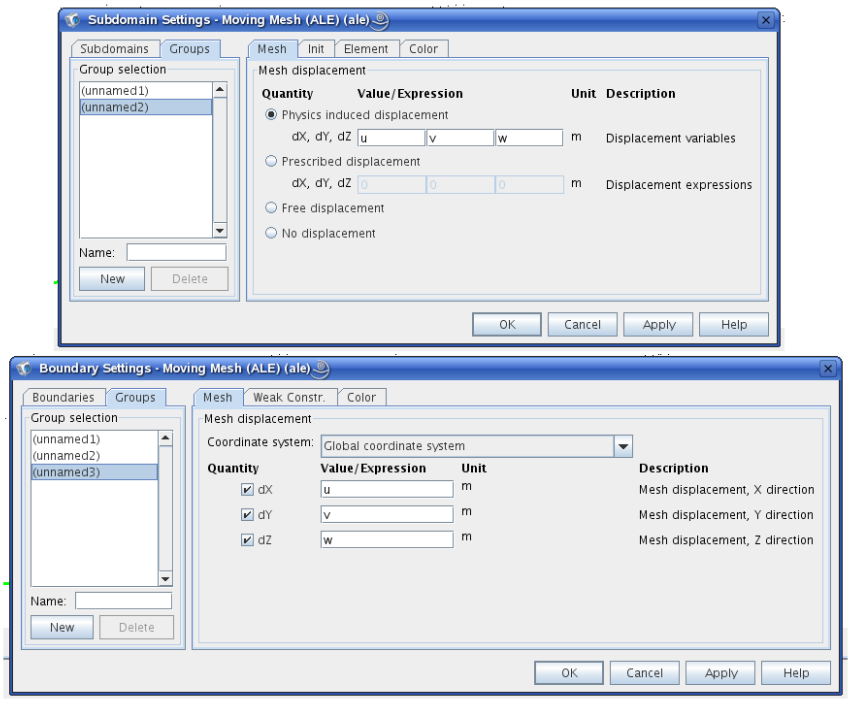

Figure 48. The screenshots of the ‘Subdomain Settings’ and ‘Boundary Settings’ for the ‘Moving Mesh (ALE) (ale)’ model.

For the ‘Electrostatics (emes)’ model, under the ‘Physics’ tab in the ‘Subdomain Settings’, Poly-Si is given to ‘Library material’ for the CMUT membrane, while it is air by default; under the

'Forces' tab, we include an electromagnetic force with the name Fes, a point (0,0,0) and an axis (0,0,1) to set the direction and coordinates of the electrostatic force that pulls the membrane down. In the 'Boundary Settings', under the 'Conditions' tab the top surface of the membrane is set to 'Continuity', 'Ground' is set to the bottom surface of the air layer below the membrane, the bottom surface of the membrane is set to 'Electric potential' while the values for the quantity V_0 is given by V_in or a fixed value depending on the analysis we will perform later, and the other surfaces are set to 'Zero charge/Symmetry'. The screenshots of the 'Subdomain Settings' and 'Boundary Settings' for the 'Electrostatics (emes)' model are shown in Figure 49.

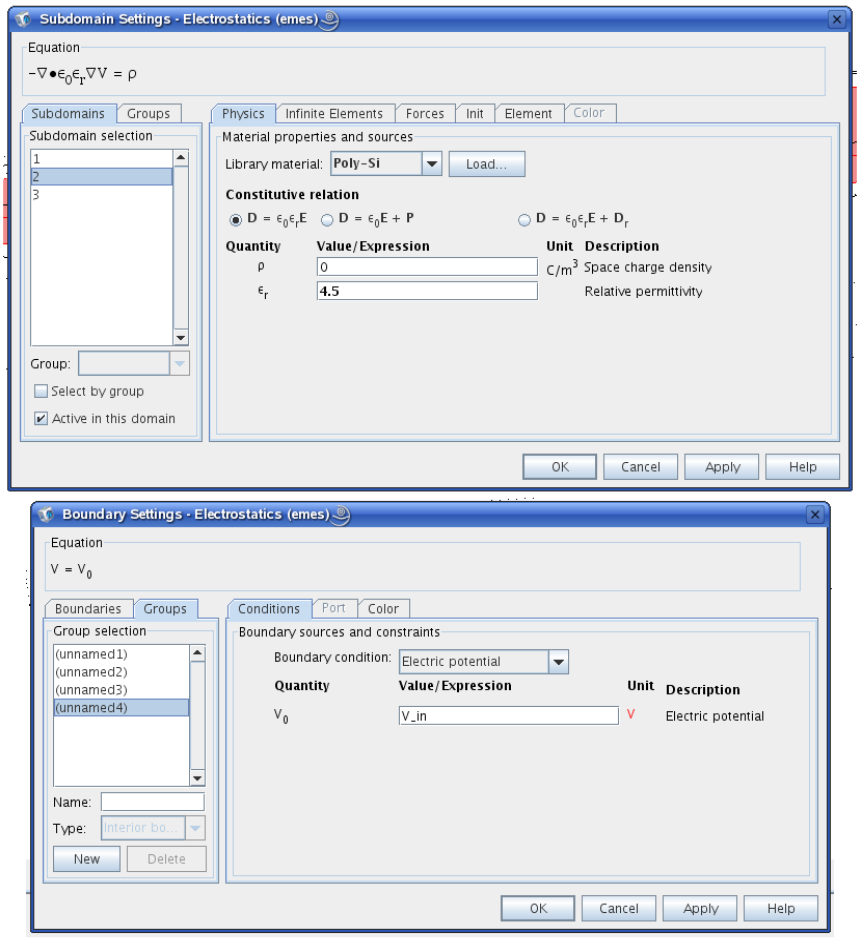

Figure 49. The screenshots of the 'Subdomain Settings' and 'Boundary Settings' for the 'Electrostatics (emes)' model.

Appendix G – Setup for Polytec Micro System Analyzer (MSA-500)

Double-clicking the PSV program icon on the desktop, the PSV software opened in the Acquisition Mode. After focusing the CCD camera image by using the coarse and fine focus control on the focusing block of the microscope and focusing the laser beam using the focus knob on the microscope adapter down to the smallest possible point on the test article, we were able to see a clear image with a well-defined laser spot, as shown in Figure 50.

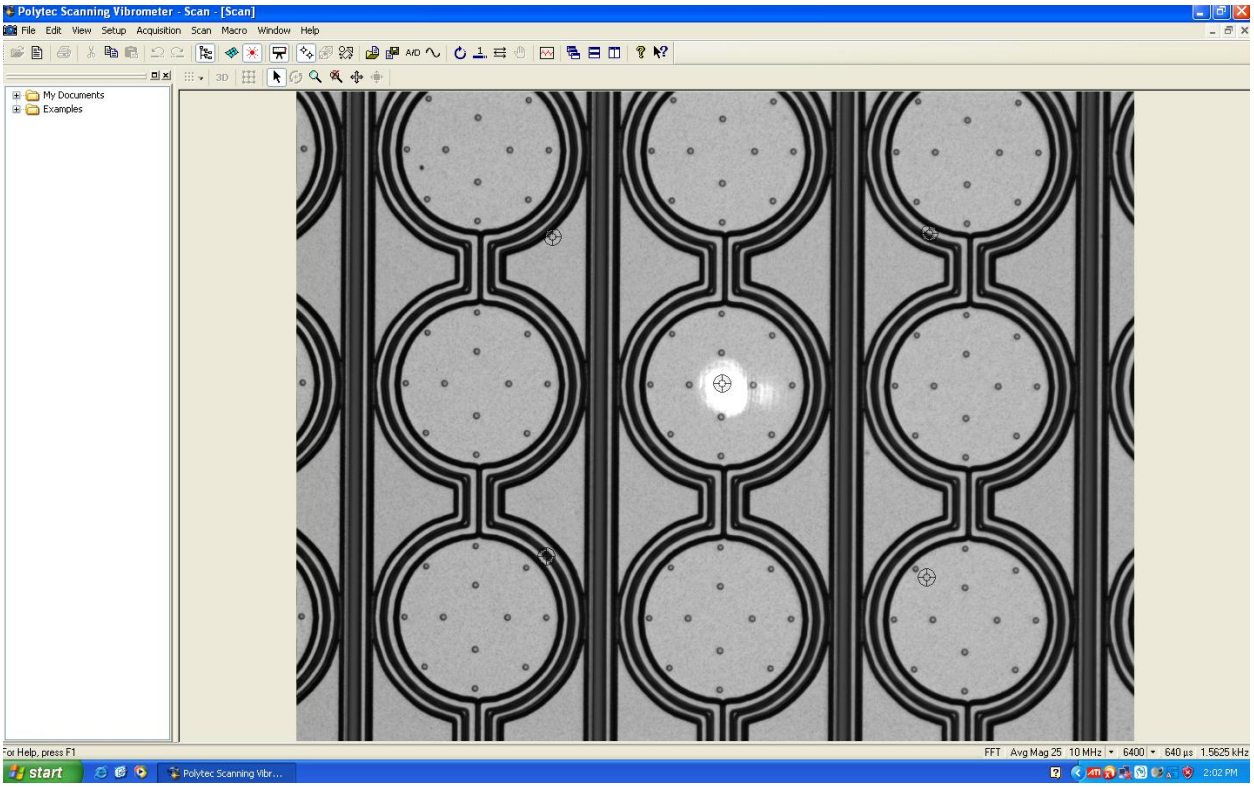

Figure 50. A clear image and a well-defined laser spot after CCD camera focusing and laser beam focusing.

Then, we needed to position the laser beam on the test object, which was to facilitate communication the PC and the scanner. This is also shown in Figure 50. In this figure, the

CMUT cell at the center of which lies the laser beam is the test cell, with one point at the center and another four at the extremes of the test cell.

A scan grid was created by choosing the Standard Mode. Of all the available shapes such as rectangle, ellipse, and polygon, we chose ellipse considering the shape of our test cell. The ellipse scan grid and its settings are shown in Figure 51.

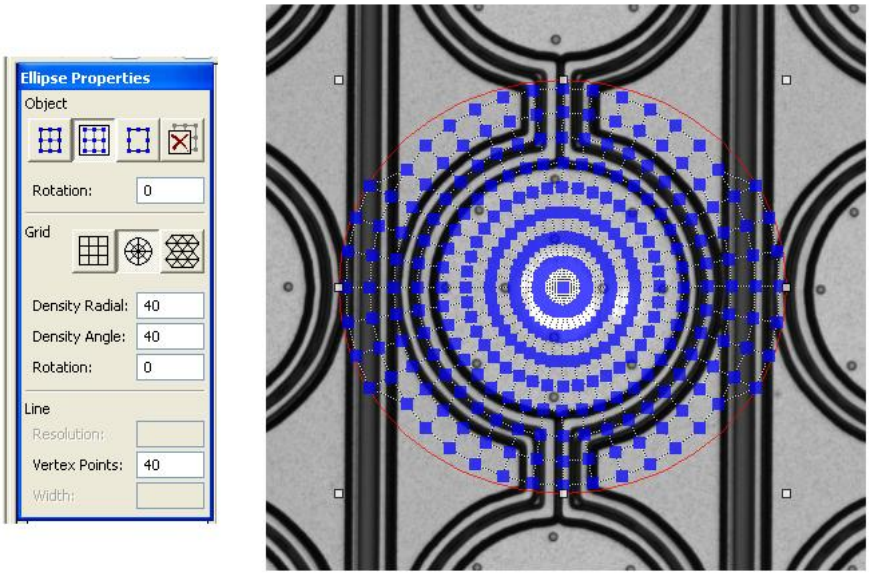

Figure 51. Ellipse scan grid (right) and its settings (left).

After the above settings, we came to setting up the measurement parameters by clicking ‘A/D Settings’ under the ‘Acquisition’ tab. Then the ‘Acquisition Settings’ window popped out, as shown in Figure 52.

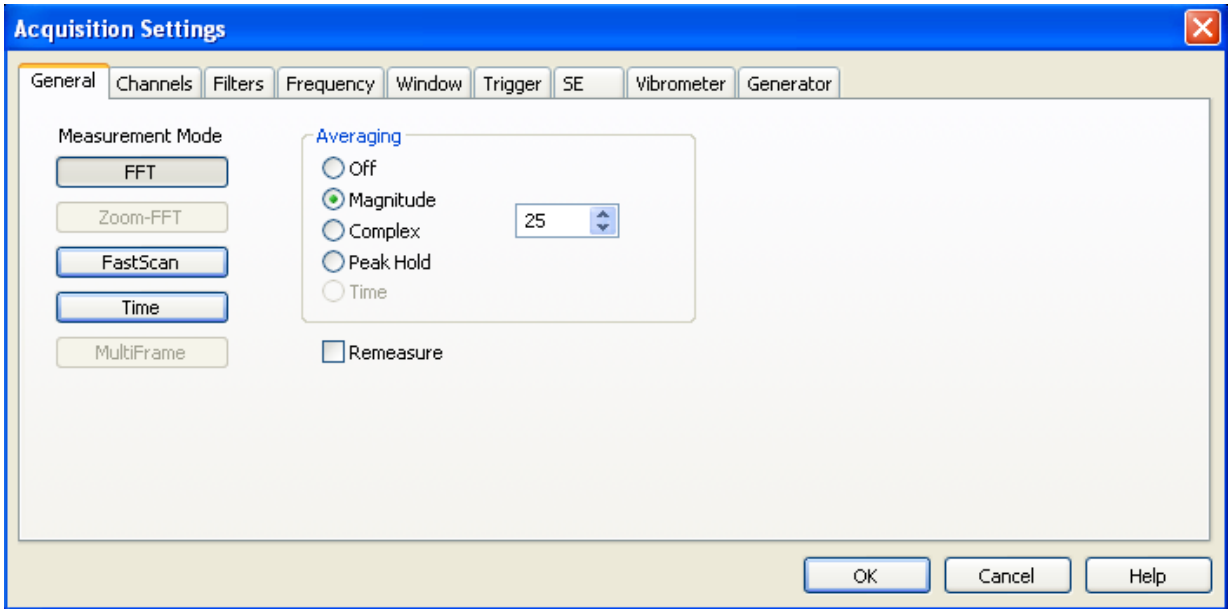

Figure 52. The screenshot of the Acquisition Settings window.

We selected the 'General' tab and clicked the box labeled FFT to make time and frequency domain measurements. We selected Magnitude Averaging and put the number 25 as the averaging times, since averaging helps reduce noise and improve overall measurement certainty. By selecting the 'Channels' tab, we could control the range on the acquisition board, AC/DC couple, and units. Both the Vibrometer and the Reference1 channels were activated, and the range was set to 10V and the impedance to 50Ohm for both channels. Since the CMUT cells vibrate in the megahertz frequency range and the maximum frequency range for the available velocity decoders is up to 1.5MHz, we would choose the displacement decoder instead, for which the maximum frequency range is 20MHz. Thus, in the 'Quantity' column we selected Displacement for both channels. The settings for the rest two columns 'Factor' and 'Unit' remain as default. The screenshot of the input channel settings is given in Figure 53.

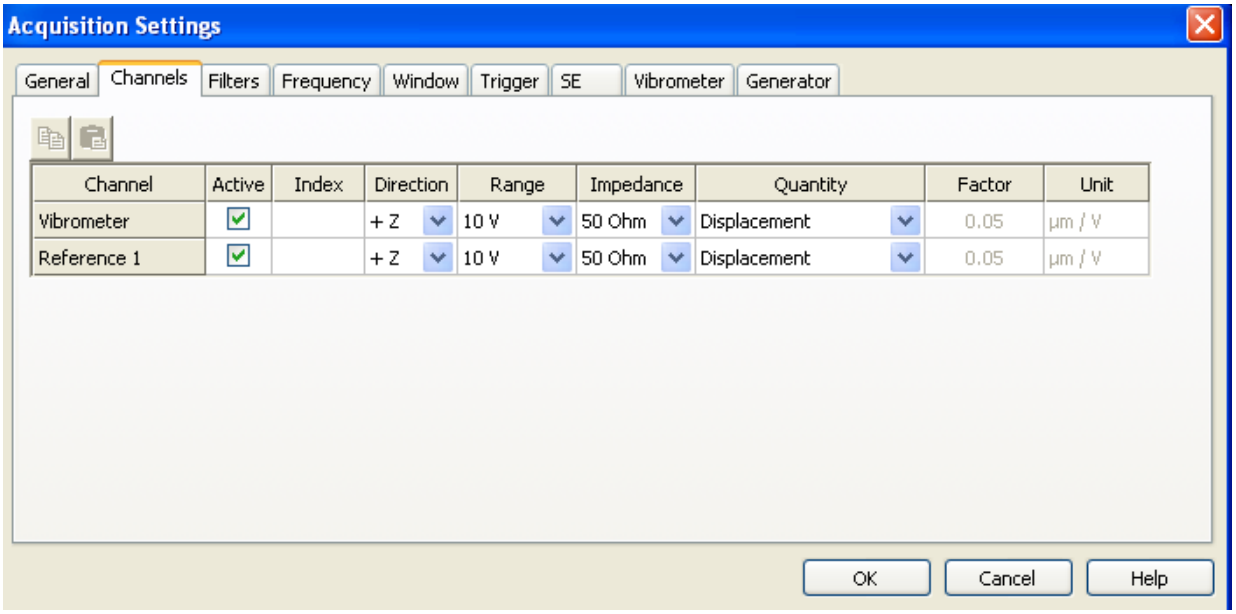

Figure 53. The screenshot of input channel settings.

According to the theoretical calculations and simulation results, the first few resonant frequencies of the CMUT lie between 1MHz and 10MHz. Therefore, we selected a frequency range of 10000 kHz. A low number of the FFT lines means faster measurement, but less resolution. Also, for lightly damped structures, more lines of resolution are needed. In our case, the measurement time was not a problem and the CMUT cells are lightly damped, so the number of FFT lines was chosen to be 6400. The screenshot of the 'Frequency' tab is shown in Figure 54.

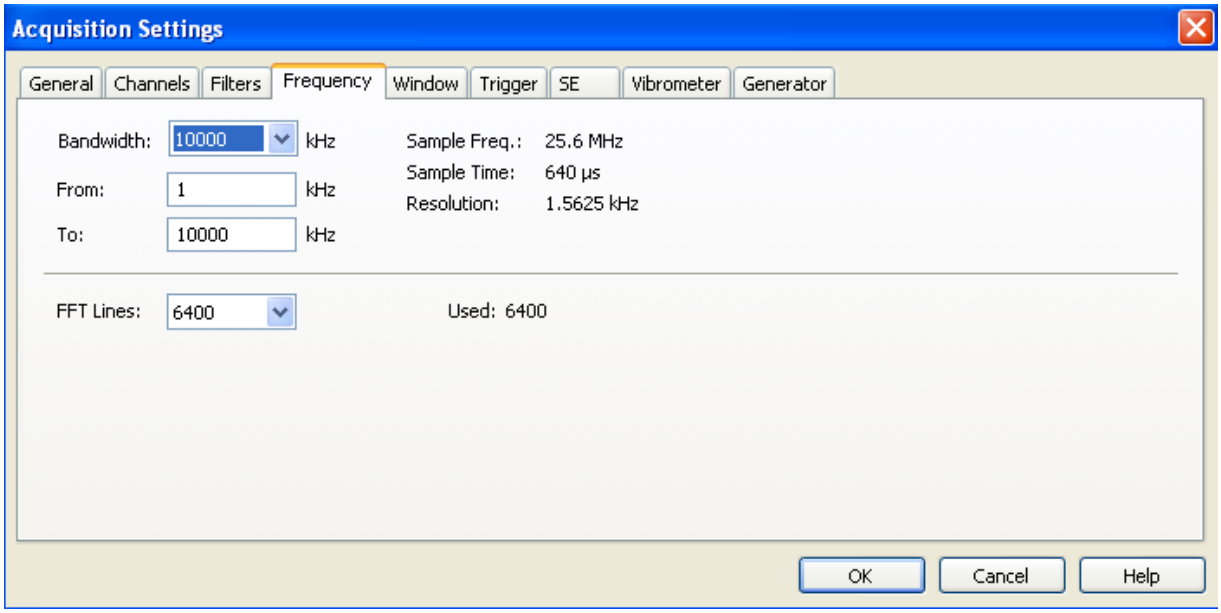

Figure 54. The screenshot of 'Frequency' tab.

We chose to not use any filters for the two channels, and to use rectangle window for both channels. The trigger source was turned 'Off', and Speckle Tracking was selected for both channels under the 'SE' tab in order to achieve similar signal quality for all scan points by avoiding the speckle nature of the backscattered light and differing surface qualities among difference scan points.

Since CMUTs usually operate in the megahertz frequency range, a decoder that is suitable to acquire high-frequency vibrations and fast transient motions was needed. The Displacement Decoder DD-300 is an auxiliary decoder that allows to measure vibrations and pulse-shaped motions in a frequency range of 30kHz to 24MHz with amplitude up to 75nm (peak to peak), which is particularly suitable in the domain of ultrasonic technology and micro mechanical systems. So in our case, we selected the auxiliary Displacement Decoder DD-300 and the

Velocity Decoder VD-02 to match the displacement decoder. The vibrometer settings screenshot is show in Figure 55.

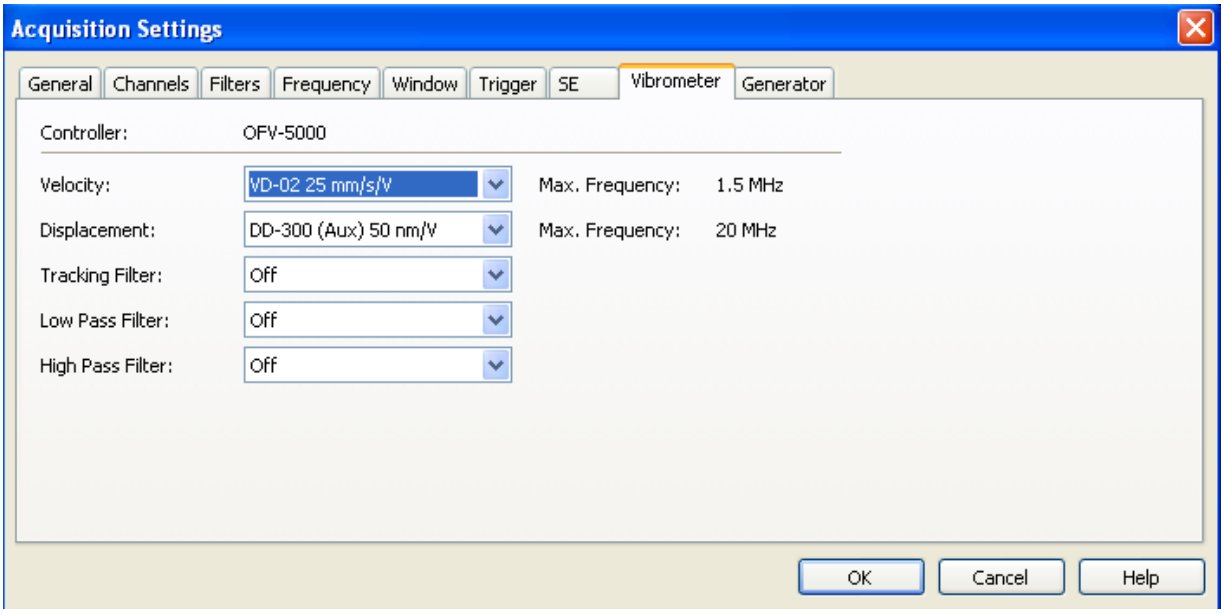

Figure 55. The screenshot of vibrometer settings.

Under the 'Generator' tab, we could choose the suitable waveforms for our measurements from Sine, Periodic Chirp, Pseudo Random, Burst Chirp, Burst Random, White Noise, Sweep, User Defined, Square, Triangle, Ramp. In order to measure the frequency response of the CMUT, 'Periodic Chirp' was chosen as our driving signal, which is a series of sinusoidal signals emitted to all FFT lines at the same time in the frequency range between 'From' and 'To' under the 'Frequency' tab. For the pull-in voltage testing, 'Sine' was chosen as input signal with a large offset (the DC bias component) and a very small amplitude. In the meantime, the sinusoidal signals can also be used to see the vibration shape of individual CMUT cells. The screenshot of the generator settings is shown in Figure 56.

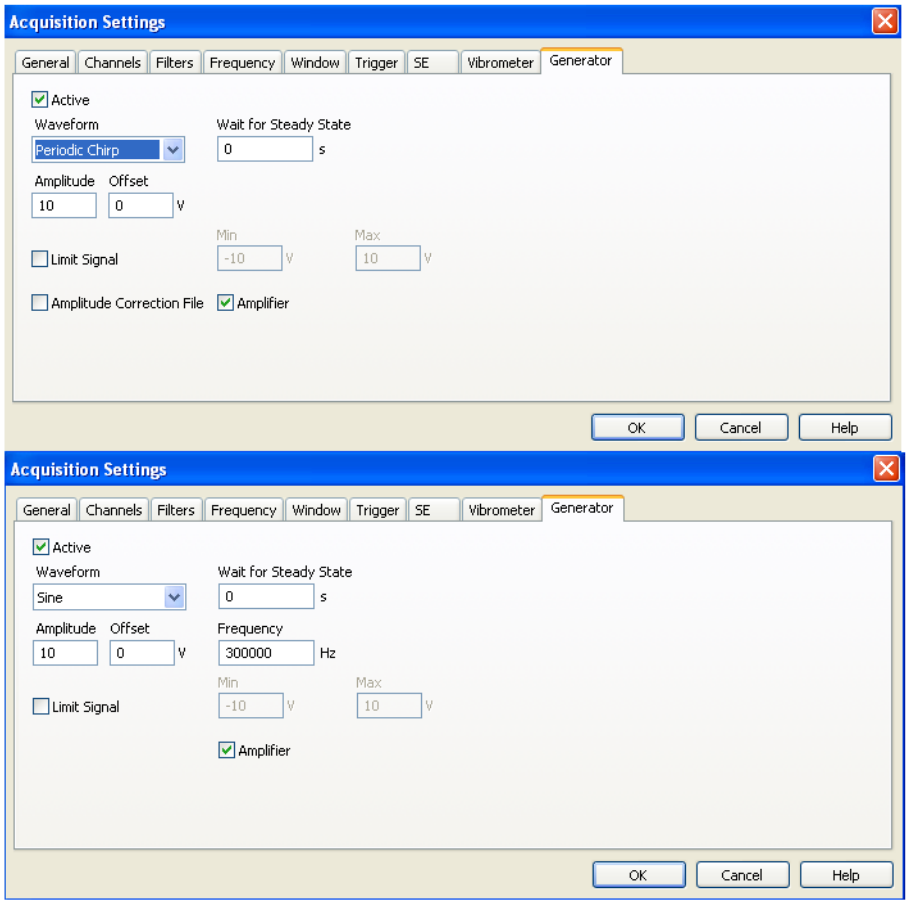

Figure 56. The screenshot of the generator settings.

By clicking ‘Scan’ under the ‘Acquisition’ tab, we could make a scanning measurement as shown in Figure 57.

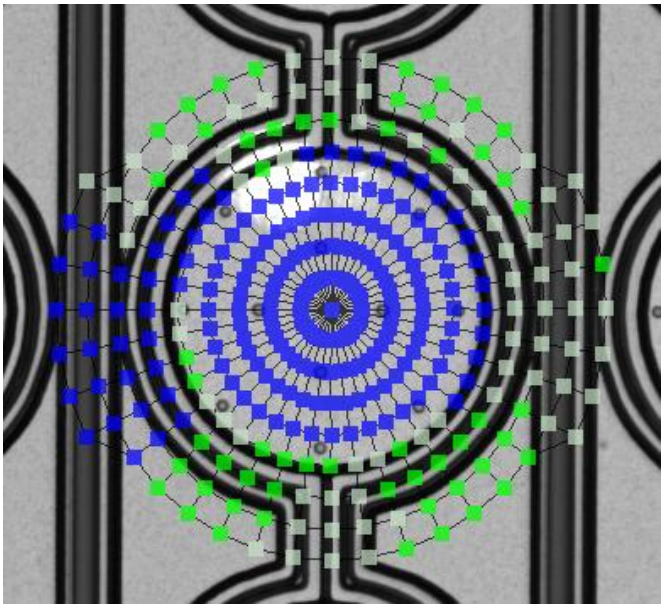

Figure 57. A CMUT cell during a scanning measurement.

The measurement results could be observed in ‘Presentation Mode’ after the scan was finished.

Appendix H – Wiring Diagram of a Packaged Die

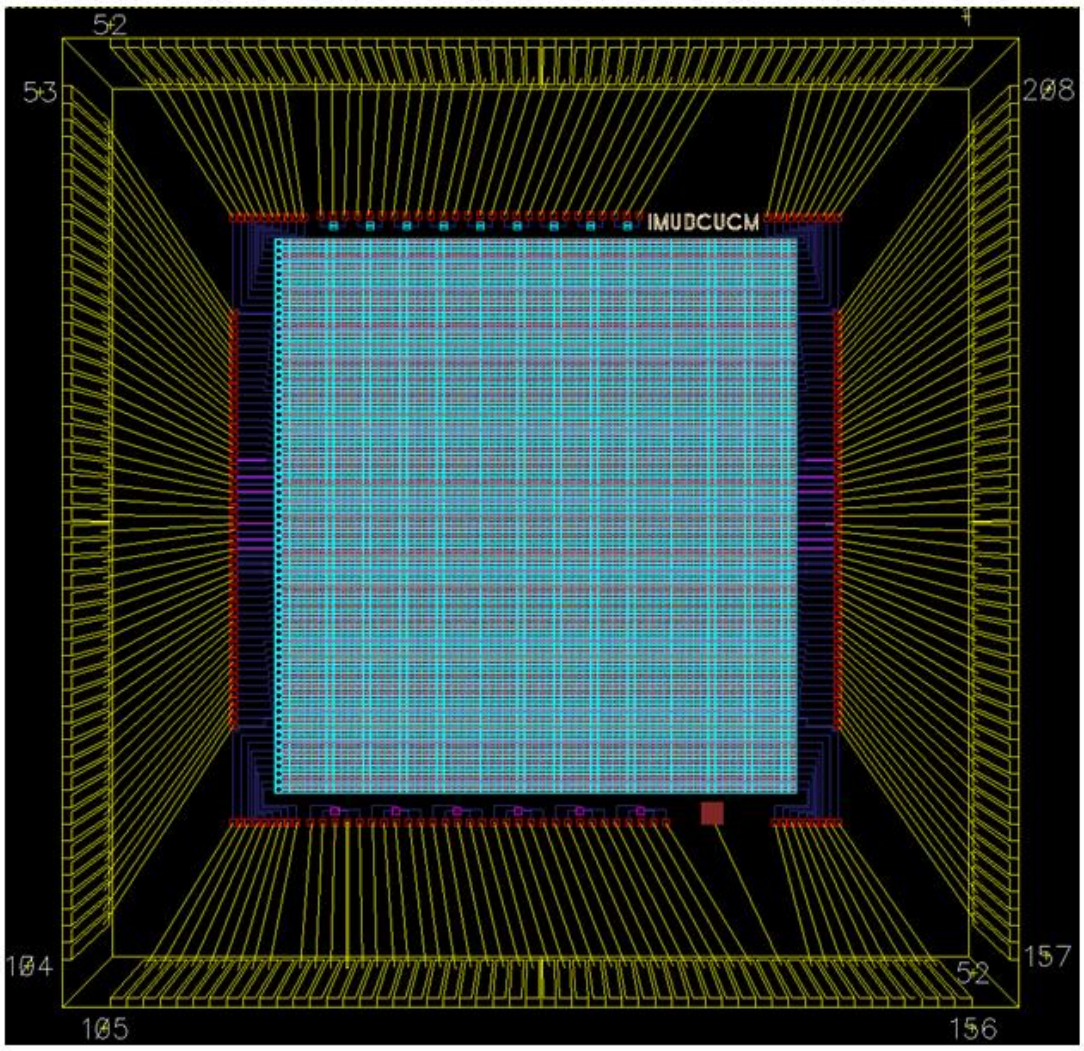

Figure 58. Wiring on a CMUT Die.